

Diss. ETH No. 17074

Dendrite engineering on xenon crystals

A dissertation submitted to the
SWISS FEDERAL INSTITUTE OF TECHNOLOGY
ZURICH

for the degree of
Doctor of Sciences ETH Zürich

presented by
MARCO FELL
Dipl. Phys. ETH
born 10.07.1976
citizen of Valendas (GR)

accepted on the recommendation of
Prof. Dr. K. Ensslin, examiner
Prof. Dr. J. Bilgram, co-examiner
Prof. Dr. B. Billia, co-examiner
Prof. Dr. H. Müller-Krumbhaar, co-examiner

2007

Meinen Eltern

Abstract

The experimental work presented here focuses on transient growth, on morphological transitions and on controlling. The free growth of xenon dendrites is perturbed by two different mechanisms, shaking and heating. Compared to the thermal fluctuations, the influence of shaking is considered to be large. Still the oscillation amplitude is not large enough to create a macroscopic convective flow in the growth vessel. Heating is performed up to the melting temperature. Melting of the growing crystal represents the largest applicable perturbation of growth.

Spontaneous and meta-stable multi-tip-configurations are stabilized, a denser sidebranch growth is induced and a periodic tip-splitting is found during perturbation by shaking. Heating on the other hand leads to controlled sidebranching and characteristic transitions of the shape of the tip. A deterministic behavior is found besides the random noise-driven growth. Together the two perturbation mechanisms allow a 'dendrite engineering', i.e. a reproducible controlling of the crystal shape during its growth.

The tip-splitting for dendritic free growth is found not to be a real 'splitting' of the tip, rather the respective growth velocities of the main tip and the fins change. The latter then surpass the main tip and grow into new tips. The occurrence of three- and four-tip-configurations is explained with this mechanism.

For a qualitative overview, the heat flow and the convective flow in the growth vessel is calculated using a finite-element solver for the Navier-Stokes and the diffusion equations. As a result the idea of a single axisymmetric toroidal convection roll across the whole growth vessel has to be dropped. The main effect of convection under earth gravity is the compression of the diffusive temperature field around the downward-growing tip.

The results imply the question whether there are more growth modes than only one marginally stable dendritic growth that compete with each other, and whether and under which conditions the system locks-in to one or another of these growth modes. The existence of a limit cycle is supported by the findings.

A model to explain the symmetry of dendritic crystals, e.g. snow crystals, is developed.

Zusammenfassung

Das freie Wachstum von Xenon-Dendriten aus der Schmelze wird durch zwei verschiedene Mechanismen gestört: Schütteln und Heizen. Verglichen mit den thermischen Fluktuationen kann das Schütteln als gross betrachtet werden. Die Schwingungsamplitude des Schüttelns reicht nicht aus, um eine makroskopische Strömung im Zuchtgefäss anzutreiben. Das Heizen bis über die Schmelztemperatur hinaus stellt in diesem Zusammenhang die grösstmögliche Störung des Kristallwachstums dar.

In Vergleich zum freien ungestörten Dendritenwachstum werden zufällig auftretende, metastabile Viel-Spitzen-Konfigurationen durch das Schütteln stabilisiert, ein dichteres Seitenastwachstum wird initiiert, und es treten Phasen mit periodischen Spitzenteilungen auf. Das Heizen führt zu gezielt ausgelöster Seitenastbildung und charakteristischen Veränderungen der Spitzenformen. Neben dem durch thermisches Rauschen beeinflussten Wachstum tritt auch ein deterministisches Wachstumsverhalten auf. Die Kombination dieser beiden Techniken erlaubt ein „Dendriten Engineering“, also eine gezielte Beeinflussung der Kristallform während des Wachstums.

Die Spitzenteilungen im freien dendritischen Wachstum sind nicht eigentliche „Aufspaltungen“ der Spitze. Es ist viel eher so, dass das Verhältnis der Wachstumsgeschwindigkeiten von Spitze und Rippen eines Dendriten sich ändern, wobei die Rippen schliesslich schneller wachsen als die Hauptspitze. Dies führt zum Entstehen von drei oder vier neuen Spitzen.

Eine Finite-Elemente-Berechnung der Navier-Stokes-Gleichungen gewährt einen qualitativen Überblick über den Wärmefluss und die Konvektionsströmung im Zuchtgefäss. Als Konsequenz aus dieser Simulation muss die Vorstellung aufgegeben werden, dass innerhalb des Gefässes eine grosse, achsensymmetrische Konvektionsrolle (angelehnt an die Form eines Torus) auftritt. Der wichtigste Einfluss der Konvektion unter natürlicher Gravitation ist die Kompression der Isothermen des rein diffusiven Temperaturfeldes um den nach unten wachsenden Kristall.

Die experimentellen Resultate führen zur Frage, ob neben dem knapp stabilen Wachstumsmodus für die Dendriten weitere konkurrierende Modi existieren, ob und allenfalls unter welchen Bedingungen das System zwischen diesen Modi wechseln kann, und welche es bevorzugt annimmt. Die Existenz eines Limitcycle wird durch die Ergebnisse gestützt.

Die Symmetrie dendritischer Kristalle wie beispielsweise Schneeflocken wird in einem Modell zu erklären versucht.

Contents

1	Introduction	1
1.1	Background and context	1
1.2	Motivation and aim of this work	2
2	Physical framework	5
2.1	Theoretical background	5
2.2	Growth morphologies in steady-state growth	7
2.3	Point attractor and limit cycle attractor	8
3	Experimental setup and procedures	11
3.1	Cryostat and growth vessel	11
3.2	Heating and shaking	13
3.2.1	Heater	13
3.2.2	Shaker	14
3.3	Optical system and tracking	15
3.4	Methods	16
3.4.1	Image processing	16
3.4.2	Smoothing and filtering the noise	17
3.4.3	Local curvature	18
4	Experimental results	21
4.1	Heating experiments	21
4.1.1	Controlled sidebranch initiation	21
4.1.2	Evolution of the tip parameters	24
4.2	Shaking experiments	28
4.2.1	Inclination and twist of the growth axis	28

4.2.2	Morphology stability	31
4.3	Cascading tip-splitting	32
4.4	Tip velocity	35
4.4.1	Tip velocity oscillations	35
4.5	An application: Dendrite Engineering	36
4.5.1	Symmetry	36
4.5.2	Transient tip shapes in melting	37
4.5.3	Sidebranch initiation and coarsening	43
4.5.4	Area	43
5	Simulations	47
5.1	Setup	47
5.2	Diffusive temperature field	48
5.3	Convective flow	49
5.3.1	Experimental observation	49
5.3.2	Simulation in 2D	49
5.3.3	Simulation in 3D	51
5.4	Heating and cooling	52
6	Discussion	57
6.1	Mechanism for tip splittings	58
6.2	Stabilized sidebranching	59
6.3	Unstable growth	60
6.4	Heat transfer as coupling mechanism	62
6.5	Fluctuations and instability	64
6.6	Convection	65
6.7	Conclusion	67
6.8	Outlook	68
A	Xenon	69
B	Piezo	71

List of Figures

2.1	Morphology diagram in two dimensions (E. Brenner, Jülich)	8
2.2	Doublons have been observed in 1980 already (U. Lappe, Jülich)	9
3.1	Experimental setup: Cryostat	12
3.2	Experimental setup: Growth vessel	13
3.3	Experimental setup: Growth vessel with heater	14
3.4	Three investigated temperature trends	14
3.5	Experimental setup: Capillary with shaking piezo	15
3.6	Contour separation algorithm	17
3.7	Contour smoothing using wavelet transformation	19
3.8	Data filtering using wavelet transformation	20
4.1	Specific initiation of dominant sidebranches	22
4.2	Tip velocity and radius change following a heating pulse	23
4.3	Tip shape during falling temperature transition	24
4.4	Difference between T-type and P-type sidebranches	25
4.5	Characteristic tip parameters during three different temperature trends	27
4.6	Two different types of inclinations	28
4.7	Temporal evolution of an inclination	29
4.8	Twist along the main growth axis	30
4.9	Multi-tip-configuration	31
4.10	Three types of tip-splittings cascades	33
4.11	Three types of tip-splittings cascades – temporal evolution	34
4.12	Detail of the characteristic T-type 45°-structure	34
4.13	Oscillation tip velocity	36
4.14	Shape and curvature of a symmetric crystal tip	38

4.15	Shape and curvature of a freely grown crystal tip	39
4.16	Over a large distance symmetric crystals	40
4.17	Three tip shapes: $ x ^{5/3}$ -tip with dominant sidebranches, spherical and spear-like	41
4.18	Characteristic tip parameters for the slowed temperature drop	42
4.19	A shaken and a freely grown dendrite in comparison	44
4.20	Comparison between the solidified volume of free and shaken dendrites	46
5.1	Mesh boundaries in three dimensions	48
5.2	The diffusion fields in two and three dimensions	50
5.3	Steady-state temperature and velocity in a two-dimensional growth vessel	51
5.4	Steady-state temperature and velocity in a three-dimensional growth vessel	52
5.5	Flow in the growth vessel after the 10 th heating pulse	54
5.6	The temperatures as calculated on four different points in the growth vessel.	55
6.1	The shape of a dendrite near the tip	58
6.2	The transition towards a doublon	59
6.3	Two- and three-dimensional tip-splittings	60
6.4	The transition towards a quadruplon and a triplon	61
6.5	Compression of the isotherms in shaking	62
6.6	Synchronous behavior of four spatially separated sidebranches	63
6.7	Synchronous behavior of four spatially separated sidebranches (temporal)	64
6.8	Selection diagram by Pelcé	65
6.9	Idea of convective flow across the whole vessel	66
6.10	The asymmetry of structures caused by convection	66
6.11	Convective flow in the growth vessel as found in CFD simulations	67
B.1	Home-built interferometer	72
B.2	Piezo elongation	73

List of Tables

3.1	Performance of contour separation algorithms	18
5.1	Mesh sizes in two and three dimensions	47
5.2	Temperature and convective flow near the tip in two and three dimensions . . .	52
5.3	Temperature in a pure diffusive temperature field in two and three dimensions .	53
B.1	Technical properties of the piezo actuator according to the data sheet.	71

Chapter 1

Introduction

1.1 Background and context

The growth of crystals into undercooled melt is a nonequilibrium process. It can lead to dendritic patterns as an archetype for pattern formation in natural processes far from equilibrium. Well known examples for these patterns are snow crystals. Although they all look similar, two ice crystals never have an identical shape [1]. Every snowflake is a postcard with information about the atmospheric conditions in the environment of its growth. Still it is possible to find characteristic properties such as length scales or sidebranch densities for a broad range of crystal shapes. Because tree-like patterns (hence the name *dendrites* from δένδρον) are found everywhere in nature (growth and aggregation processes in chemistry, biology, crystal growth), these structures have been studied for many years. The appearance of dendrites in cast metals attracts strong interest to this topic: The microscopic dendritic structure arising when a solid grows from its undercooled melt influences the bulk properties of metals like strength, elasticity, ductility etc. After three thousand years of experience in metallurgy, only little is known about the solidification process taking place on microscopic scales in large volumes. With a total production of more than 1100 million metric tons of steel in 2005¹, there is a huge potential for optimization in industrial applications of designing the properties of bulk metals.

Unfortunately, the solidification of steel can not be observed in real time. With synchrotron radiography it is possible to investigate only the near-surface layers (e.g. [2,3,4]). Furthermore steel is not a single component material which complicates the description and analysis of the solidification process. Often an optical transparent model substance is used to overcome these obstacles. There are different materials well-suited for the research on dendritic growth, such as pivalic acid (PVA), succinonitrile (SCN) and xenon the most prominent ones. As a model for two-component systems, the organic alloys SCN (with acetone) and PVA (with ethanol), ammonium bromide and ammonium chloride (NH_4Br , NH_4Cl) in water, and $CBr_4 - x\%C_2Cl_6$ are used with great success.

¹http://www.stahl-online.de/wirtschafts_und_Politik/stahl_in_zahlen/2005/stahlerzeugungWelt.jpg

1.2 Motivation and aim of this work

The research in dendritic growth in the last decades led to a considerable theoretical understanding of several aspects. Ivantsov found the rotational paraboloid to be a solution of the *Stefan problem* in a pure undercooled melt (see section 2) about 60 years ago. Langer and Müller-Krumbhaar [5] incorporated the anisotropy of the surface free energy in a theoretical description of the idealized crystal shape near the tip in two dimensions. For a review see reference [6]. A steady-state solution, defined by a unique shape of the tip was found. The influence of thermal fluctuations on the branching was investigated in various studies, for a comprehensive review by Langer, see reference [7]. The needle-crystal as an analytical solution for the three-dimensional growth with anisotropic surface free energy was introduced by Ben Amar and Brenner [8,9]. Good agreement with the theories was found in experiments on different aspects like growth rate (e.g. [10,11]), tip shape (e.g. [12,13]) or sidebranching (e.g. [10,14,15,16]).

In most theoretical models, the dendrite is assumed to grow unperturbed in an undercooled melt. Prominent experiments to prevent any perturbations were performed by Glicksman et al. [17,18] aboard the Space Shuttle. For the testing of steady-state theories, a microgravity environment is probably the best suited.

Since these ideal growth conditions can not be provided on earth and in the large volumes in steel production, the focus shifted on perturbations. Only a few experiments have been performed up to now under the aspect of transient growth conditions. Qian and Cummins [19] included sidebranching by a localized laser pulse, where heat was deposited in the melt ahead the tip of a dendrite. Sidebranching was induced that way and an exponential growth of the sidebranches was found. The same technique of heat depositing by laser is used in directional solidification experiments in quasi-two dimensions (e.g. [20,21]). It allows to control the spacing of the fingers and the splitting. Another type of perturbation experiments was performed on PVA dendrites by Bouissou et al. [22,23]. In a quasi-two dimensional growth cell an external flow has been applied and an increasing growth rate was found. An oscillating flow lead to regular sidebranches and a linearly increasing amplitude (i.e. length of this sidebranches). Börzsönyi et al. [24] calculated the influence of a pressure oscillation in 2D using a phase-field model. He performed a test experiment on changing pressure on the liquid crystal nematic-smectic phase transition that showed qualitatively good agreement with his calculations results of regularized sidebranches. Koss et al. [25] found that a pressure change on a three-dimensional SCN dendrite affects its radius and its growth velocity as a different temperature would do. The *Clausius-Clapeyron* effect was found to hold in solidification experiments. During the work on this thesis, the author was told about a similar but yet unpublished work by Dougherty [26] on transient growth on ammonium chloride dendrites.

The influence of convective flow on the growth was investigated experimentally [27] and numerically [28,29,30]. It has been shown in ref. [29] that with convective flow the sidebranching occurs at a higher spatial frequency than without convection. The stability constant σ^* (see equation 2.4) was determined to be up to 50% higher by Lee et al. [27].

An increasing number of numerical simulations in two and three dimensions have been performed in computational domains large enough to be comparable with experiments and theo-

ries. Phase-field models agree with observations of doublons (e.g. [31, 32, 33]) and theoretically predicted characteristic length scales (e.g. [34, 35]).

Experimentally, sidebranches in free growth show up spontaneously at a distance of about 10 tip radii behind the tip [11] and determine the shape of the crystal from that point on. Two possibilities have been discussed about the onset of the sidebranches. On the one hand there is the widely accepted idea of *thermal noise* fluctuations that gives rise to the initiation of sidebranches. On the other hand there is another idea proposing a *limit cycle model* for the growing dendrite as dynamical system with an oscillating tip velocity. In the last years most theoretical work was focused on the first idea and the experiments were performed in this light. The presumable reason is the good agreement of both experiments and simulations with Brener's theory. Still the idea of the oscillation of the tip properties was continued of being cited (e.g. [18, 36]).

The experimental work presented here focuses on transient growth, on morphological transitions and on controlling. It provides a hypothesis on the combination of the two ideas mentioned above. The experimental findings described in chapter 4 provide the basis for this hypothesis and give rise to a technique of controlling the shapes of dendritic crystals during solidification, described in section 4.5. For a rough qualitative understanding of the diffusive and convective processes in the experiments, simulations (chapter 5) have been performed.

Most perturbation experiments have been done in a (quasi-)two-dimensional environment up to now. The main advantage of the experimental setup used in this work is the large volume of the growth vessel, providing the conditions for free growth in three dimensions, which means that the growth is not perturbed by the walls of the vessel. Based on this well-established fundament, a series of new experiments were performed where two different perturbation techniques have been applied to the growth of xenon crystals.

(i) The first concept is to directly change the only free control parameter, the temperature of the melt. Compared to the instantaneous parameter changes, possible in calculations or by applying pressure to the melt, the temperature change is done in a more intuitive way by heating.

(ii) The second perturbation is to shake the crystal in its melt. The results of more than 30 melting experiments and 20 shaking experiments can serve as a benchmark for future computational and theoretical results in order to describe the transient crystal growth in large vessels.

It is worth to mention that Gorbunov [37] reports about dendritic melting in superheated crystal volumes. In this case the meta-stable phase is solid. Therefore convection can be excluded. The observed structures of the liquid regions in the crystal are hardly distinguishable from the crystals in the melt described in this work. Various effects such as tip splitting and the occurrence of periodic sidebranches under periodically modulated superheating are found in the dendritic melting.

Chapter 2

Physical framework

2.1 Theoretical background

Melting is a first order phase transition. Latent heat is released during freezing at the solid-liquid interface. The melting temperature (of a plane surface) is T_m , while the temperature in the melt, far away from the solid-liquid interface is T_∞ . The undercooling is $\Delta T = T_m - T_\infty > 0$. For comparison between different materials, the temperature field T is scaled with material constants, resulting in the dimensionless temperature field

$$u := \frac{(T - T_\infty)}{(\Delta T)}, \quad (\Delta T) = \frac{L}{c_p},$$

where (ΔT) is the unit undercooling, defined by L the latent and c_p the specific heat. The latent heat is transported away from the interface. This can happen either in a purely diffusive form or by convection involving mass transport. The former transport is described in the diffusion equation:

$$\frac{\partial u}{\partial t} = D\Delta u, \quad (2.1)$$

where D denotes the thermal diffusivity. This relation holds for both the liquid and the solid phase, with the respective diffusivity and specific heat parameters.

While one boundary condition is easily found – the temperature of the melt far from the solidification front is T_∞ or $u_\infty = 0$ in dimensionless units – the interface temperature requires a more detailed analysis [7]:

$$u|_{interface} = \Delta - \beta v_n - d\kappa, \quad (2.2)$$

where $\Delta = (T_m - T_\infty)\frac{c_p}{L}$ is the dimensionless undercooling far away from the interface. The second and third terms on the right hand side describe the *kinetic factor* and the *Gibbs-Thomson effect*. Both prefactors β and d are potentially anisotropic. The fourfold anisotropy (in 2D) resulting from the crystallographic f.c.c. structure of many metals is $d = d_0(1 - \varepsilon_4 \cdot \cos(4 \cdot \theta))$, with $d_0 = \gamma T_m c_p / L^2$ the capillary length, proportional to the isotropic part of the surface energy γ . In a three-dimensional description, the angular dependence term for d has a more complicated

form (e.g. in [38]). The local curvature of the interface is κ . The more convex the solid surface is, the lower is the local interface temperature.

At the interface the energy conservation is given:

$$v_n = D(\nabla u|_{solid} - \nabla u|_{liquid}) \cdot \hat{n}, \quad (2.3)$$

where v_n is the velocity normal to the solid-liquid interface that is proportional to the gradient in this direction. With this equation, dynamics enters the problem and it becomes a *moving boundary problem*. The main difficulty is the position of the interface. It is – at the same time – a solution as well as a boundary condition and therefore a part of the *Stefan problem* [39].

Three implicit assumptions are made in the formulation of equations 2.1-2.3:

- **One component:** The equations describe the problem in a pure single component system. This work is restricted to this case.
- **Free growth:** The initial temperature is T_∞ and it is kept at this value far from the growing crystal, no confinement effects influence the solid-liquid interface.
- **Symmetry:** The thermal constants D, c_p are the same in both phases.

The last assumption has been made in many theoretical works (known as *symmetric models*) and is justified by the argument, that the two parameters are at least in the same order of magnitude. Langer argues [7] that not too much information is lost by assuming this symmetry, while the mathematics is greatly simplified. The thermal flux in the solid is not investigated in most works. Still, incorporating the different diffusivities gives more complicated isotherms than usually assumed for convenience (in this work too), and therefore may lead to another system behavior (section 2.3).

Neglecting the kinetic and Gibbs-Thomson-terms, Ivantsov showed [40] that a rotational paraboloid, growing into undercooled melt, is a shape preserving solution of the Stefan problem. His solution is still considered to describe the basic shape of a dendritic crystal close to the tip. But it can not predict the unique growth rate v and radius of curvature ρ at the tip for a given undercooling that is observed in the experiments. Rather Ivantsov calculates the Péclet number $p = \frac{\rho v}{2D}$, depending on the undercooling Δ ¹, and the system could grow with every parameter pair (ρ, v) fulfilling this relation. Finally, the paraboloid does not describe the shape in 3D very well, neither does it explain the occurrence of sidebranches. The first problem (*selection problem* for a unique growth rate) was attacked with the *maximum velocity hypothesis* by Nash and Glicksman [41], which was replaced by the *marginal stability theory* [5] that predicts a unique volume growth rate

$$\sigma^* = \frac{2Dd_0}{\rho^2 v}, \quad (2.4)$$

depending on material properties only. It was assumed that the growth takes place at an operating point at which the tip is just marginally stable. The numerical value for the so called *stability constant* has been predicted in this theory $\sigma^* \cong 1/4\pi^2$.

¹ $\Delta = pe^p \int_p^\infty \frac{e^{-s}}{s} ds$

In a next step the *solvability theory* [42, 43, 44] incorporated the anisotropy of the surface tension. It was shown that this anisotropy has a major influence on the selection of a unique tip shape of the dendrite. Thermal noise was found to be amplified for selected frequencies [45]. From an initial wave packet, the amplified wavelengths grow with increasing distance from the tip. However the strength of thermal noise was found to be about one order of magnitude too small for the measured sidebranch amplitudes.

In a fully three dimensional theory for pattern selection for cubic anisotropic materials, Ben Amar and Brener [8, 9] described the shape near the axisymmetric tip without noise using a perturbation ansatz

$$z(r, \phi) = -\frac{r^2}{2} + \sum A_m r^m \cos(m\phi).$$

Furthermore Brener found the shape of the dendrite tip to be of the form

$$z \propto |x|^\beta,$$

with $\beta = 5/3$. This theoretical finding was confirmed by Bisang [46] to $\beta = 1.67 \pm 0.05$, with a prefactor $a = 0.58 \pm 0.04$. It is worth to mention that Breners 'arms' are not the 'sidebranches' in todays terminology. Rather his expression means the 'fins', a four-fold symmetric, integral structure of a dendrite. For a sketch of the cross-section, see figure 4.8(b).

Brener and Temkin [47] extended the theory away from steady-state under consideration of noise-induced sidebranching and found an exponential growth of the amplitude of the non axisymmetric sidebranches

$$A_{BT}(z) \approx \bar{S} \exp\left(\frac{2 \cdot (5/3)^{9/10}}{3\sqrt{\sigma^*}} z^{2/5}\right),$$

where the $\bar{S} = 2k_B T^2 c_p D / L^2 v \rho^4$ denotes the dimensionless fluctuation strength [45]. This amplitude has been verified by Wittwer [48].

2.2 Growth morphologies in steady-state growth

The morphologies of crystals grown freely from pure melt differ depending on undercooling Δ and surface energy anisotropy ε . A low anisotropy causes crystals to grow less oriented than dendrites. Brener et al. [49, 50, 51] developed *analytically* a phase diagram (see fig. 2.1) to classify the different two-dimensional growth morphologies. It has been proposed that there exists a unique growth morphology for a given parameter set (Δ, ε) . The exact position of the boundaries between the region depends on numerical parameters, e.g. the fluctuation strength.

A morphology diagram for two and three dimensional free growth was found by means of *phase-field calculations* by Singer et al. [52]. Experimentally, transitions have been identified between the different morphologies. Dendrite tips (FD-region) were observed to split and the crystal was found to continue to grow *temporarily* in seaweed morphology (FS, CS). It is suspected that these transitions are induced by noise.

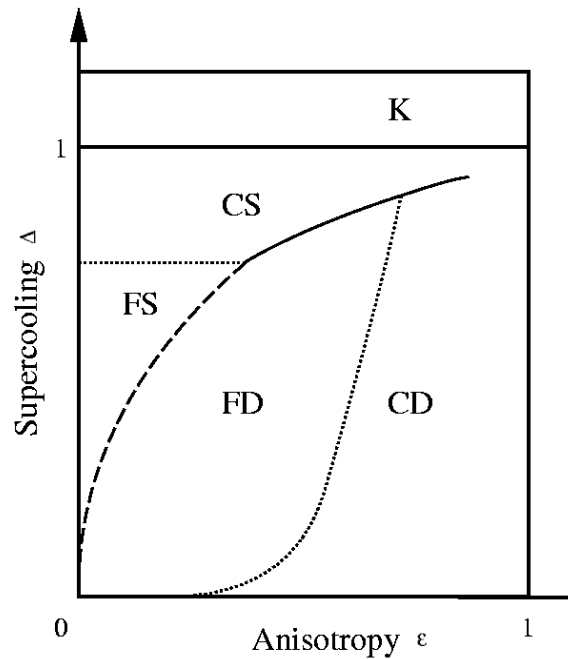


Figure 2.1: Phase diagram of morphologies: The growth morphology depends on both the anisotropy of the surface tension ε and the undercooling Δ . In the (ε, Δ) domain there are 5 different regions, denoted with FD, CD, FS, CS and K, where C indicates compact, F fractal, D dendritic, S seaweed-like growth. In the region with undercoolings higher than unity, the kinetics K dominates the growth.

Dendrites are only one of the solutions for the Stefan problem discussed in section 2.1. Ihle and Müller-Krumbhaar [53, 54] numerically found stable double fingers as another solution in two dimensions. They assumed these *doublons* to be the building blocks of seaweed. In fact, these structures have been observed almost 15 years before in an experimental work by Lappe [55] (see fig. 2.2) and maybe in other works too, but they have not been investigated systematically until Akamatsu’s experiments in quasi-two dimensions [32]. Stalder and Bilgram [33] observed the *dendritic doublons* in a three dimensional growth vessel. The occurrence of Stalder’s three-dimensional doublons was correlated with perturbations and did not lead to seaweed growth apart from a few seldom cases. They were therefore identified as new growth morphology – besides the dendrites – existing for free growth. In recent works multi-tip configurations have been observed (e.g. [48]).

2.3 Point attractor and limit cycle attractor

In early theories for the selection problem, the existence of a *limit cycle* for the tip growth parameters was suggested by Holzmann [56]. As a condition to find a limit cycle two different diffusion constants for the solid and the liquid phase are found to be necessary.

Langer and Müller-Krumbhaar [5] proposed a stability criterion resulting in an *operating*

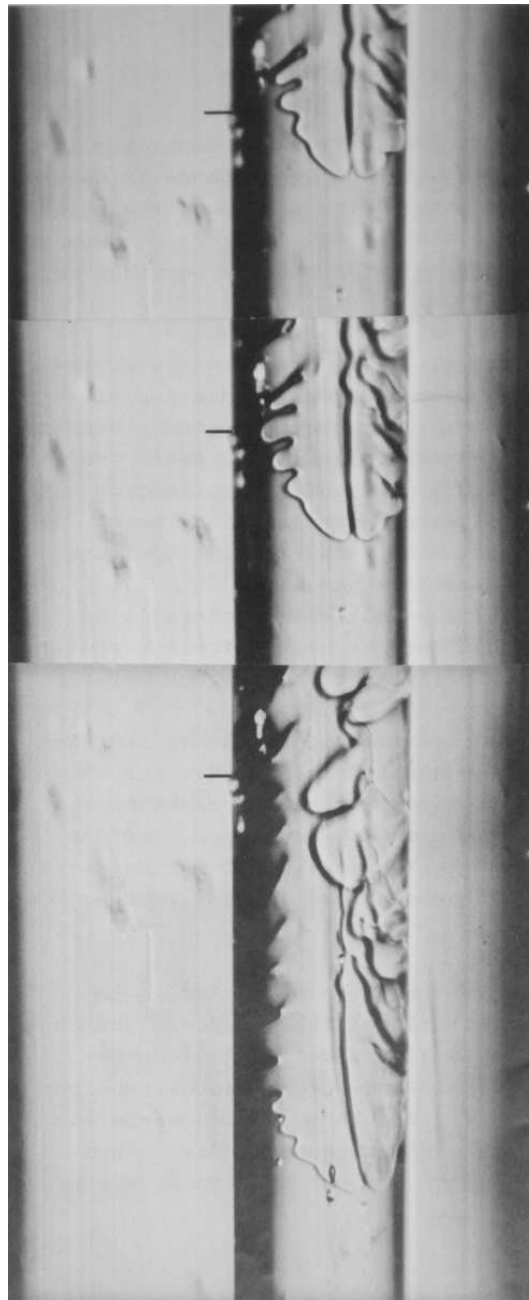


Figure 2.2: The double fingers (doublons) are found in this SCN crystal growing along the glass capillary. (U. Lappe, *Experimentelle Untersuchung des dendritischen Wachstums von Kristallen in unterkühlten Schmelzen*, Jülich, 1980)

point of the tip. In the phase space of ρ and v , the system behavior is analyzed at this point of marginal stability. However it is not clear how the system behaves in a small region around this point attractor for dendritic needle-crystal growth. It could show a noise-driven erratic behavior around the one special point, or it could be driven into a limit cycle, thus lock-in to

some oscillatory state. This was the main idea of another analysis [57] where the same authors argued that noise always drives the system in such a limit cycle as a unique operating mode for a growing dendrite.

Many experiments show a constant tip velocity. Glicksman [17] and Bisang [11] for example found the velocity to be constant within $\leq 5\%$ margin over the observation time. Measurements of the stability constant σ^* result in unique values, and are comparable to each other for different materials. The absolute values are in the region of the theoretically predicted $\sigma^* \cong 0.025$ [58].

Thermal fluctuations in fact seem not to be strong enough to surpass the (marginal) stable character of the unique operating point. The experiment of Qian and Cummins [19] imply that the marginally stable operating point is unique. The crystal was heavily perturbed with a laser pulse, depositing heat near the dendrite tip. The deformations were below the limit of detection at the tip but evolved rapidly to a sidebranch-like structure. Still the crystal preserved its dendritic shape, i.e. no tip-splitting event was detected.

In both the solvability and in Brener's theory, thermal fluctuations are the reason for random sidebranching. This stochastic character for free dendritic growth had been confirmed in experimental observations: Dougherty [14] reported that sidebranches show no periodicity and no apparent onset. Bisang's results [11] confirmed the random branching, but stated more precisely the distance where the sidebranches become visible to about 14 tip radii behind the tip.

On the other hand, there are experiments that propagate an oscillating tip. Raz [59] reported on this topic, as well as LaCombe [18] and Liu [36] in more recent works. They observed tip velocity oscillations and periodical sidebranching. Honjo [10] observed both, tip-stable and tip-oscillating types of dendrites, the latter showing highly correlated sidebranches.

In a recent work, Glicksman [60] analyzes the temperature boundary conditions and proposes the limit cycle as an alternative to the marginal stable interface under selective noise amplification.

In this framework, the results of our different experiments are an indication that both ideas, the operating point of marginal stability and the attractive limit cycle, should to be considered and maybe extended with an unstable operating point for multi-tip configurations for a complete understanding of the dendritic growth.

Chapter 3

Experimental setup and procedures

The rare gas *xenon* is used as an experimental substance. It is an excellent model substance for metals since it solidifies in f.c.c. structure and has a low melting entropy. Xenon grows with a rough surface and the formation of dendrites is observed. The substance is liquid at 162 K and transparent, allowing *in-situ*-observation of the growth. Unlike many organic substances, xenon forms a simple liquid and does not decompose at T_m . The purity is 99.9999%, potential impurities (O_2 , N_2 , H_2O) are removed in a gas purifier prior to each experimental run. Xenon is recycled in a closed system.

3.1 Cryostat and growth vessel

As a basis for our perturbation experiments one needs to provide a controlled growth environment. Liquid 2-methylbutane (commonly known also as isopentane) serves as a heat bath. Its temperature is controlled by a closed loop. The melting temperature of xenon $T_m = (161.3897 \text{ K})$ allows to use liquid nitrogen (boiling temperature 77.4 K) as cooling substance, the heat transfer between the two liquids is controlled via a helium-filled double-wall vessel in between. The complete setup is depicted in figure 3.1 This setup makes it possible to keep the temperature constant ($\Delta T \approx \pm 10^{-4} \text{ K}$) for hours.

The xenon is filled into a growth vessel (fig. 3.2) in the center of the heat bath. The vessel is a cylinder with diameter and length of about 5 cm, with a volume of about 100 cm^3 , which is large enough to provide the conditions of free growth [12]. The solidification of a single crystal in the middle of the growth vessel is initiated by the *capillary injection technique* [61] from the top. Since the spatial orientation of the crystal growing out of the capillary is random, so is the projection of the crystal in the field of view. The turnable capillary permits to find a good projection angle. The capillary is movable in vertical direction in a range of $\pm 2 \text{ cm}$. The temperature in the vessel is measured by two thermal resistors Pt-100 located about 1 cm above and below the middle plane and about 1 cm off the shell. Three more thermometers are located at different positions in the heat bath.

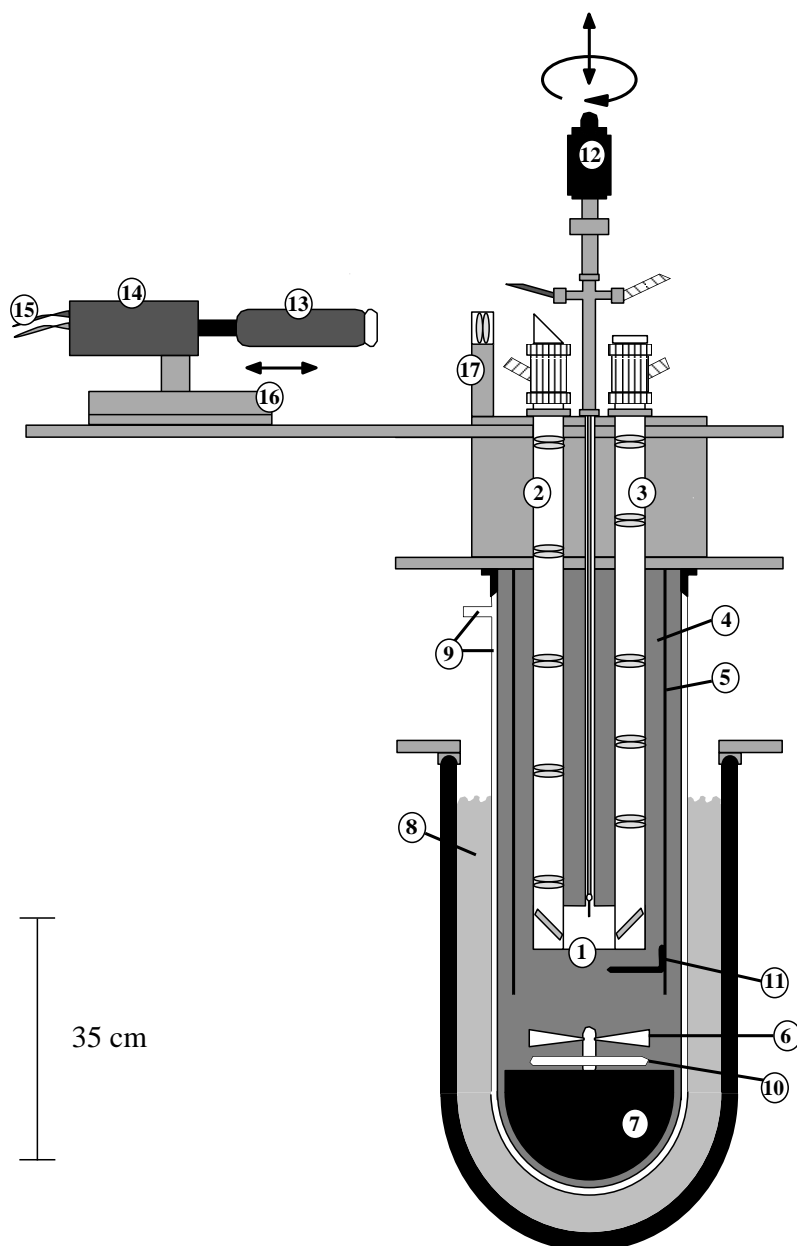


Figure 3.1: Experimental setup: The growth vessel (1) is surrounded by isopentane (4). A stirrer (6) – its oscillations damped by a large mass (7) – and a tube (5) provide a laminar flow in the isopentane, that is cooled by nitrogen (8). The thermal insulation and heat transfer is provided by a helium-filled dewar (9). A controller stabilizes the isopentane temperature in a closed loop with heater (10) and thermal resistors Pt-100 (11). By means of two periscopes illumination (3) and observation (2) of the growing crystal is done. They consist in a sequence of lenses with a flexible last field lens (17). The camera (14), on a movable stage (16) and equipped with an additional zoom lens (13), is connected to a computer (15).

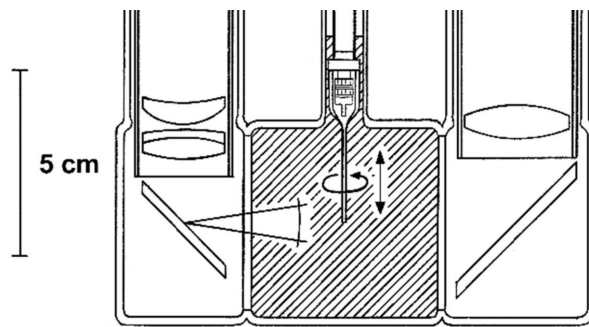


Figure 3.2: The growth vessel (middle) with the capillary and the observation and illumination periscopes to the left and the right.

3.2 Heating and shaking

Two types of experiments have been performed on two almost identical setups as described above. There are specific modifications made for the heating and shaking experiments.

3.2.1 Heater

For rapid temperature changes, a heating foil was wrapped around the lower half of the growth vessel (see fig. 3.3). A heating power of about 1 W was used to increase the temperature of the xenon melt in the growth vessel. Too much heating resulted in massive turbulence in the liquid, therefore it was heated only in intervals: Heating was activated for about 10 s (t_{on}) and thereafter interrupted for some 45 s (t_{int}). Overall the mean heating power was about 0.2 W while heating-up the melt and 0.1 W while keeping a temperature above the melting point. For the heating experiments an initial undercooling in the range of $100 \text{ mK} \lesssim \Delta T \lesssim 400 \text{ mK}$ was chosen. That corresponds to $2 \times 10^{-3} \lesssim \Delta \lesssim 8 \times 10^{-3}$ in dimensionless units. The application of heat pulses allowed to follow the heat flux. The lower one of the two resistance thermometers in the growth vessel indicated a temperature rise about 30 s after triggering the heating pulse; the crystal tip (about 2 cm off the bottom of the vessel) reacted visibly another about 30 s later. This time frame has been confirmed in the fluid-dynamics simulations, described in chapter 5.

Heating A few minutes after the crystal had left the capillary, a steady-state temperature field was established, and heating was started. Different temperature characteristics were tested. The main restriction was a temperature must not be kept above T_m for more than about 250 s. Otherwise the crystal would have broken off the capillary. Three temperature trends (shown schematically in figure 3.4) have been analyzed. The temperature rise from the initial temperature to the maximum in (I) is measured at the Pt-100 to happen within about 10 seconds.

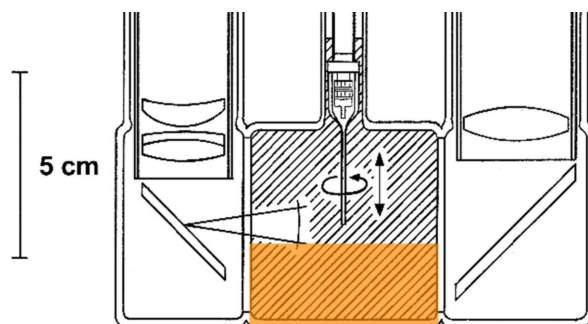


Figure 3.3: Detail of the growth vessel: The bottom is modified with a heating foil. It allows a much larger heating power than the 1 W used in the experiments.

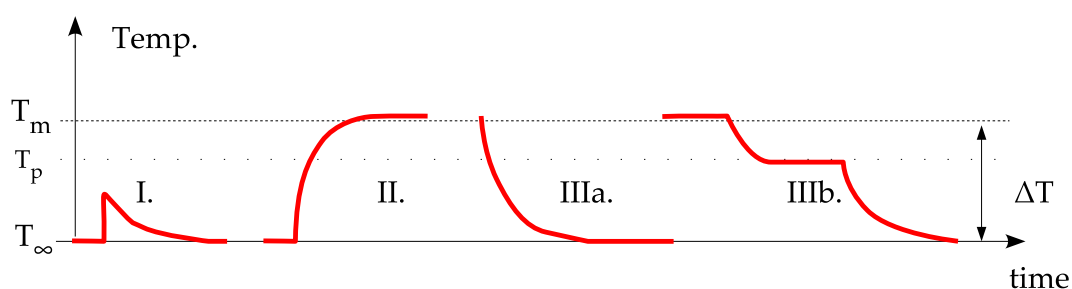


Figure 3.4: Three different investigated temperature trends: (I) Short heating pulse below the melting temperature T_m ; (II) Heating to above T_m and melting; (IIIa) Falling temperature without interaction; (IIIb) Falling temperature with a platform at T_p .

3.2.2 Shaker

The perturbation was generated by moving the crystal – located at the end of the capillary – back and forth. A piezo¹ was built in the structure above the capillary (see fig. 3.5). Its vertical oscillations are transformed into horizontal movements in one plane. The piezo elongation is amplified by the leverage from vertically $1.7\ \mu\text{m}$ to horizontally $\sim 10\ \mu\text{m}$ at the tip of the capillary. The plane of oscillation turns with the capillary.

Shaking The procedure for one run was as follows: After free growth for about 2 minutes the tracking (sec. 3.3) was started. The crystal was slowly moved upwards at the same velocity as the tip grew downwards, v_{\perp} . This exact velocity was unknown at this time of the experiment because of the different thermal expansion coefficients of the capillary mounting between the liquid xenon at 161 K and room temperature where the driving was applied. Rather the pattern recognition algorithm and the controlling server stabilized the crystal in the field of view. Again 2 minutes later it was supposed that a steady-state diffusion field and a convective flow had developed and then the perturbations were started. This assumption is also backed by the CFD simulations. Typically the crystal was shaken for a time interval t_1 with a frequency f , then

¹(PICMA® PL033 from PI, see appendix B)

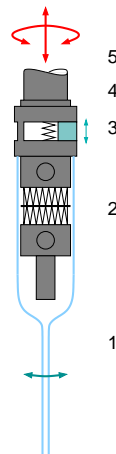


Figure 3.5: The capillary and the resulting degrees of freedom. (1) Glass capillary; (2) Peltier elements; (3) Piezo and spring, vertical movement is transformed to horizontal; (4) Supporting structure; (5) Degrees of freedom of the crystal positioning

it evolved freely for another interval t_2 . The two intervals t_1, t_2 and the frequency f could be chosen freely. To narrow the large range of controlling parameters – resulting from the combination of the mentioned perturbation and undercooling – and in order to isolate the mechanical from the temperature effects, the dimensionless undercooling $\Delta = \Delta T / (\Delta T) = \Delta T / (L/c_p)$ of the 20 examined runs was in a small range between 0.003 and 0.005.

3.3 Optical system and tracking

The spatial resolution for the observation in both experimental apparatuses was diffraction limited by the optical setup to $\approx 1 \mu\text{m}$. The growth process was recorded with a video camera at 756×581 pixels and additionally captured via a high resolution CCD camera at 1280×1024 pixels in the setup for the experiments on mechanical perturbations. The field of view is narrowed by the geometrical layout of the optical system. For the experiment on thermal perturbations this is no restriction, since melting prevented the crystal anyway from growing out of this region. But for free growth and the shaking perturbations this was a serious problem because one needed to readjust the vertical position of the crystal in the growth vessel by moving it. Stalder made use of this degree of freedom. By shifting the crystal downwards out of its steady-state temperature field, ‘washing-away the diffusion field’, he could induce the formation of doublons [33]. Now a continuous tracking system was implemented in order to minimize the effect of large position corrections. The camera was mounted on a high precision linear positioner. Together with the shiftable capillary along the z-axis these two degrees of freedom were used to keep the crystal tip fixed in the field of view of the camera. A pattern recognition software (developed by H. M. Singer) finds the position of the tip in a picture. This value is compared with a desired position and the difference is sent to a server software (developed by M. F.). The computer controls the linear drives for both the capillary and the camera position. This unique

mechanism allows to examine crystal growth over macroscopic distances for up to 40 minutes without noticeable, sudden perturbations (see sections 5.2 and 5.3).

The growth velocity is determined from the images by using an algorithm for the detection of the relative shift on the contours, see section 3.4.1.

3.4 Methods

3.4.1 Image processing

The experimental procedure results in a bunch of pictures and movies. These images need to be made accessible for numerical analysis. During the last years, an image processing toolchain was developed in our laboratory for this aim. The contour of the crystal image is found by an edge detection and contour finding algorithm (see reference [62] for details). During this work, parts of Singer's workflow proved to be insufficiently robust for the large amount of pictures provided by the now implemented long term growth experiments. This has not been a serious problem before when a crystal was observed for a maximum of 2 minutes before it left the field of view, resulting in about 100 pictures per sequence. Manual support for the automated contour finding process could be given within a reasonable time and effort. But for several thousand images it was not possible to do so any longer. An analysis revealed that most of the manual corrections had to be made in the *contour cleaning* step, i.e. after the edges are found, the outline has to be isolated, inner contours need to be neglected, clusters and loops removed. Singers heuristic algorithm was slightly enhanced and changed to a recursive form that does not get confused at contour branchings anymore. Rather it follows both ways trying to 'find a way out' and finally chooses the longest one with the least number of branchings.

The random spatial orientation of the crystal with respect to the plumb line results in a skewed projection. By a trigonometric transformation (see reference [63] for details) the contours are brought to original proportions.

For the tracked crystals another problem is the superposition of the images that has to be undone in order to find the temporal evolution of the shape and the tips. An algorithm has been developed to shift two contours accordingly. The idea is to take advantage of the morphological shape of the crystal that changes only a little between two images. The main tip grows and so do most of the sidebranch tips. The branchings however remain in their positions in the laboratory frame of reference. The later contour should thus enclose the former one like a glove. The question is: How to dress properly?

A measure for how well the glove fits is the sum of all distances between every point of a contour to the nearest point of contour one time step before. This distance is minimized and the resulting offset is saved. It corresponds to the tip movement between the two images. Applying this algorithm for a sequence of some dozens to hundreds contours, it is possible to reconstruct the growth of the crystal part in the field of view. An example on how it works is shown in figure 3.6.

The first implementation of this algorithm (done by O. Wittwer) again proved not to be fast

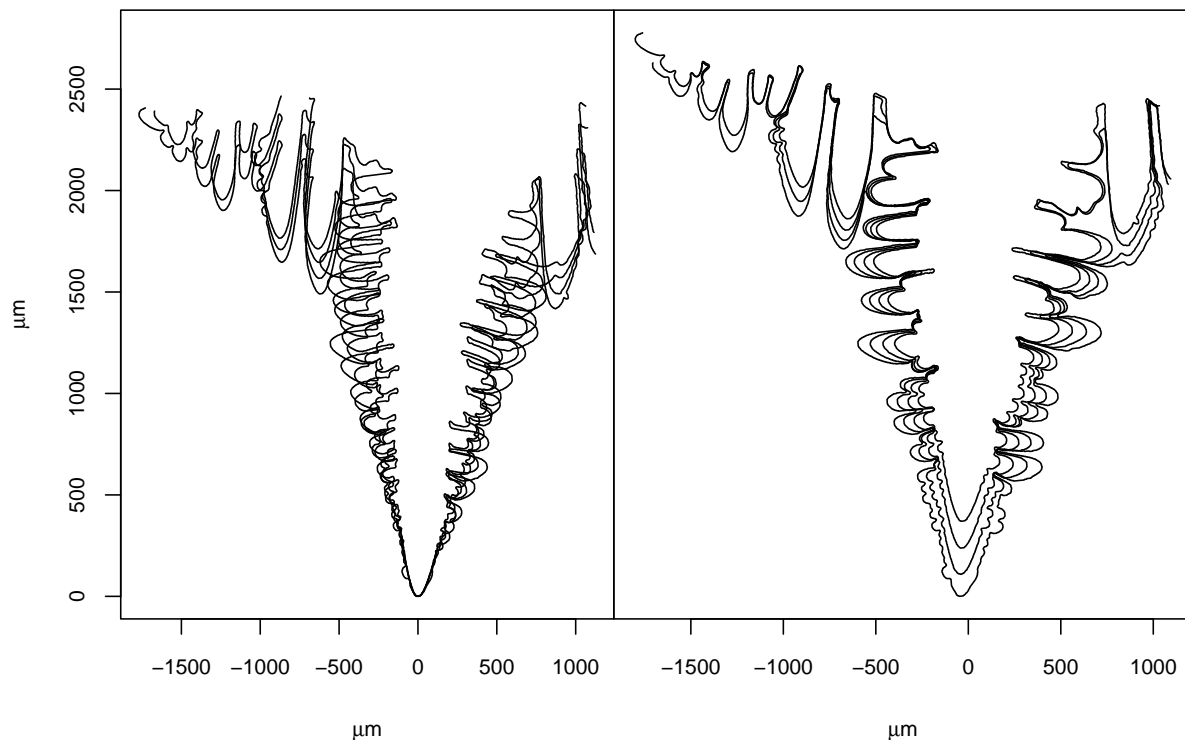


Figure 3.6: The effect of separation algorithm on a bunch of contours. **left** The contourlines are superimposed because of the stabilization of the tip in the field of view. The frame of reference is the main tip. **right** The *uncenter* algorithm shifts the contours and centers them in the laboratory frame of reference. The growth rate of the crystal becomes visible.

enough for many thousand pictures. The code has been optimized and accelerated by almost two orders of magnitude. This was only possible with the caveat of a little loss in precision. An analysis of the results of three different methods for a sequence of 300 contours showed no significant difference in the result. This can be seen in table 3.1.

3.4.2 Smoothing and filtering the noise

Pixelated images have the inherent problem of spatial discretization. The 'exact' solid-liquid interface is mapped to pixels at a scale of about $1.3 \mu\text{m}$ per pixel at best. This pixelation results in noisy signals and artifacts, and leads to large uncertainties, mainly for the two characteristic parameters for the radius ρ and the velocity v at the tip. One solution for this problem is to use averaging over some measured points, giving reasonable results, especially for systematic noise as can be found in the tip position and therefore tip velocity measurements. But averaging is not well suited for finding smooth contour shapes. It seems to be more useful to apply a low-pass frequency filter. Such a filter was implemented using wavelet transformation (WT). Compared with the Fourier transformation (FT) the WT preserves both, frequency and localization of the

	OW	MF1	MF2
mean shift value in Δy [μm]	10.84	10.57	10.56
change in %	—	-2.5	-2.6
variance change in %	—	+12	+19
time per image pair	359.2	23.7	8.6
change in %	—	-93.4	-97.6

Table 3.1: Three algorithms for contour shifting (*uncentering*) in comparison: Wittwer’s first implementation (OW) is taken as reference in precision and in time consumption. The two modifications (MF1 & MF2) give a slightly lower mean value combined with a higher variance. The striking feature is the almost two orders of magnitude better speed.

transformed function. Hence the time-frequency analysis for any oscillation phenomenon is less difficult with WT than with FT or the short-time Fourier transform (STFT). As in FT the filter corresponds to cutting-off some parts in the wavelet-‘spectrum’. In figure 3.7 two contours together with their smoothed counterparts (using WT) are shown. Both columns show three zoom stages of the same contour. The original data come from a video tape (left) and the high resolution CCD-camera (right). While no difference can be seen between the original and two different filtered data (superimposed) at the large scale, the detail reveals the effect of the low-pass filter. Depending on the quality (pixel resolution) of the raw data the cut-off has to be selected carefully between filtering effect and losing real information as can be seen in the third row. A cut-off at the wavelength λ_c corresponding to twice the pixel size in the space-domain has been identified as well-suited.

A wavelet filter with a cut-off frequency f_c corresponding to 8 datapoints was applied to a noisy velocity signal in figure 3.8. A comparison with averaging over $k \in \{8, 16, 32\}$ data points show that the averaging over 8 and 16 points show a bulge near 28 s, also seen in the filtered values, while the 32-point-averaging smoothes it out. The mean values are identical, but only the lossy averaging over 32 points has the same small variance as the filtering.

3.4.3 Local curvature

For the calculation of the local curvature of the contours, the filtered contour points (see section above) were expanded by a cubic-spline interpolation to a four times finer spacing. A parabola was then fitted over a sequence of 5 to 20 points to the left and the right of every point, depending on the radius of curvature, to find iteratively the local curvature at this point.

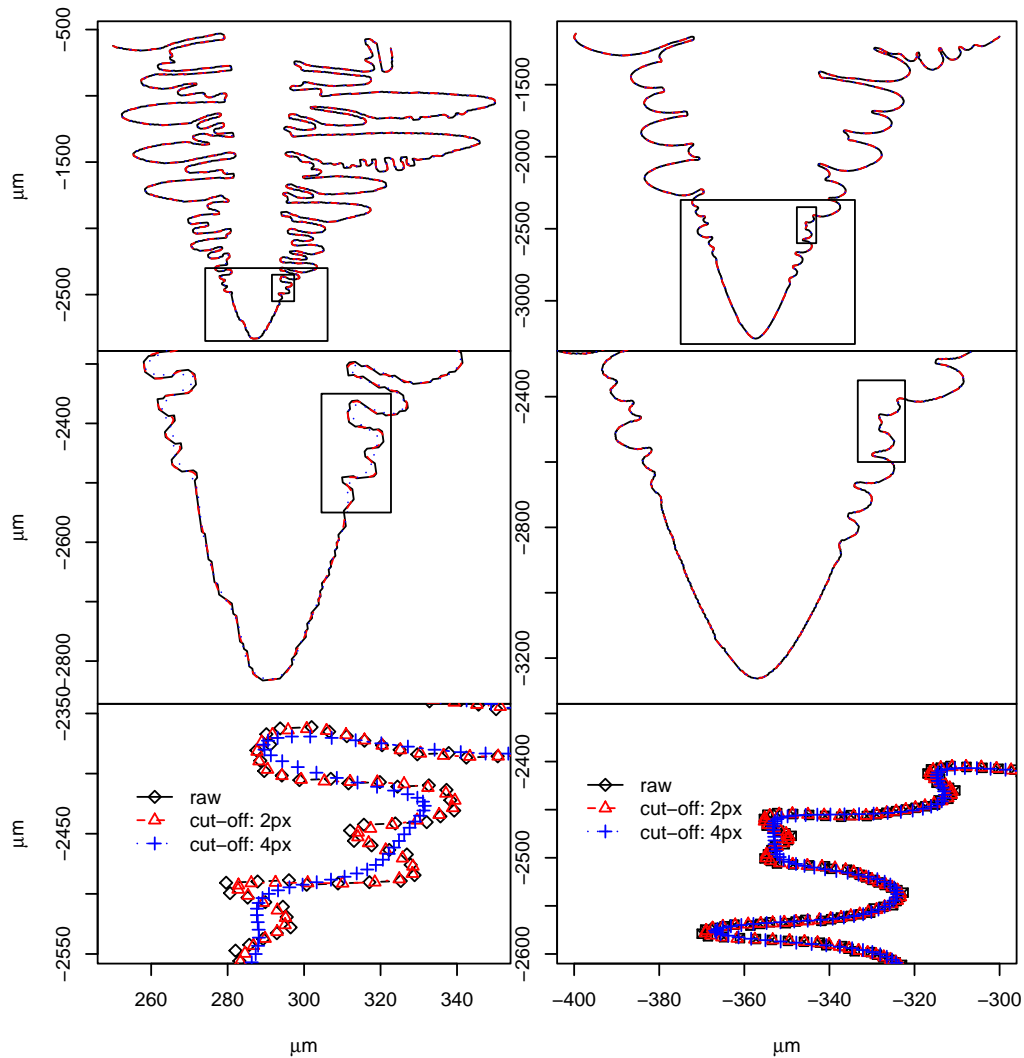
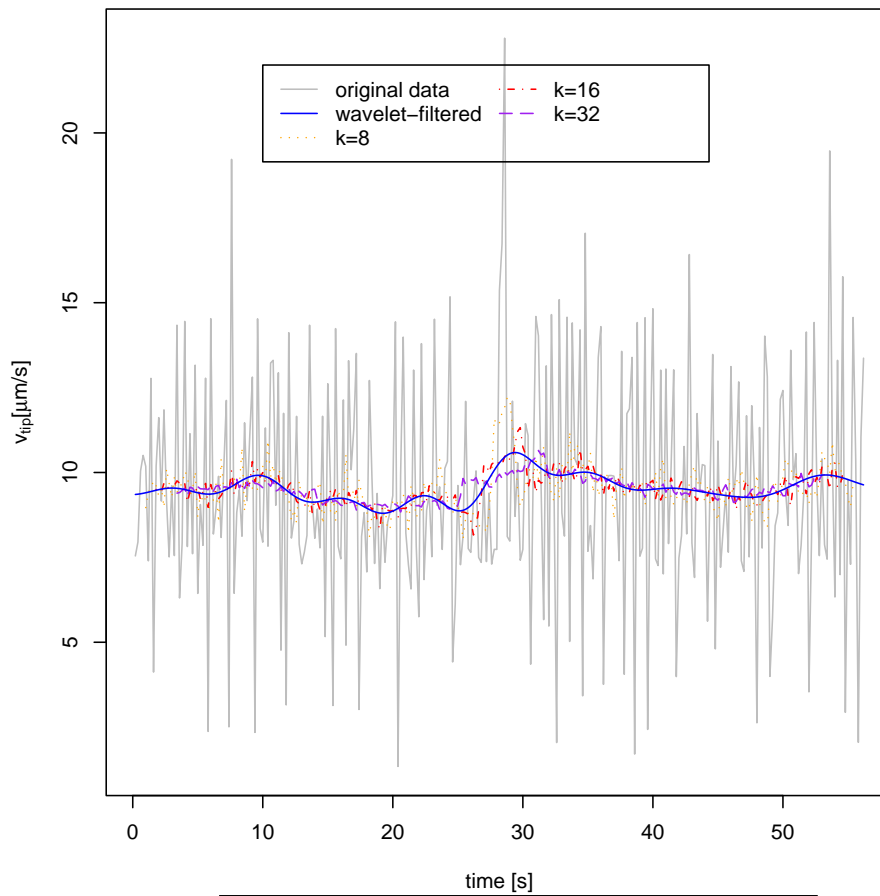


Figure 3.7: Two contours smoothed with wavelet transformations. Three zoom levels for each contour are shown, the panes are marked by the rectangles. The original data points (\diamond) are black and connected with a solid line. The filtered data (\triangle) with a cut-off wavelength ($\lambda_c \approx 2\text{px}$) is the red dashed line while the blue dotted line represents the filtered data ($+$) with ($\lambda_c \approx 4\text{px}$). While first filter reproduces the original data from both sources video tape (left) and CCD-camera (right) smoothly, the latter is lossy on both data sources.



technique	mean [$\mu\text{m/s}$]	\pm [$\mu\text{m/s}$]
raw	9.52	3.38
averaging (8 pt)	9.53	0.68
averaging (16 pt)	9.53	0.46
averaging (32 pt)	9.52	0.34
wavelet filtering	9.53	0.38

Figure 3.8: A timeseries for the tip velocity. The images behind this series were recorded on video tape @ 25 fps and grabbed to PC @ 5 fps. This explains the large variance in the raw data. Using averaging and filtering the noise is reduced. The mean values are almost preserved and the wavelet filtering gives about the same standard deviation as the averaging over 32 points. But the bulge near 28 s (visible in 8- and 16-points-averaging as well as in the wavelet-filtered data) can not be seen in the 32-points-averaging anymore.

Chapter 4

Experimental results

By heating and by shaking two very different perturbation mechanisms were applied to the growing crystal. The results can be categorized with respect to the framework mentioned in chapter 2.

4.1 Heating experiments

4.1.1 Controlled sidebranch initiation

Short pulse

Strong perturbations of the temperature field around the tip were experimentally identified by Stalder [33] to trigger a morphology transition to a dendritic doublon. Fluctuations in the temperature field, caused by transient convective flows were suspected by Wittwer [48] to be responsible for the 'spontaneous' initiation of so called P-type sidebranches (indicating *perturbation*-induced ones). By applying a sequence of single heating pulses (see fig. 3.4 type I), it was possible to test this hypothesis. An example is given by the contours of a growing crystal in figure 4.1. In this case three heating pulses with a power of 0.9 W lasting for 15 s each, separated by a time interval of 360 s were applied. The undercooling, measured by means of a Pt-100 in the lower part of the growth vessel, changed from 150 mK to 90 mK in less than 30 s and relaxed back to 150 mK in the next 300 s. This cycle was repeated twice. In the figure — the picture has been taken one minute after the third heating pulse was measured — one clearly identifies two dominant sidebranches pairs: one at 2350 μm , the other at 1250 μm above the tip. A third pair of sidebranches has just emerged very close to the tip (150 μm), corresponding to about 5 tip radii, and is about to develop into a new dominant one, showing the characteristics of P-type sidebranches. Between the dominant sidebranches with equidistant spacing Λ , one observes random non-symmetric sidebranches.

This *active* sidebranch initiation was performed successfully with different undercoolings ΔT in the range from 100–300 mK. It was not possible to separate the *noise*-induced (N-type) sidebranches from the P-type ones at higher undercoolings. Then sidebranch spacing became

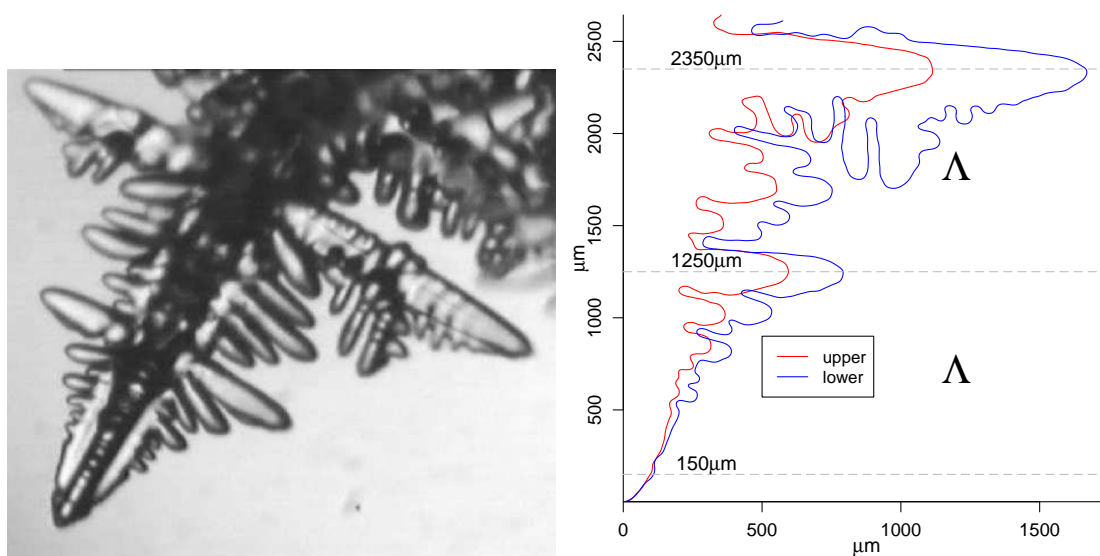


Figure 4.1: Dominant sidebranches are initiated by a well-defined temperature rise. On the left hand side the crystal is shown as picture, while on the right hand side its contours are plotted. Both sides of the dendrite, left and right, are shown superimposed for better comparison. The temporal intervals of 360 s between heating perturbations lead to spatial intervals $\Lambda = 1100 \mu\text{m}$ of the dominant sidebranches. They are found on both sides at the same distance behind the tip, thus they were initiated at the same time.

too short for a proper contour extraction (i.e. about twice the pixel size). The difference in the time they show-up between the P-type sidebranches starting at the very tip and the N-type ones starting only a little behind was too small for a visual identification by their respective size in the greyscale image.

Heating gives rise to additional convection and the xenon flow reaches the tip after some time. (For a simulation on convection in macroscopic scales, see chapter 5). The time interval between the starting of the heating and the first visible indications of a change in the tip shape (early sidebranching) was measured to be about 60 s. This perturbation by the 'warm' convective flow is large compared to the thermal fluctuations in the xenon due to the $k_B T$ fluctuations of the atoms and induces a P-type sidebranch.

While the tip radius R grows massively ¹, the tip velocity shows an opposing behavior to the temperature rise (see fig. 4.2), it decreases before relaxing back to the initial value. The tip does not split but sidebranches start growing at the tip. The radius slowly decreases back to the steady-state value as the temperature falls, and the following sidebranches grow randomly on either side. Compared to the reaction of the tip velocity upon the heating pulse, the radius has a lag of about 25 seconds.

¹The tip radius is denoted by R in the following to indicate the experimental way of finding it (with all related problems, see references [64, 63]) and to distinguish it from the ideal theoretical tip radius ρ .

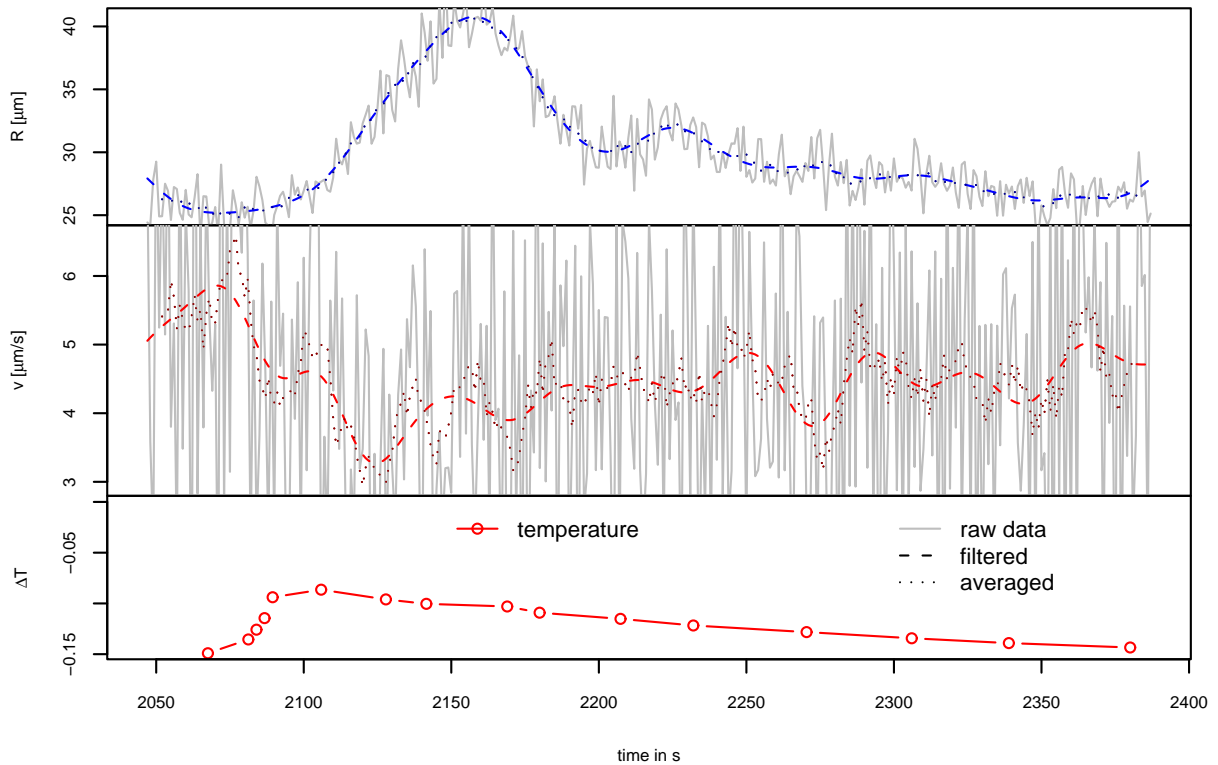


Figure 4.2: One of the three heating pulses leading to the contour seen in figure 4.1. The noise in the original data (plain grey curve) is due to the pixelization, the dashed curves are filtered (the cut-off wavelength corresponds to 10 datapoints) while the dotted curves are averaged (over 10 points). The radius reacts massively but with some lag upon the temperature rise, the velocity instantaneously becomes slower. Both parameters relax as temperature keeps dropping to the initial value. The sidebranches are visually identifiable at $t \sim 2200 - 2220$ s.

Melting-growth transition

In another sequence of investigations (see fig. 3.4, type II) the xenon was heated to a temperature $T > T_m$. For the first seconds of temperature rise, this corresponds to the 'short pulse' in the section above. But since the melting temperature T_m was reached within 5 minutes, the newly born P-type sidebranches could not evolve and were melt away just seconds later. The melting regime was held for some minutes, causing more and more sidebranches to disappear. The tip radius decreased to a steady-state value, the velocity became negative. When the temperature began to drop (fig. 3.4, type IIIa), the now smooth shaped tip restarted growing. In figure 4.3(a) four snapshots of this transition are shown. The corresponding values for the tip radius and the tip velocity as a function of time can be seen in figure 4.3(b).

The tip showed an isotropical sphere-like growth *with increasing radius* in the first minutes of falling temperature. Within seconds, the tip selected a new sharp tip and growth rate, corre-

sponding to the current undercooling. The system falls into the basin of attraction for dendritic growth. During this sudden selection of a new operating point, symmetrical sidebranches are initiated. Focussing on the shape of these new sidebranches, it is easily seen that they are different from the P-type ones: They have doublon-character, as can be seen in the last picture in figure 4.3 and in the sequence in figure 4.4. The lower doublon constituent shows always an additional structure growing in a 45° -angle to the main axis. This structure is further investigated in section 4.3. To clearly separate the sidebranches initiated during the change from melting to growth and because of their reproducible characteristic shape, they are called *T-type sidebranches*. This name indicates their origin in a transient temperature drop.

4.1.2 Evolution of the tip parameters

The main parameters to characterize steady-state dendritic growth (section 2.1) are the radius R and the velocity v of the main tip which show up in the inverse of the stability constant σ^* . The temporal developments of these two parameters are also useful to characterize transient states. The product R^2v means a *solidification rate*. The name *stability constant* is omitted in this section.

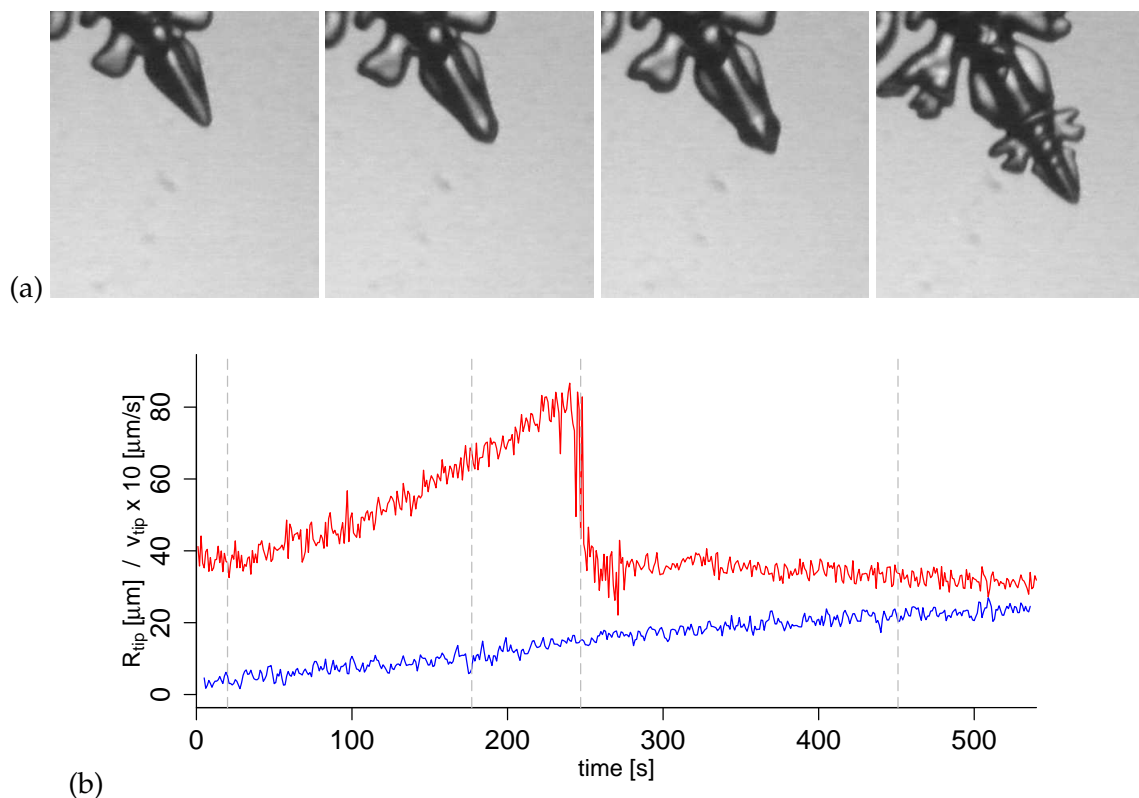


Figure 4.3: (a) Four snapshots of a dendrite tip growing during falling temperature. The smooth shape at the beginning becomes sphere-like, the radius grows. Then suddenly a new sharp tip evolves and the sphere deforms to lobes at both sides that give rise to a characteristic sidebranch shape. The vertical lines in (b) indicate the pictures.

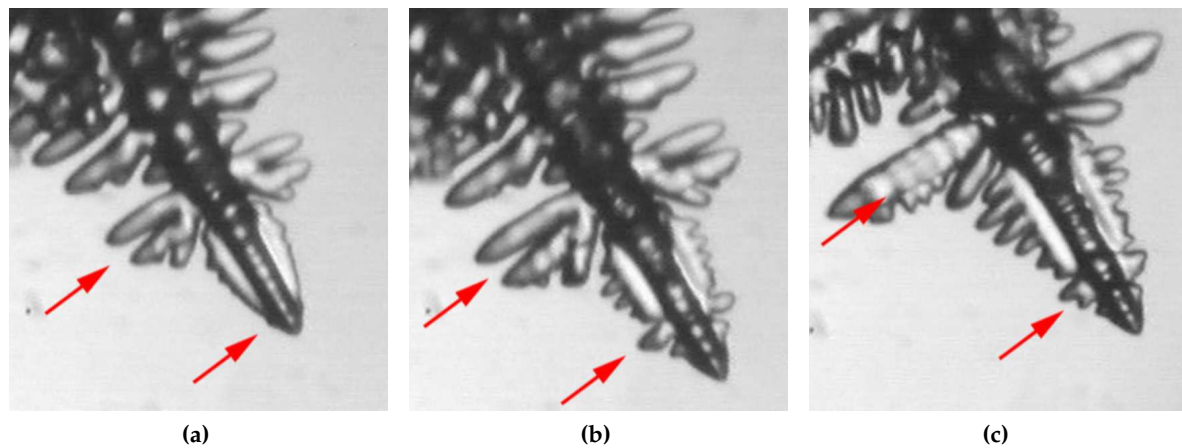


Figure 4.4: The characteristic shapes of the new *transition-initiated sidebranches* (T-type) in comparison with the P-type sidebranches. **(a)** The dominant doublon-like *T-type* sidebranch was initiated by the falling temperature transition. A heating-pulse caused a P-type sidebranch starting at the tip. **(b)** Two minutes later, the T-type sidebranch structure has grown larger, the doublon character is still visible. The P-type sidebranch has become dominant in its surrounding. **(c)** The same crystal 5 minutes later shows the now dominant P-type sidebranch and the beginning of another P-type branch. The T-type sidebranch has left the field of view.

It would mislead – by its origin – to a steady state growth. These parameters are plotted for typical temperature trends in figure 4.5.

Tip velocity: The tip decelerates for rising temperatures. As long as the temperature remains above the melting temperature T_m , the tip shrinks, hence its velocity is negative. The tip velocity accelerates with falling temperature as expected. The transitions from growing to shrinking are smooth. The tip velocity has been found to react almost instantaneously on changed temperature in accordance with Koss' experimental [25] and Steinbach's numerical [65] observations.

Tip radius: The radius of the tip on the other hand *increases after any perturbation*. A rising temperature, either caused by a single pulse or by the initiation of a melting phase, always triggers the formation of sidebranches (P-type). An indicator for this formation is the temporary increase of the tip radius. Once the temperature T exceeds T_m , the radius becomes smaller until it reaches a steady state value about 5 minutes later. This constant value was observed in a different experimental setup by Glicksman and Lupulescu in microgravity [66, 67], before the melting crystal became so small that capillarity effects set in. The bulges one observes during the melting phase (*red, plain arrows* in figure 4.5(a),(b)) are caused by a shrinking sidebranch disappearing at the tip. This sidebranch does not necessarily have to be an former P-type sidebranch.

The sharp rise in the tip radius and the even sharper drop to a new value, followed by

another small bulge (*blue*, dotted arrows in figure 4.5(a),(b)) during a continuous drop is characteristic for the T-type sidebranching in falling temperature. It is remarkable that the first sharp drop in the tip radius takes place when the undercooling $\Delta T(t)$ is at $(0.60 \pm 0.048)\Delta T$. The small bulge, indicating the second finger of the doublon-like sidebranch structure arising is at $(0.72 \pm 0.057)\Delta T$. These values are measured for undercoolings of about 250 mK. In another run with about 160 mK undercooling, this hysteresis effect was found at $(0.69 \pm 0.055)\Delta T$ and $(0.79 \pm 0.064)\Delta T$ respectively. No difference in the maximum tip radius could be found. In all cases the radius reached between 48 and 55 μm measured by means of the local curvature.

The observation of a dominant sidebranch as reaction of a change in the growth environment is consistent with a similar observation of Koss [25]. Because of experimental limitations he could not see a maximum-area projection of his crystal and could not find the symmetry of the induced P-type sidebranches.

Solidification rate: While the value R^2v near the tip changes from a *growth* rate to a *shrink* rate during the heating phase, it mirrors the behavior of the tip radius R in the transition back to growing. In a recent paper, Steinbach et al. [65] reported on the evolution of these values during transient growth simulations. He found the tip velocity to respond almost instantaneously on changed temperature and to 'overshoot' initially. After this abrupt change, the velocity slowly approached the steady-state value. The variation of the solidification rate showed a constant value except for a pronounced spike immediately following the temperature change.

In the results presented in figure 4.5 the temperature does not change instantaneously as in Steinbach's numerical experiment. The spike in the solidification rate is correlated with the increase in R during the falling temperature. It can be seen in figure 4.5(a) that the solidification rate is essentially constant after the spike at $t = 1500\text{s}$. Even during the short heating pulse phase, the solidification rate remains at about $3000\ \mu\text{m}^2/\text{s}$. In figure 4.5(b) the shrink rate during melting is found to show a good stability at about $-2500\ \mu\text{m}^2/\text{s}$ during the melting phase.

The observations of a growing tip radius during the first moments in the transition to growth and the emergence of these tips is also found by Dougherty and Nunnally [26].

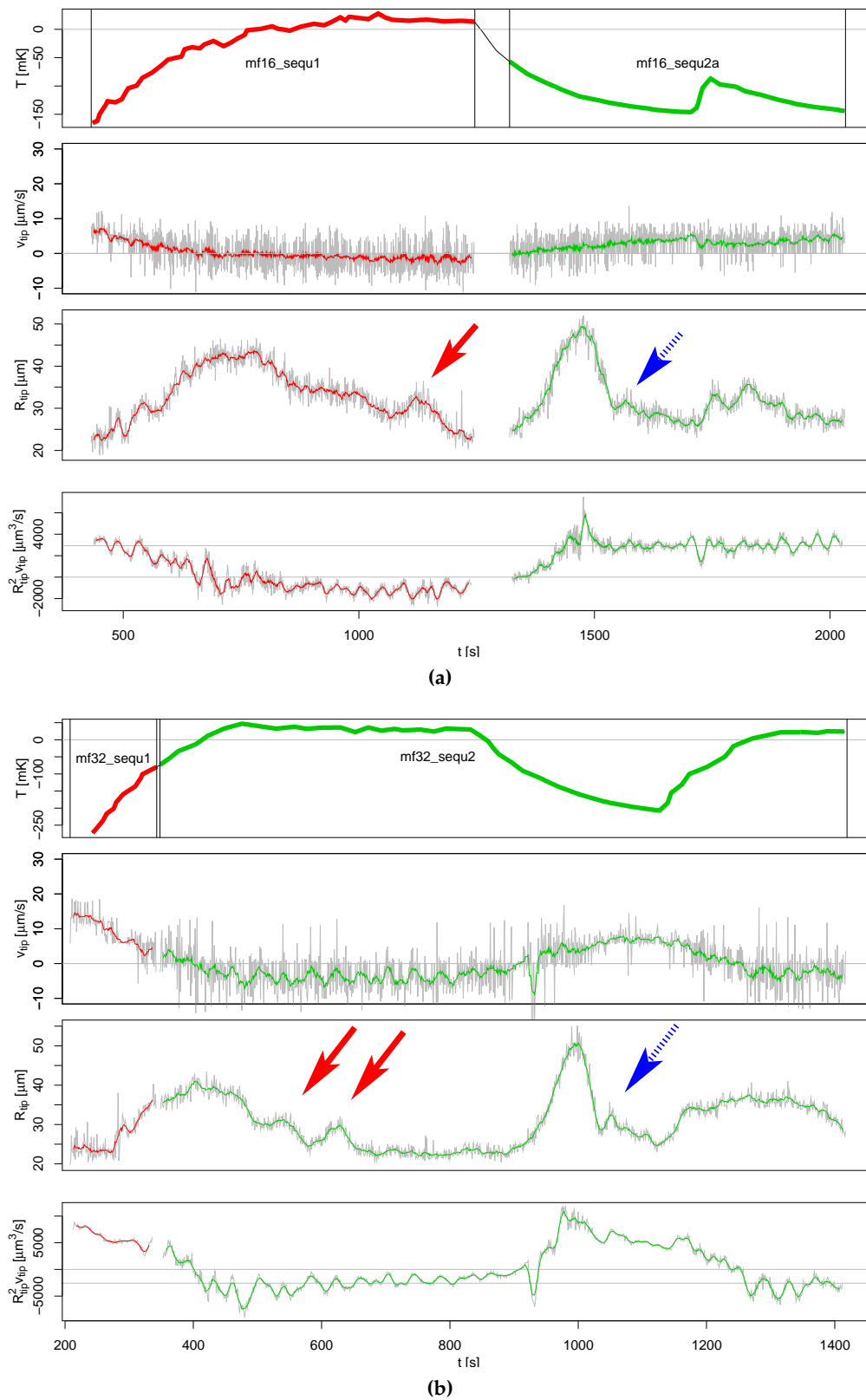


Figure 4.5: The temporal evolution of the characteristic parameters of the main tip. The temperature trends I, II, IIIa (fig. 3.4) are shown. The arrows indicate disappearing side-branches (red, plain) and the typical doublon birth in T-type sidebranching (blue, dotted).

4.2 Shaking experiments

4.2.1 Inclination and twist of the growth axis

In total 7 different runs a misorientation in the crystal was observed after start (in 5 cases) or stop (one single case) of the periodic perturbations. One event was found after an unidentified accidental perturbation of the tip. Inclinations in the growth axes were measured in the observation plane between $1.5 \pm 0.2^\circ$ and $8.2 \pm 0.2^\circ$. No dependence on the angle between observation and oscillation plane was found, inclinations were measured when the oscillation plane was the same ($\pm 10\%$) as the observation plane and also when the planes were perpendicular ($\pm 10\%$) to each other. While in some cases the main axis was restored after the perturbation was switched off, the inclined growth axis persisted in others. A closer look at both of these types (see fig. 4.6) reveals two different mechanisms. The more distinct inclinations are caused by a sequence of cascading tip splittings that preserve the main axis. The errant tips can switch back, i.e. stop splitting and continue growing along the main axis. The other less pronounced inclinations do in fact change the main growth axis. It is important to keep in mind that these inclinations are not 'breaks', i.e. the crystal does not break at some point in its structure. Rather at some time, the tip changes its growth direction. A sequence of contours showing the temporal evolution of the inclination is plotted in figure 4.7. Because the changed spatial orientation of the $\langle 100 \rangle$ -axis begins at the specific tip position in the moment of perturbation changes, and because the exact liquid flow at microscopic scale at the tip during shaking could be quite complicated, the non-alignment of observation and oscillation plane could be considered as random.

A second change in the growing crystal structure was observed as a *twist* along the main axis. Unfortunately only one single instance of this twist was found in the shaking experiments.

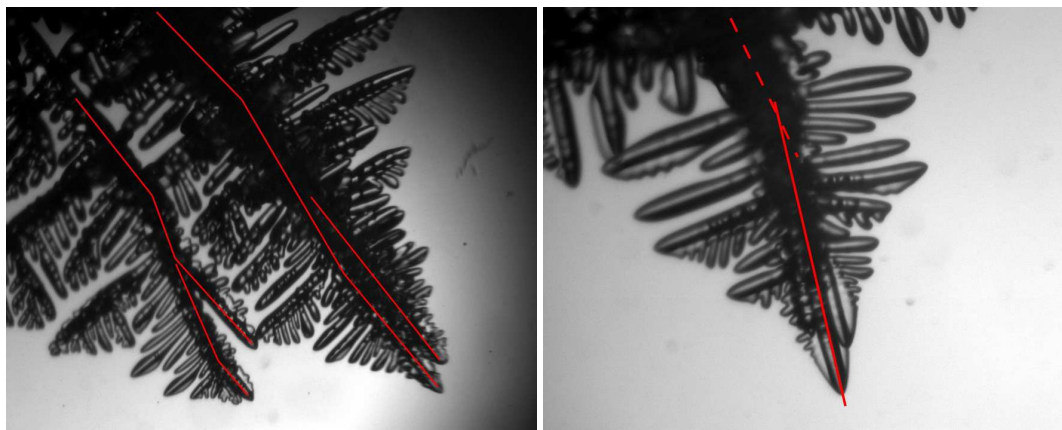


Figure 4.6: Different types of inclinations. **left:** The tip performs a series of tip-splittings, but preserves the original growth direction. This allows the growth direction to switch back to the original one, either spontaneously or after stopping the perturbation. **right:** The crystal suffers a change in the direction of its $\langle 100 \rangle$ main axis. The original orientation is shown by a dashed line, while the plain line shows the new growth direction, the angle is about 11° before the geometrical correction.

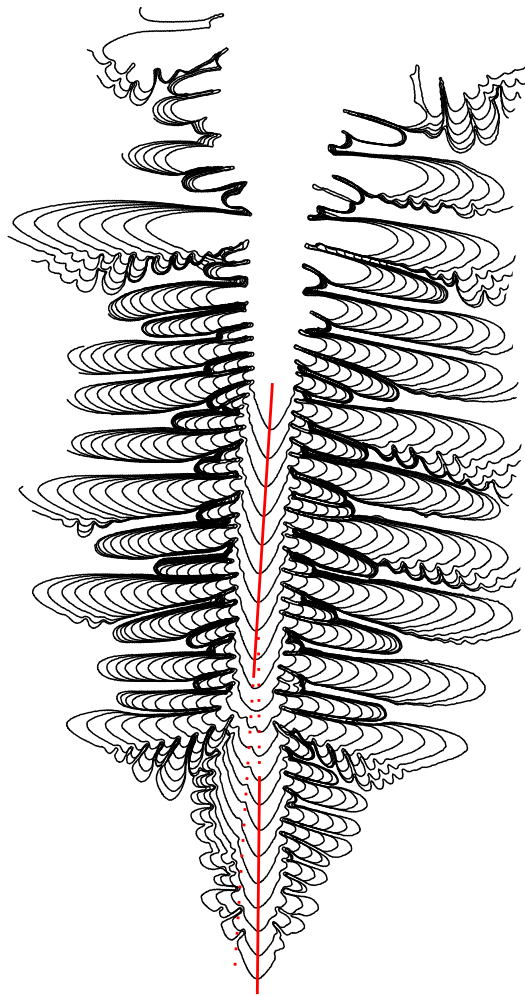


Figure 4.7: A sequence of contours showing the temporal evolution of an inclination. The change of the direction of the growth direction happens as the tip splits. After this tip instability, another main tip dominates the growth, but its $\langle 100 \rangle$ –axis is inclined by about 2° to the axis before.

It is shown in figure 4.8(a). In the upper part of the picture, the crystal is oriented in such a way that one clearly identifies a bright line in the crystal structure center. The light traversing through the melt is refracted at the solid-liquid interface because of the difference in the refractive index (see Appendix A). The larger the angle between the interface normal and the light beam, the more is it refracted and the darker appears the structure.

Above the marker line one can not see any of the fourfold symmetric fins on the trunk, they appear dark. Below the marker, there are fins visible and the bright trunk is slightly shifted. The twist occurred during growth, when the tip was at the position of the marker. A possible explanation for this visible ‘failure’ is a rotation of the crystal around the growth axis as depicted in the schematic cross-section in figure 4.8(b). The observation of this twist was made incidentally, after the orientation of the projection was changed, i.e. the capillary was turned.

This turn happened about 200s after the actual twist of the growth direction must have taken place, determined from the distance between the distortion at the marker line and the actual tip position.

It is not possible to see the twist in other pictures from earlier in this run, which makes it difficult to determine the exact time when the growth axis changed the direction. However within the questionable time frame, a tip split induced by a changed perturbation occurred, and a small torn of the capillary was performed.

In earlier experiments, fast turn of the capillary and therefore of the crystal in its melt caused tip splittings (similar to Stalder's doublons) but a twist in the growth direction has not yet been observed. It can therefore be ruled out that the shear flow of liquid along the surface of the tip during the small turn is the only reason for the observed twist. More probably, the combination of an unstable microscopical interface, caused by the perturbation and the shear flow due to the capillary turn at the same time, can be assumed to be the reason for the crystal to continue to grow along a twisted $\langle 100 \rangle$ -axis.

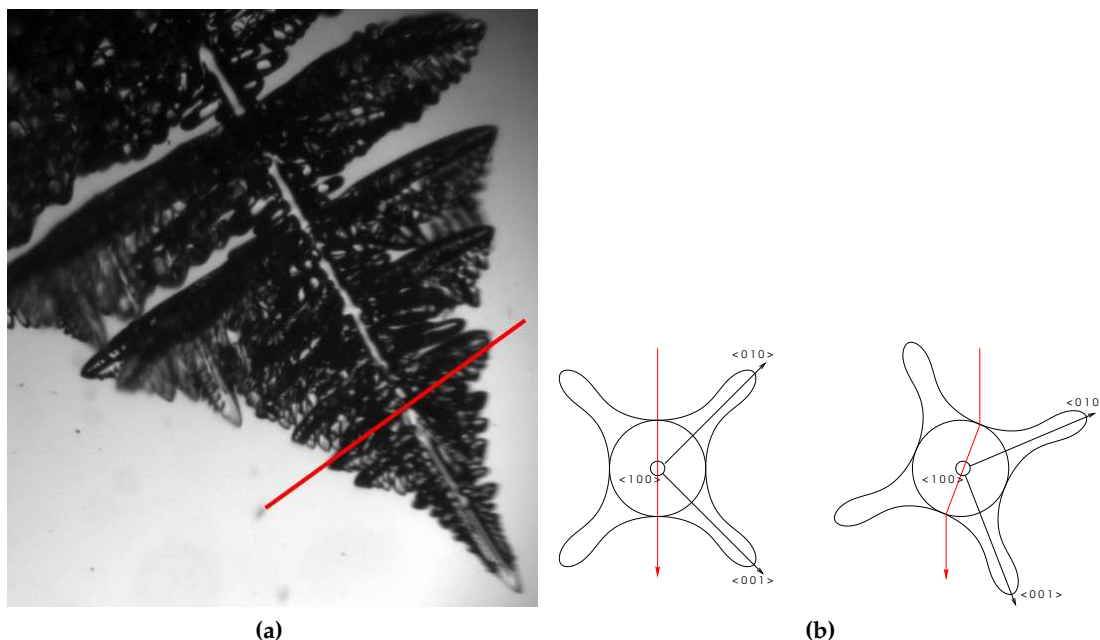


Figure 4.8: left: (a) The crystal is oriented in such a way that the light line of the trunk is clearly visible above the marker (the light is passing through the most inner part of the dendrite). Note that below the marker the trunk line is shifted while the fins are identifiable. The two gaps in the sidebranch structure separate one dominant P-type branch from its random neighbors. It was triggered by the start of the perturbations almost 6 minutes before the picture was taken. (b) The scheme shows the path of light through the trunk and the orientation of the crystallographic main axes before and after the twist.

4.2.2 Morphology stability

Without any changing of the growth environment, spontaneous formations of multi-tip-configurations evolving from a dendritic tip has been observed before [68, 63]. These *multiplons* decayed within 30 s to 3 min to a dendrite again.

In the 20 examined sequences with shaking perturbation, 18 tip-splitting events at the main tip were found. Three of them showed up spontaneously while no perturbation was applied, they decayed within 60 to 200 s. Another three showed up during oscillation and also decayed about 200 s after the perturbations were stopped. Most tip-splittings were induced by starting the perturbations as one could expect, only a few could not be correlated to the applied perturbations. There were six tip-splittings found that led to a doublon or to a multiplon (by a sequence of splittings) that was stable as long as the oscillatory perturbations were continued and the observation was possible. This is 260, 420, 500, 540, 1400 and 1500 seconds. The oscillations covered a large range from 1/60 Hz to 2 Hz and no influence of the frequency was found.

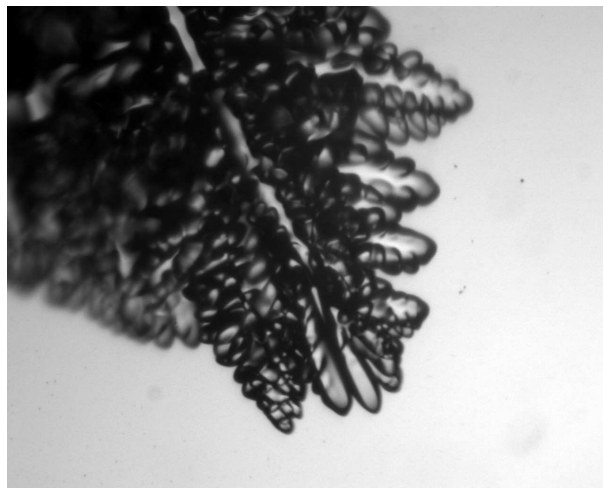


Figure 4.9: A multi-tip-configuration showing three main tips are growing close to each other. This multiplon was stable for the following more than 20 minutes.

4.3 Cascading tip-splitting

In experiments with both kinds of perturbations, melting and shaking, tips growing in an oscillating mode were identified. This means either a **periodic splitting** or a **periodic sidebranching** in the tip region took place for up to 5 minutes. While the sidebranching led to structures on all sides of a growing tip, the splitting led to new tips with new growth directions. These tip-splittings have to be distinguished from the multiplon formation where the multiple tips preserve (almost) their main growth direction. The cascading splitting reported here took place once to the one side, then to the other periodically (say alternatively to the left and right), and the angle between the two new tips was found to be constant during such a splitting sequence, typically 45° as shown in figure 4.12. The periodic early sidebranching can also be interpreted as a tip splitting into three (or five considering the 3D shape), whereas two (four) bulges on the two (four) sides of the tip degenerate into sidebranches. Figures 4.10(a)-(c) show three examples for each of the mentioned events. The first (a) and the last one (c) were found in the shaking, the middle (b) in the melting experiments.

The cascading tip-splitting led to periodic first order (c) and second order (a) sidebranches. While the cascading tip-splitting as in (a) never showed up spontaneously but always in correlation with shaking, (b) was found to be characteristic for the T-type branching after a transition to low temperatures and (c) could be found as reaction upon perturbation as well as spontaneously.

The cascading tip-splitting mechanism seems to be a universal concept. Utter et al. [69] report on it at the main tip in directional solidification and Karma and Lobkovsky [70] found it in a phase-field simulation on crack propagation. The consecutive splittings into $\langle 100 \rangle$ – and $\langle 010 \rangle$ – direction results in a trunk along the $\langle 110 \rangle$ – axis. Similar structures have been found by Henry, Minghetti and Rappaz [71] in aluminium alloys.

The temporal evolution in the highlighted regions seen in figure 4.10 is depicted in the contours in figure 4.11. The visually observed sidebranches tips in a cascading region have been marked when they were clearly formed, then the positions were tracked backwards in time. The contours have been rotated and stretched in order to make the shapes appear in true relations.

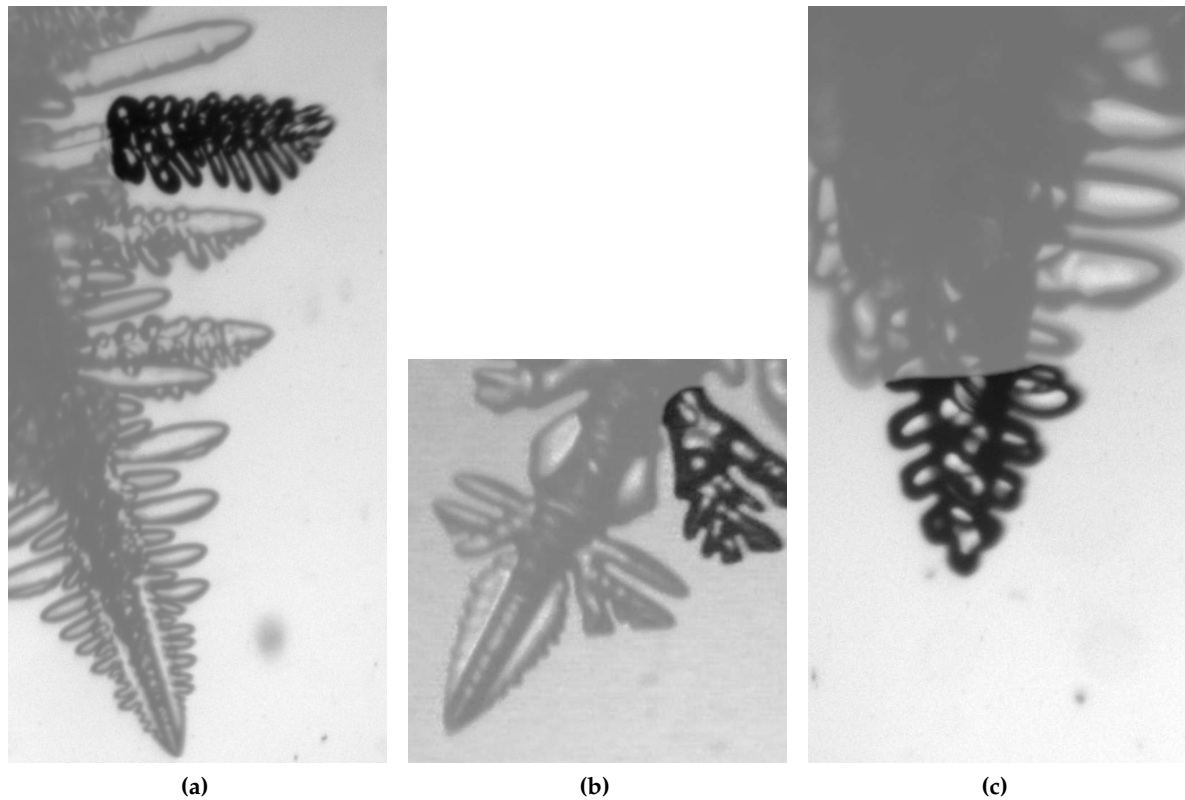


Figure 4.10: Alternating tip-splitting, *cascading*, on three different situations. (a) The sidebranch tip shows a sequence of periodic tip-splittings in alternating directions. The final direction is parallel to the initial one. (b) The 45° -structure in a typical T-type sidebranch structure. Its tip performs an periodic alternating splitting. (c) One tip in a multi-tip configuration. The dendrite shows periodic sidebranching alternating to the left and to the right.

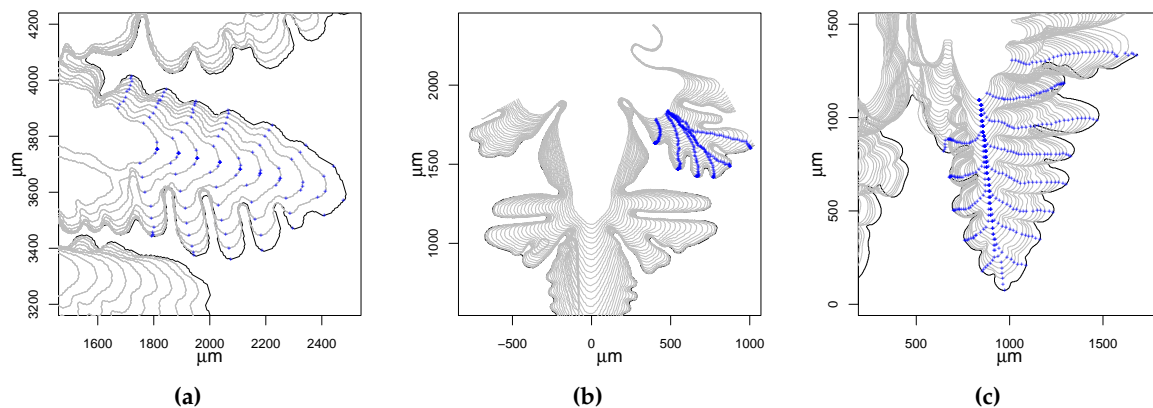


Figure 4.11: The same tip-splittings shown in figure 4.10 are plotted in the temporal evolution. The tips of the branches are marked on the last contour and tracked back in time. The time interval between the points is 10 s.

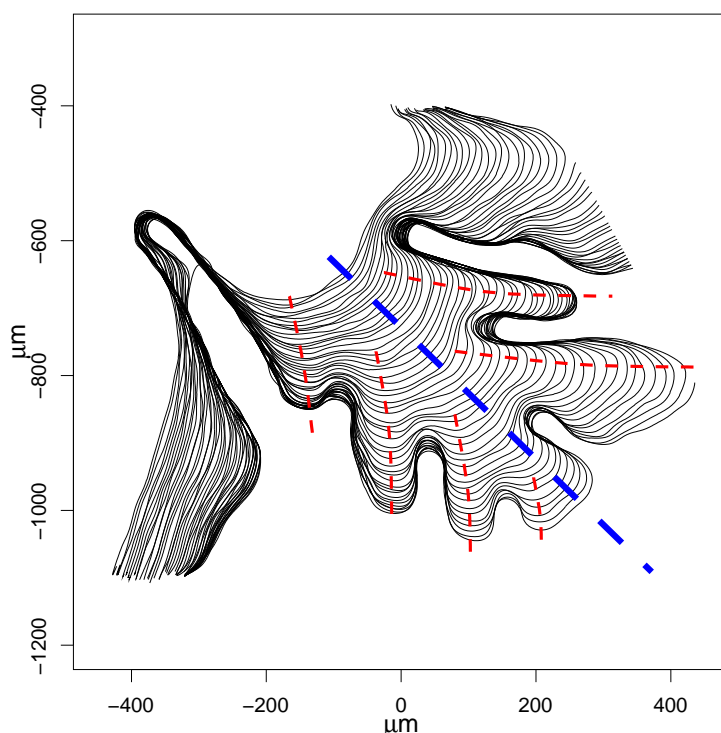


Figure 4.12: A detail of figure 4.10(b), the typical T-type sidebranch. While the main direction (dashed blue line) of this structure is 45° against the dendrite tip's $\langle 100 \rangle$ -axis, each alternating branching leads to second order branches again in a 45° -angle (dashed red lines).

4.4 Tip velocity

The tip velocity was analyzed in three situations: (i) unperturbed, (ii) in the transition from free growth to the tracked tip (see sect. 3.3) and (iii) in the transition from unperturbed growth to shaking perturbations.

(i) free growth The tip velocity for free growth was determined to be $v = 188.8 \cdot \Delta T^{1.745}$ by Bisang [11] in a temperature range $50 \text{ mK} \lesssim \Delta T \lesssim 200 \text{ mK}$, i.e. $0.001 < \Delta < 0.0039$ dimensionless. The temperature range has been expanded in this experiments, ranging to about 300 mK , i.e. 0.006 . While for 5 different dendrites grown at an undercooling of $175 \text{ mK} < \Delta T < 225 \text{ mK}$ Bisang's model is confirmed with a variance of about 5%, the tip velocity for 4 dendrites in the range $258 \text{ mK} < \Delta T < 278 \text{ mK}$, i.e. $0.005 < \Delta < 0.0054$ is about 20% below this value.

The reason might be found in two different mechanisms. On the one hand, the viscosity η of the liquid xenon increases with increasing undercooling ΔT . This causes a slower v_{tip} [72]. On the other hand the advection flow slows down a growing dendrite [73], which becomes more important on larger growth rates.

(ii) Tracking enabled The numerical results in chapter 5 show that the convective flow is of the order of magnitude of about $200 \mu\text{m/s}$, thus much faster than the tip velocity of about $10 \mu\text{m/s}$. During the tracking the tip velocity relative to the convective flow from below decreases further since the vertical tip movement v_{\perp} is neutralized. The tip velocity was measured before and after the tracking was switched on for three undercoolings $212, 261, 278 \text{ mK}$ and was found to drop by 20, 8, 5% respectively.

(iii) Shaking perturbations enabled No clear results were found for the change in the tip velocity after the shaking was enabled. While a shaking with 2 Hz at 209 mK led to a drop of the velocity by 10%, a shaking of $1/6 \text{ Hz}$ at 258 mK and 261 mK resulted in an unchanged and in a 8% higher velocity respectively.

4.4.1 Tip velocity oscillations

In figures 4.5 another effect in the tip velocity is visible. While the four oscillations in the last 200 seconds of the sequence `mf16_sequ2a` in figure 4.5(a) can not be identified clearly in the original data (grey) and therefore could be an artifact of the wavelet filtering, the seven oscillations of the (negative) tip velocity between 600 and 900 seconds in figure 4.5(a) are visible also in the raw data. A more detailed plot of the same regions is seen in figure 4.13. This plots reveal that in both sequences the oscillations are visible in the filtered and the averaged values for the tip velocity.

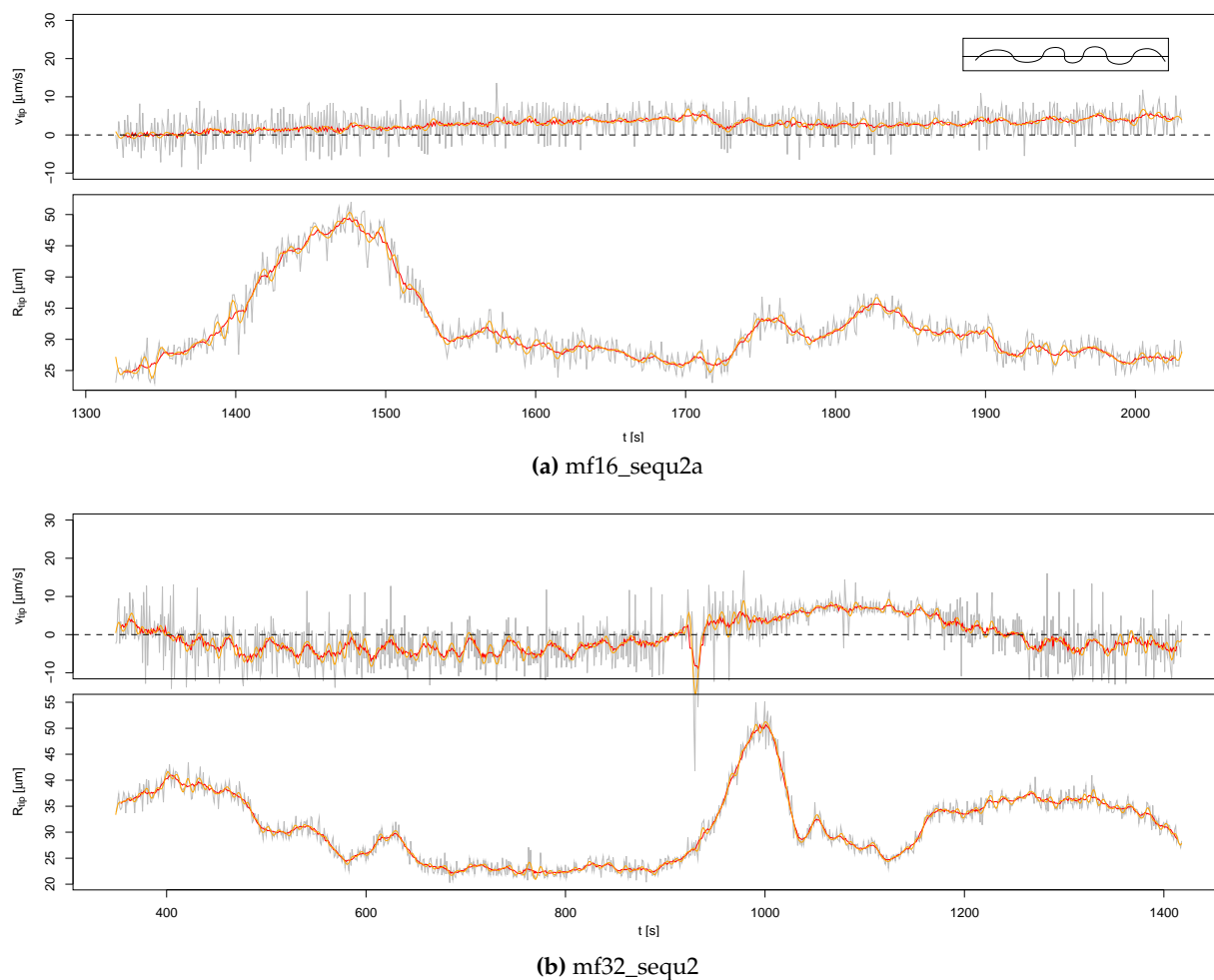


Figure 4.13: The oscillations in the tip velocity are visible in the filtered and in the averaged values for these two examples. This is a clue against wavelet transformation artifacts. **(a)** The timeframe from about 1900 s to 2000 s where oscillations are visible is emphasized in the inset. **(b)** The oscillations are visible in the melting phase between 400 s and 900 s and in the growth phase from about 1100 s and 1200 s.

4.5 An application: Dendrite Engineering

4.5.1 Symmetry

The controlled initiation of sidebranches of both types P and T (described in section 4.1.1) was observed to give rise to a pair of sidebranches synchronously. In fact all these 'pairs' are double pairs, one in the image plane and one perpendicular to it. Comparing the two perpendicular pairs by turning the capillary by 90° fourfold symmetric sidebranching is observed as shown in figure 4.14(a),(b). The superposition of the four outlines (fig. 4.14(c) top) shows the good agreement of the four shapes including the sidebranches. The first lobes on all four contours show an excellent correlation, while the more evolved sidebranches (they have grown for a longer time since they symmetrically have emerged) start to be influenced by random processes,

independent from each other. Plotting the local curvatures of the contour starting at the tip (fig. 4.14(c) bottom) gives a more quantitative way to demonstrate the symmetric shape of the sidebranches on the four fins. The maxima and minima coincide over a large distance. The correlation decreases in the region of the second T-type sidebranch. The two structures on the right hand side of (a) and (b) grow a little faster than their left hand counterparts. The reason is probably the slightly cooler surrounding on the lower side of the crystal that is exposed to a stronger convective flow. It is also shown that the difference between both sides is less for the view turned by 90° in (b). This is due to the fact that the inclination against gravity and therefore the difference in the convective flow on either side is smaller than in (a). The same plots for a freely grown crystal (fig. 4.15) shows no symmetry except at the very tip.

By periodically applied cycles of heating until melting smoothed the crystal and the following transitions to growth, shapes as shown in figure 4.16 were obtained. The symmetry is visible in a 45° -projection (fig. 4.16(a)). The right hand side of the crystal in this picture shows longer sidebranches. Another example is shown in figure 4.16(b) in maximum-area projection. There are *higher order branchings* (i.e. branching off the branches) clearly identifiable, occurring on sidebranches on both sides of the crystal synchronously, despite more than $500\ \mu\text{m}$ distance in between (≈ 25 tip radii).

4.5.2 Transient tip shapes in melting

The transition from melting to growth leads to the sphere-like tip and the T-type sidebranches described in section 4.1.1. Another falling temperature trend was analyzed that leads to a different tip shape evolution. The temperature drop was slowed down. Instead of letting the temperature decrease to the full undercooling T_∞ , heating was used to stabilize it at T_p for some minutes. This trend is shown in figure 3.4 (IIIb).

The result is a rather triangular shape with straight sides. A comparison with the heating pulse P-type branching and with the sphere-like shape is shown in figure 4.17. While the pulse lets dominant P-type sidebranches grow, the sphere-like transition gives rise to the typical T-type sidebranching with doublon character. The spear-like tip becomes unstable against the Mullins-Sekerka instability and sidebranches start to grow from its four fins.

The difference between spherical and triangular transition of the dendrite tip is also seen in the plot for the characteristic parameters (fig. 4.18). Compared to the T-type branching in figures 4.5(a)(b) the sharp drop does not show up, and neither does the characteristic bulge indicate the second partner of the doublon. The tip gradually becomes thinner over a lapse of about 150 seconds while the velocity increases. These two characteristics together lead to the triangular shape.

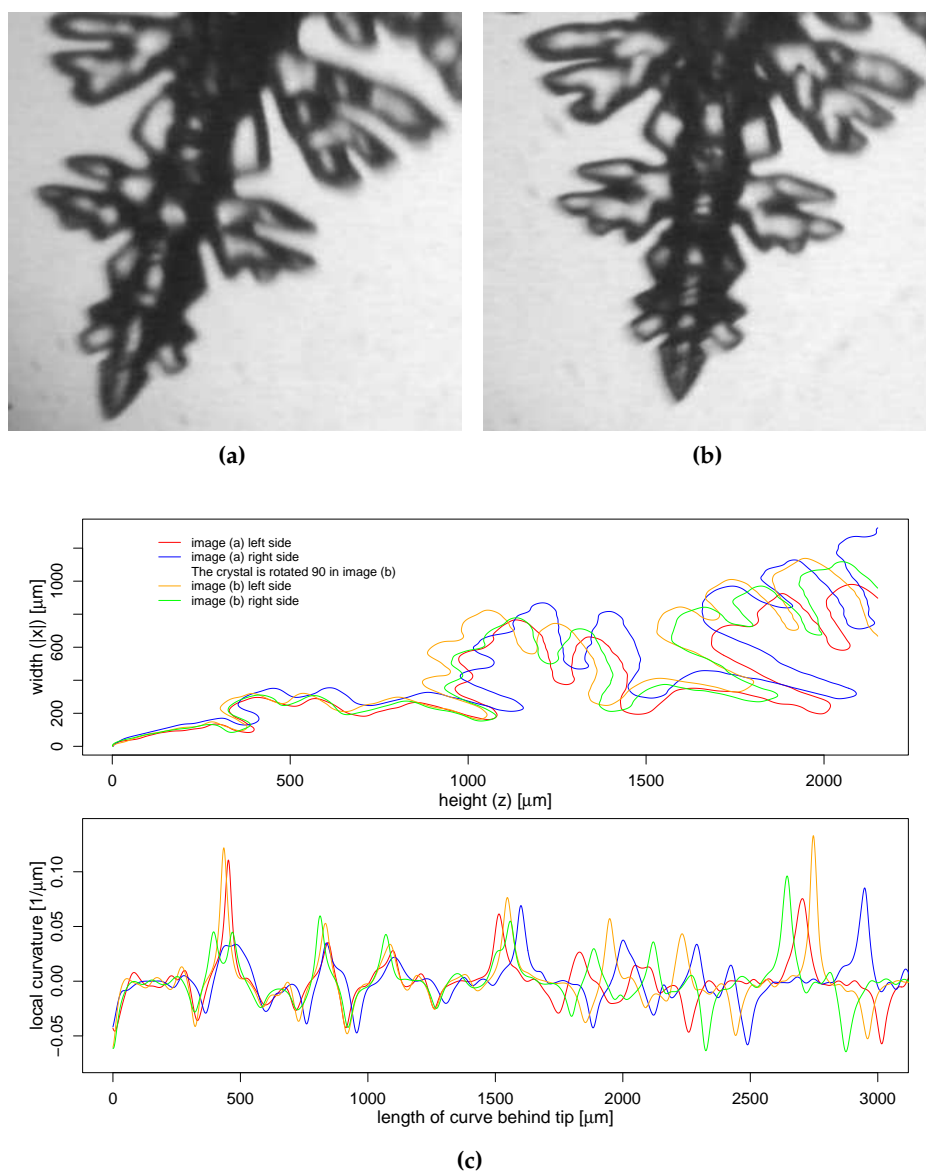


Figure 4.14: A symmetric tip viewed from two perpendicular angles. The images (a) and (b) show a symmetric shape. The four outlines are plotted in the upper panel of (c). The shapes are almost the same on all four sides, for both perspectives the right hand side, i.e. the lower part of the dendrite grows a little faster. The local curvature of the same contours, plotted against the contour length behind the tip, is shown in the lower panel of (c). The curvatures are highly correlated for the first 1.5 mm, then the asymmetric growth makes the before coincidental maxima and minima to spread out.

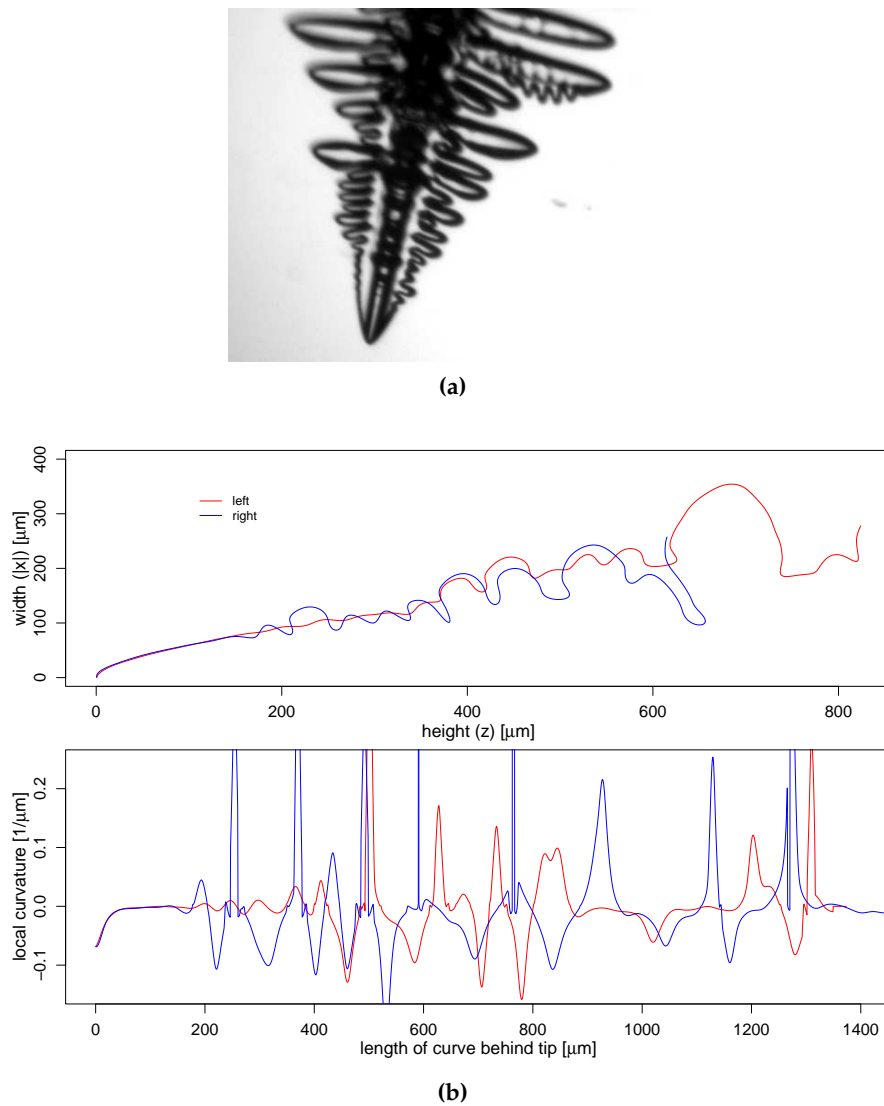


Figure 4.15: A freely grown dendritic tip in the same analysis as in figure 4.14. The dendrite looks similar on both sides (a), but neither the contours match nor does the local curvatures (b).

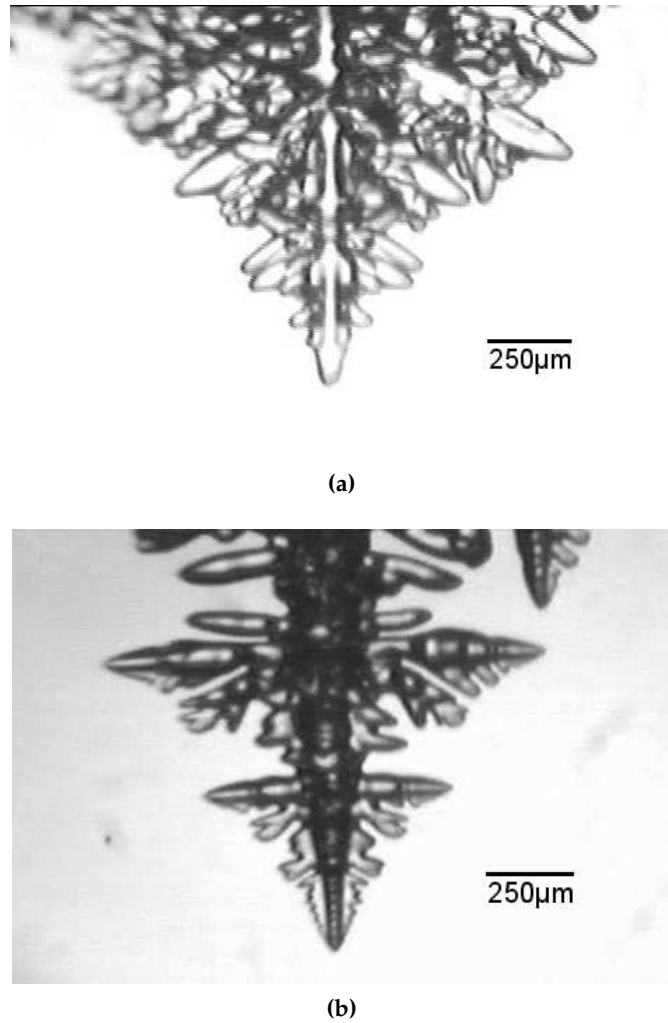


Figure 4.16: Two symmetric crystals viewed from 45°-angle (a) and in a maximum-area projection (b). The symmetric sidebranches show higher order branchings occurring simultaneously even though they are about 20 tip radii separated.

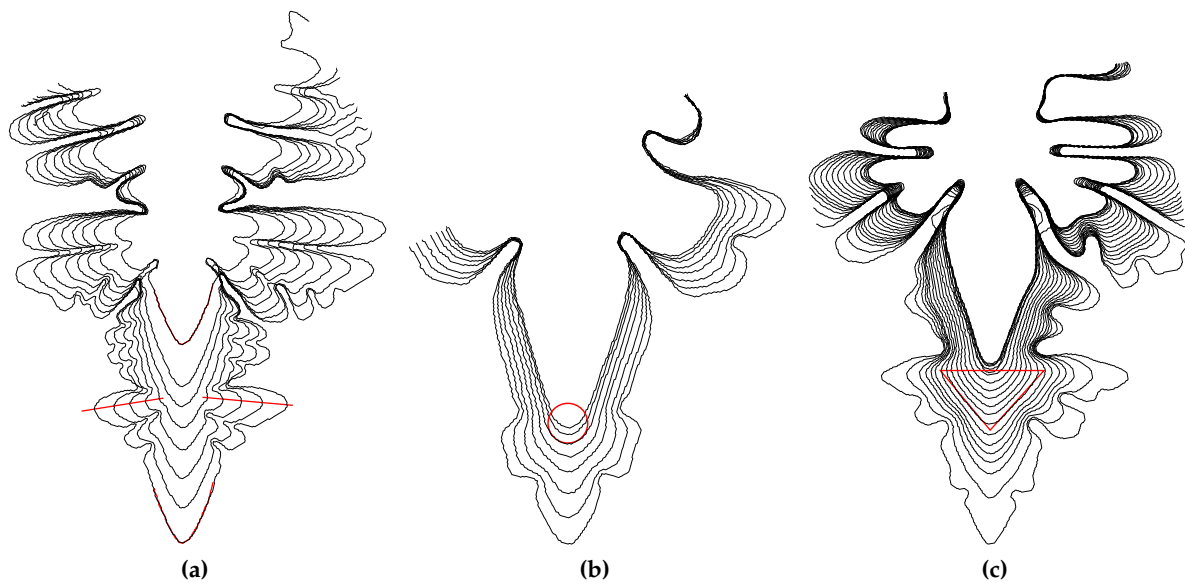


Figure 4.17: Three possibilities for tip shaping: Heat pulse, free falling temperature and slowed temperature drop lead to different tip shapes and therefore different sidebranches. **(a)** The heat pulse produces a P-type sidebranch, the tip shape remains unchanged. **(b)** A falling temperature transition results in a temporary spherical growth and to T-type sidebranches. **(c)** When the temperature drop is slowed down and stabilized at T_p , where $T_\infty < T_p < T_m$, the tip evolves to a triangular shape and the sidebranches look different, compared to the T-type sidebranches. The doublon character is missing. The contours show the crystals outlines in 50 second intervals for **(a),(b)** and 100 second intervals for **(c)**.

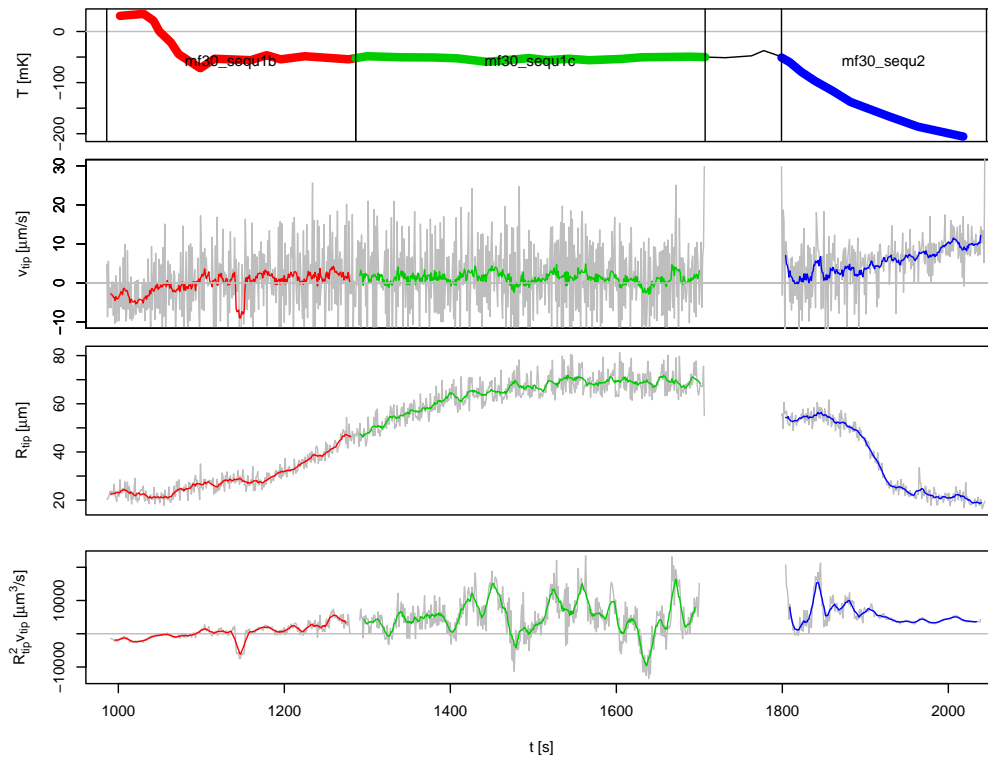


Figure 4.18: The temporal evolution of the characteristic parameters of the main tip. The temperature is stabilized at $\Delta T \approx 50$ mK for almost 700 s. The velocity is about $2 \mu\text{m/s}$ during this period and the radius grows to a stable value. Once the temperature is allowed to fall towards T_∞ , the velocity increases and the radius decreases without the sharp drop seen in figure 4.5.

4.5.3 Sidebranch initiation and coarsening

One of the characteristic features of dendritic growth patterns is the sidebranch spacing. The controlled sidebranch initiation by temperature changes, described in section 4.1.1 allows to modify this feature. A comparison between a freely grown dendrite (a) and a shaken one (b) in figure 4.19 reveals another modification of the sidebranch geometry. Both dendrites were grown at the same undercooling of $\Delta \approx 0.005$, never the less they show a difference in their sidebranch arrangement. The sidebranch growth for the free dendrite (a) obeys Brener's law for the amplitude of sidebranches [47], as confirmed by Wittwer [48]. The tip region is smooth, having the shape of a $|x|^{\frac{5}{3}}$ -curve. Sidebranches start being visible at a distance \bar{z}_{SB} of about 10 to 15 tip radii behind the tip, in accordance with reference [11]. Shortly after the formation of sidebranches, coarsening sets in and only a few dominant ones continue to grow, while their neighbors vanish.

For a shaken dendrite (b) the sidebranches start growing at the very tip. This is an indication for the perturbation induced P-type sidebranches. There is no clear distinction between dominant and vanishing sidebranches in the region up to about $1000 \mu\text{m}$. The area filling factor i.e. the solid/liquid ratio within the dendrite envelope seems to be higher than for the free dendrite.

The superposition of the two geometrically corrected contours (fig. 4.19(c)) shows that the envelope of the shaken dendrite has more a triangular shape with straight sides, whereas the envelope of the free dendrite is curved. A rough estimate of the angle of aperture of the envelopes at the tip gives about $35 \pm 5^\circ$ for the free dendrite and about $70 \pm 5^\circ$ for the shaken one in the lower about $1000 \mu\text{m}$. The sidebranch amplitudes of the shaken crystal are in fact bigger than the ones of free dendrites. The dominant sidebranches of the free dendrite – that could 'free itself from its surrounding' – surpass the shaken ones and have bigger amplitudes from about $1200 \mu\text{m}$ behind the tip. The temporal evolution of sidebranches is shown in (d), (e). On the shaken dendrite (e), the sidebranch spacing λ is wider, they start earlier and the coarsening process is less effective than on the free dendrite (d). Up to a height of $1000 \mu\text{m}$, the variance of the sidebranch amplitude is smaller than for free growth.

4.5.4 Area

Figure 4.19(e) brings us back to the idea of a volume filling factor discussed in [13]. The projection area of the shaken dendrite resembles a triangle. A simple model for the area A of such a triangle leads to

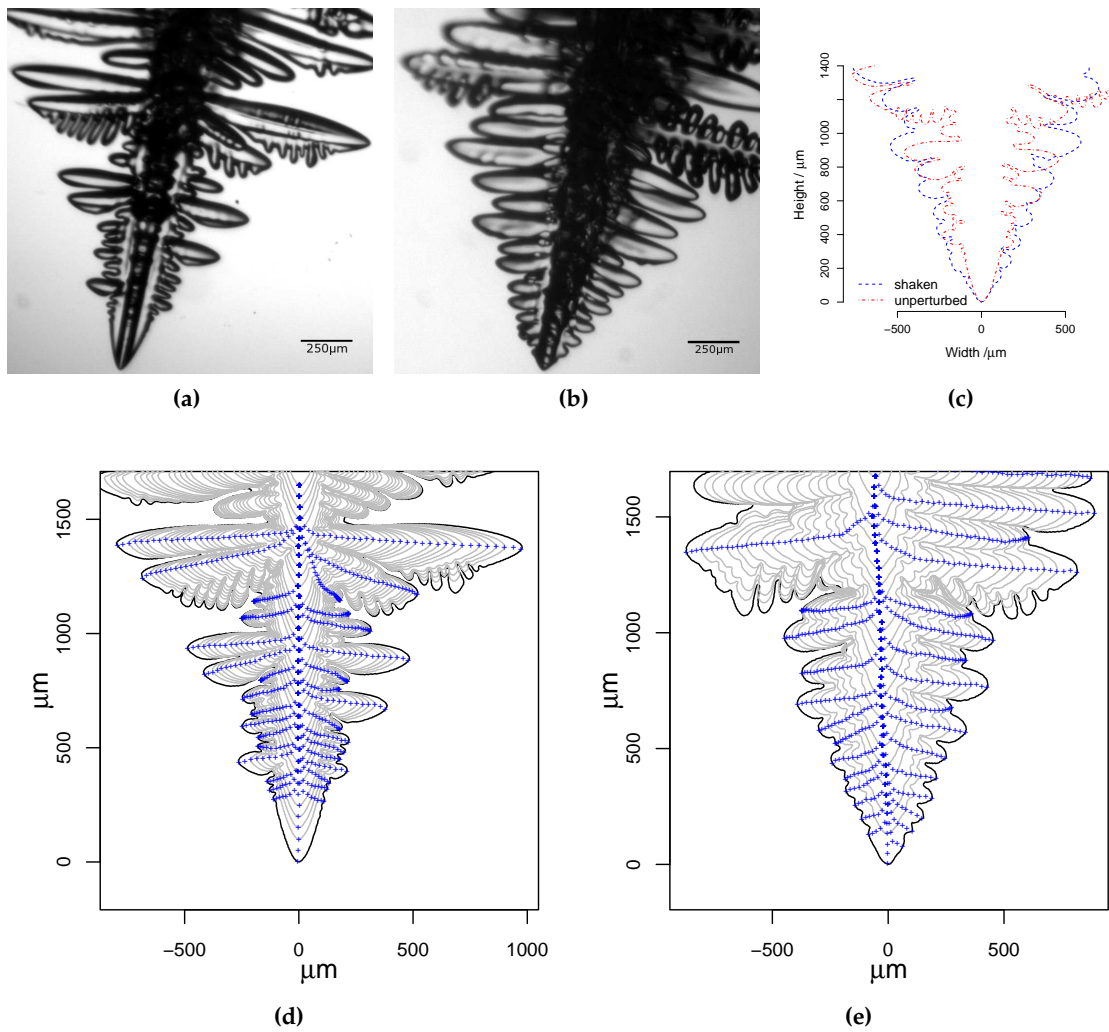


Figure 4.19: A comparison between a freely grown (a) and a shaken (b) dendrite. The shaken one is identified by eye to be the thicker one. The plot of the geometrically corrected contours (c) proves that this is not because of different projection angles. The sidebranches are tracked in (d) and (e) and show a larger spacing and a less effective coarsening for the shaken dendrite (e).

$$h = v_{tip} \cdot t \quad (4.1)$$

$$w \approx 2 \cdot v_{SB} \cdot t$$

$$\sim 2 \cdot \frac{v_{tip}}{2} \cdot t = v_{tip} \cdot t = h$$

$$A \sim \frac{h \cdot w}{2}$$

$$\sim 0.5 \cdot h^2, \quad (4.2)$$

where h is the height along the z -axis, w is the width along the x -axis, v_{tip} the main tip velocity and v_{SB} the sidebranch tip velocity. The ratio of the two velocities was found to be $v_{SB}/v_{tip} \sim 0.5$ [74].

The measured area as a function of h^2 is seen in figure 4.20 for various dendrites. The prefactor is a measure for the area filling factor

$$A = \beta \cdot h^2.$$

The prefactor β for 11 sequences from 9 different freely grown crystals (open circles in the plot) is $\beta = 0.210 \pm 0.035$, while the same prefactor for 8 sequences from 3 different shaken crystals (filled circles) is significantly larger, $\beta = 0.365 \pm 0.020$. Different frequencies of perturbation have been applied: 1/40, 1/10 and 2 Hz and the range of undercooling is $100 \text{ mK} \lesssim \Delta T \lesssim 250 \text{ mK}$. No significant influence has been found. Compared to the model of a filled triangle, about 40% of the area is solidified in free growth, whereas the shaken dendrites fill the triangle to more than 70%.

Coming back to the volume according to the simple model, the volume is proportional to the thickness of the triangle and thus proportional to the radius of curvature R as found from volume measurements in reference [13], figure 15. The independence of the area filling factor on the undercooling is consistent with this idea.

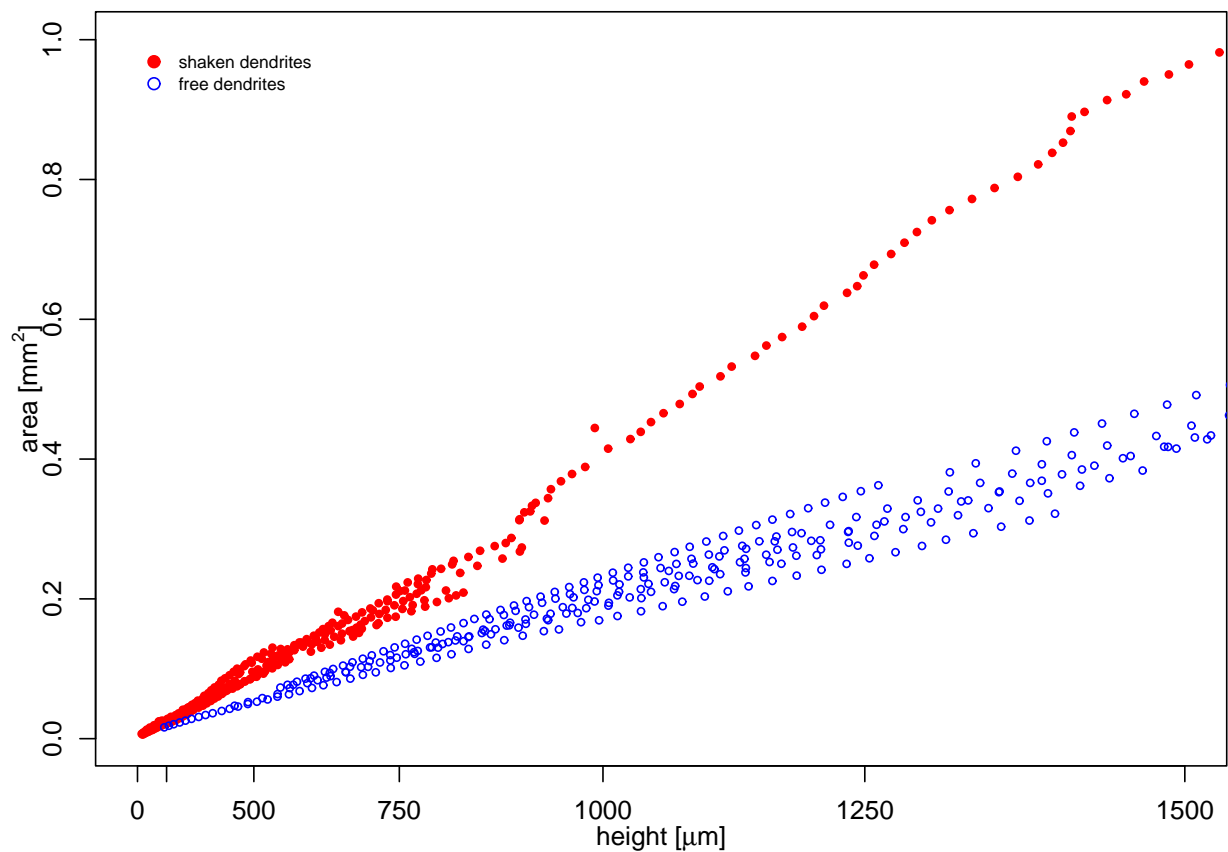


Figure 4.20: The area of the projection of a dendrite as function of the height. The values on the abscissa indicate the true height h of the dendrites. They are plotted squared to see the filling factor β from $A = \beta \cdot h^2$ as the slope. The area for the three shaken crystals (filled circles) grows faster with increasing height (i.e. the filling factor β is larger) than it does for free growth (open circles) of nine crystals. The undercoolings are between 100 mK and 250 mK for both the free and the shaken crystals. No significant influence of the undercooling is found.

Chapter 5

Simulations

5.1 Setup

For a qualitative analysis of the thermal fields in the growth vessel, simulations over the complete domain were performed. The size of about $5 \times 5 \times 5$ cm prevented using microscopic modeling for computational reasons. It was supposed that for qualitatively reasonable results it is sufficient to solve the classical fluid dynamics equations using a finite element method. The coupled differential equations for heat and flow were solved in two and in three dimensions on a fixed mesh according to table 5.1. The solver was ELMER¹, provided as open source software by CSC, the Finnish IT center for science².

The mesh was not adapted in order to simulate the growth and the phase transition was not modeled since this was out of the scope. Instead, the surface was kept at the melting temperature T_m .

The mesh was generated automatically to be denser near thin structures like the crystal and wider near the shell of the vessel. Two meshes with a different lower limit for the element size (both much smaller than the capillary diameter) were compared in the three-dimensional calculation and showed no significant differences on the results. Therefore the coarser mesh

¹<http://www.csc.fi/elmer/>

²<http://www.csc.fi/suomi/info/index.phtml.en>

domain	# nodes	# elements
2D	2547	4874
3D	33334	176580
3D high res.	74780	405546

Table 5.1: The mesh sizes for the finite element simulations in two and three dimensions. No significant differences have been found using either of the two three-dimensional domains. The repeated heating cycles were solved on the '3D' domain in order to save time.

with about 176 000 elements was used for all calculations, mainly the repeated heating would have taken too much time otherwise. The boundaries of the used mesh is shown in figure 5.1. The crystal has a tilt angle ($\sim 20^\circ$) against the vertical. The symmetry is broken thus the whole domain has to be solved.

5.2 Diffusive temperature field

For a comparison of the approximate diffusion fields in the growth vessel in both two and three dimensions with the result under consideration of the convective flow, the diffusion equation has been solved. No qualitative differences in the shape of the diffusive field can be found numerically for the three different undercoolings ΔT of 50, 200 and 400 mK, covering the range of the experiments. A rough estimation of the extension shows a large diffusion field compared

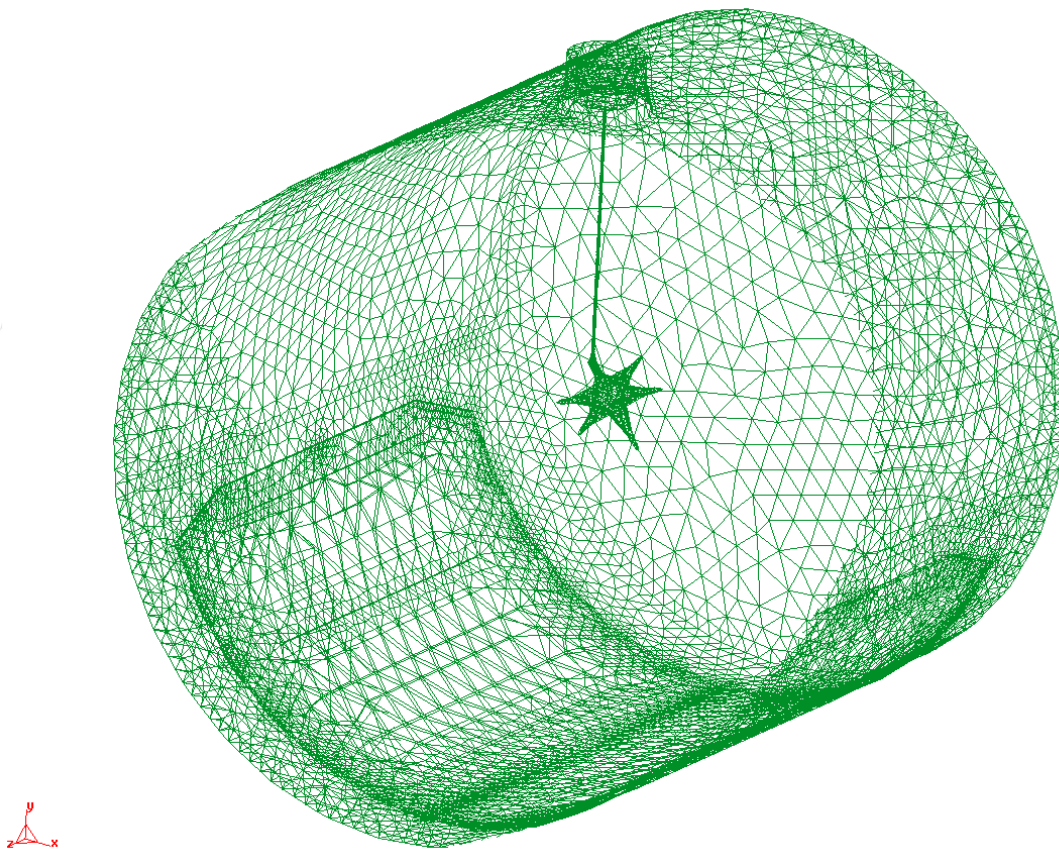


Figure 5.1: The boundary elements of the mesh used in three dimensions. The cell sizes vary according to the structures. One part was cut away in this representation for a better view inside the vessel.

to the crystal structures. The diffusion length l and the Péclet number p are

$$l = \frac{2D}{v} \approx \frac{2D}{5 \cdot 10^{-6} \text{ m/s}} \approx 3 \cdot 10^{-2} \text{ m} \quad (5.1)$$

and

$$p = \frac{R}{l} \approx \frac{20 \cdot 10^{-6} \text{ m}}{l} \approx 7 \cdot 10^{-4} \text{ m}. \quad (5.2)$$

The diffusion length l has no meaning in the region of the dendrite tip though, because it is defined ahead of a plane surface. Therefore the undercooling at a point close to the dendrite tip, e.g. 0.3 mm ahead of the tip pointing downwards (*the 0.3 mm point*) is given in table 5.3.

5.3 Convective flow

In earth-bound growth experiments, a buoyancy force shows up due to the temperature dependency of the density of the melt. This force drives a convective flow. It has been an open question, how strong this flow is in the growth vessel.

5.3.1 Experimental observation

Experimentally it was possible in some seldom cases to observe single dust particles in the liquid xenon in the focus plane. They were about $5 - 10 \mu\text{m}$ in diameter and the maximum velocity in one sequence was measured to be in the order of magnitude of 0.7 mm/s. In a second sequence, Wittwer [63] found a particle moving in the liquid upwards with a maximum velocity of about 0.5 mm/s. This gives an order of magnitude of the convective velocity in the experiment.

5.3.2 Simulation in 2D

The results on a two-dimensional domain can provide at least a qualitative idea on the process in the growth vessel. It is found that for the typical situation of a (quite large, actually) crystal, 20° rotated against the vertical, there are two convective rolls formed in the upper part of the vessel (fig. 5.3). There is no prominent convective flow channel upwards except at the top of the crystal along the capillary. The capillary itself was not modeled in 2D to prevent a separation of the domain. Compared with the pure diffusive case the temperature field is shifted to the top and the gradient around the lowest of the four tips (*the tip*) is larger. The convective flow compresses the isotherms.

The mean velocity at the 0.3 mm point as well as the temperature at the same position were calculated for different setups, the crystal was located in the upper, middle or lower part of the vessel, inclined or symmetric relative to the plumb line. The results in table 5.2 show that for the larger crystal in the middle position the flow is a little higher, especially in the asymmetric case.

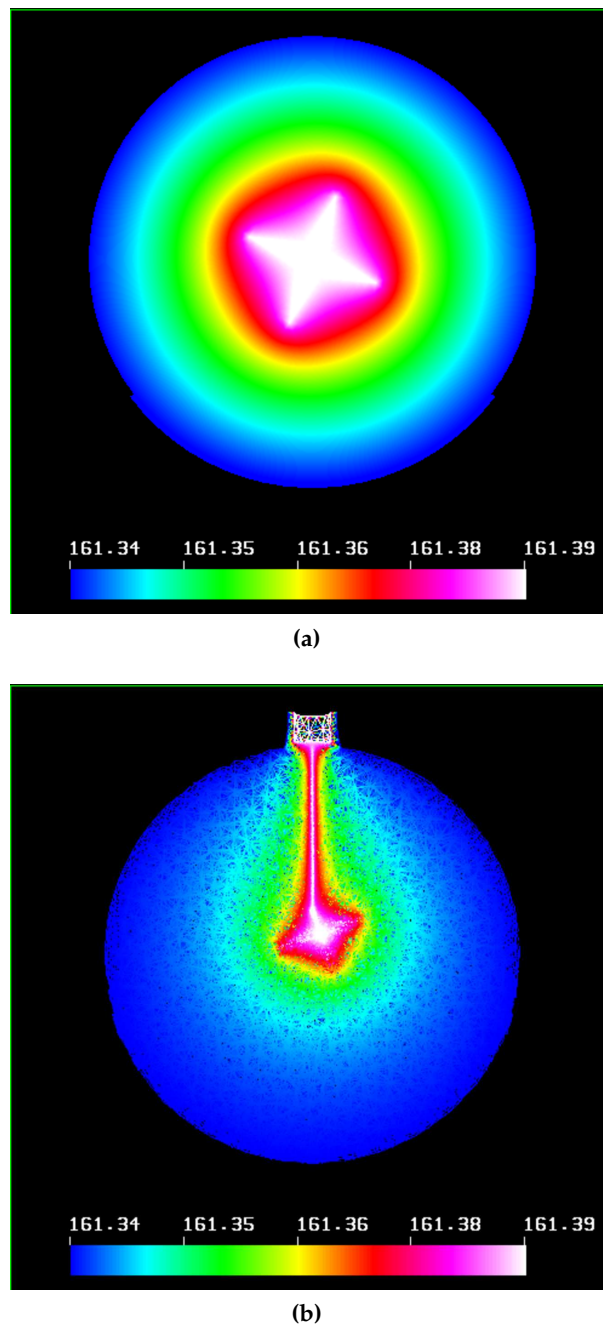


Figure 5.2: The solution for the temperature fields without any convection (a) in two and (b) in three dimensions (for a given undercooling of $\Delta T = 50\text{mK}$). The diffusion fields are large compared to the crystal.

For the symmetric growth as well as for the different vertical crystal positions in the vessel, the velocity of the convective flow correlates with the undercooling. The higher the undercooling ΔT the higher the convective velocity.

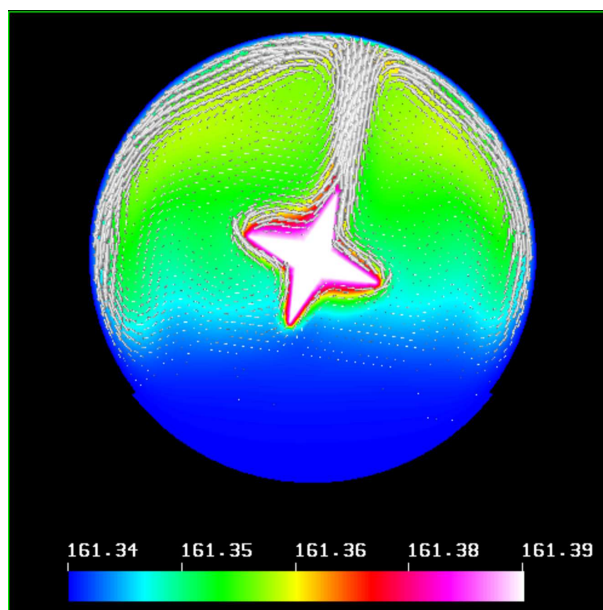


Figure 5.3: The temperature and velocity fields in the 2D growth vessel in steady-state, with the crystal tilted 20° in the middle. The undercooling at the outer boundary is $\Delta T = 50\text{mK}$, the temperature on the crystal surface is $T_m = 161.3987\text{K}$.

5.3.3 Simulation in 3D

The Laplace operator differs in three dimensions from the two-dimensional one, which leads to the well known fact, the diffusive field in 2D and in 3D have different decay rates (see fig. 5.2). The results in 3D therefore can be expected to look different from the 2D solutions.

In figure 5.4 is clearly shown, that the convective flow in large parts of the growth vessel is much less pronounced than it is in 2D. The strong upward flow around the capillary (which is of comparable magnitude) in the three-dimensional case spreads over all directions once it has reached the top of the growth vessel. Therefore the downward flow speed is significantly reduced. Only near the crystal tip the strong upward flow causes a higher velocity of the melt in 3D than in 2D. This is shown in the last line of table 5.2. Both figures 5.3,5.4 show a decreasing temperature from the upper to the lower part of the growth vessel. However this gradient is small compared to the one at the interface.

As in the two-dimensional case the isotherms are compressed by the convective flow in such way that the gradient around the crystal is larger than in the two-dimensional layout. The temperature at the 0.3mm point is noticeably lower as can be seen again in table 5.2.

The influence of the convective flow in either dimension can be seen clearly in the temperature at the 0.3mm point as listed in table 5.3. The temperature of the purely diffusive field alone is lower in 3D than in 2D, and this difference grows with undercooling. With convective flow the temperature is again lower than without and the difference to the convection-free case of the same dimension increases with increasing undercooling.

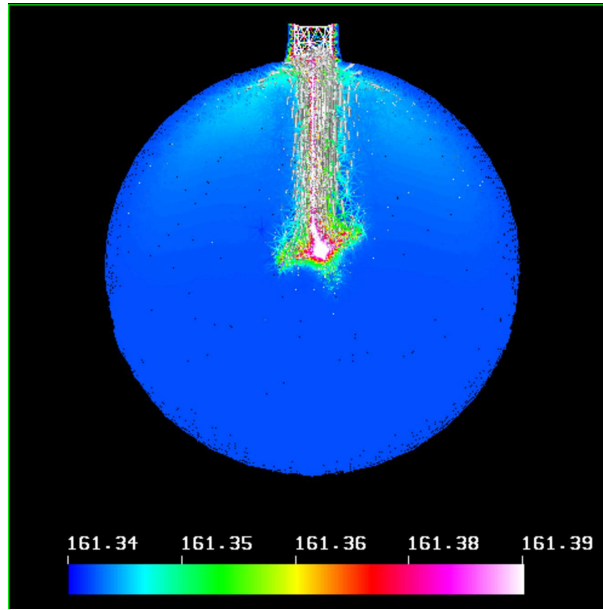


Figure 5.4: The temperature and velocity fields in the 3D growth vessel in steady state. The undercooling at the outer boundary is $\Delta T = 50\text{mK}$, the temperature on the crystal surface is $T_m = 161.3987\text{K}$. The crystal orientation is the same as in figure 5.1.

		ΔT		50 mK		~ 200 mK		~ 400 mK	
		T_∞		161.3400 K		161.2000 K		161.0000 K	
position	tilt angle	V_{abs}	T	V_{abs}	T	V_{abs}	T	V_{abs}	T
bottom	0°	91	161.3747	181	161.3338	242	161.2743		
	20°	97	161.3749	192	161.3345	256	161.2761		
middle	0°	104	161.3725	201	161.3254	265	161.2578		
	20°	138	161.3682	287	161.3095	395	161.2254		
top	0°	88	161.3752	171	161.3355	229	161.2784		
	20°	86	161.3751	179	161.3355	243	161.2782		
middle (3D)	$20^\circ / 20^\circ$	159	161.3652	306	161.2956	449	161.1970		

Table 5.2: The calculated values for the absolute velocity V_{abs} in $\mu\text{m/s}$ and the temperature T in K in two and three dimensions at a point 0.3 mm ahead of the tip.

5.4 Heating and cooling

Within this computational framework a complete heating cycle was calculated. The heater was switched on for $t_{on} = 45\text{s}$ and heating was interrupted for another $t_{int} = 15\text{s}$ as in the experiments. The formation of complex flow patterns was observed. A snapshot of the situation after the last heating pulse can be seen in figure 5.5. The flow around the crystal was found to

ΔT		50 mK	200 mK	400 mK
T_∞		161.3400 K	161.2000 K	161.0000 K
position	tilt angle	T	T	T
purely diffusive				
middle	20°	161.3850	161.3719	161.3531
middle (3D)	20° / 20°	161.3782	161.3457	161.2994
with convection (same as table 5.2)				
middle	20°	161.3682	161.3095	161.2254
middle (3D)	20° / 20°	161.3652	161.2956	161.1970

Table 5.3: The calculated values for the temperature T in K in two and three dimensions at a point 0.3 mm ahead of the tip. Both cases (diffusion-only and with convective flow) are shown. The actual undercooling is shielded in both cases, 2D and 3D, by the diffusion field. With the convective flow enabled, the gradient is more sensible to ΔT and the temperature reaches about $\Delta T/2$ at this point in 3D.

change within seconds. The resulting temporal evolution of the temperatures at four different positions in the vessel are shown in figure 5.6(a) for two dimensions and in figure 5.6(b) for the three-dimensional environment. The positions correspond to the real positions of the crystal tip, the 0.3 mm point, and the two Pt-100 in the growth vessel respectively. Compared with the experimental data, a good qualitative agreement can be found. The absolute values in three dimensions are too small though. Two effects could explain this discrepancy:

- (1) The finite thickness of the glass hull of the vessel was neglected. Instead the glass wall was considered as an infinitely thin boundary between the xenon and the outer medium (fixed to T_∞ , except where it is in contact with the heater of course). The heat can leave the vessel faster than in reality due to the missing heat capacity of the glass shell. Although this does not matter for a steady-state, it is important for transient phases. The heat flow from the heater into the vessel was calculated using an estimation for the transfer coefficient.
- (2) The surrounding heat bath has not been taken into account. About one half of the heater's power is absorbed in the heat bath. This 'warm' liquid flows around the growth vessel to the top and reduces the heat flow out of the vessel.

The implication of these simplifications is that the calculated temperature in the growth vessel in 3D is too low and does not exceed the melting temperature after 10 heating pulses.

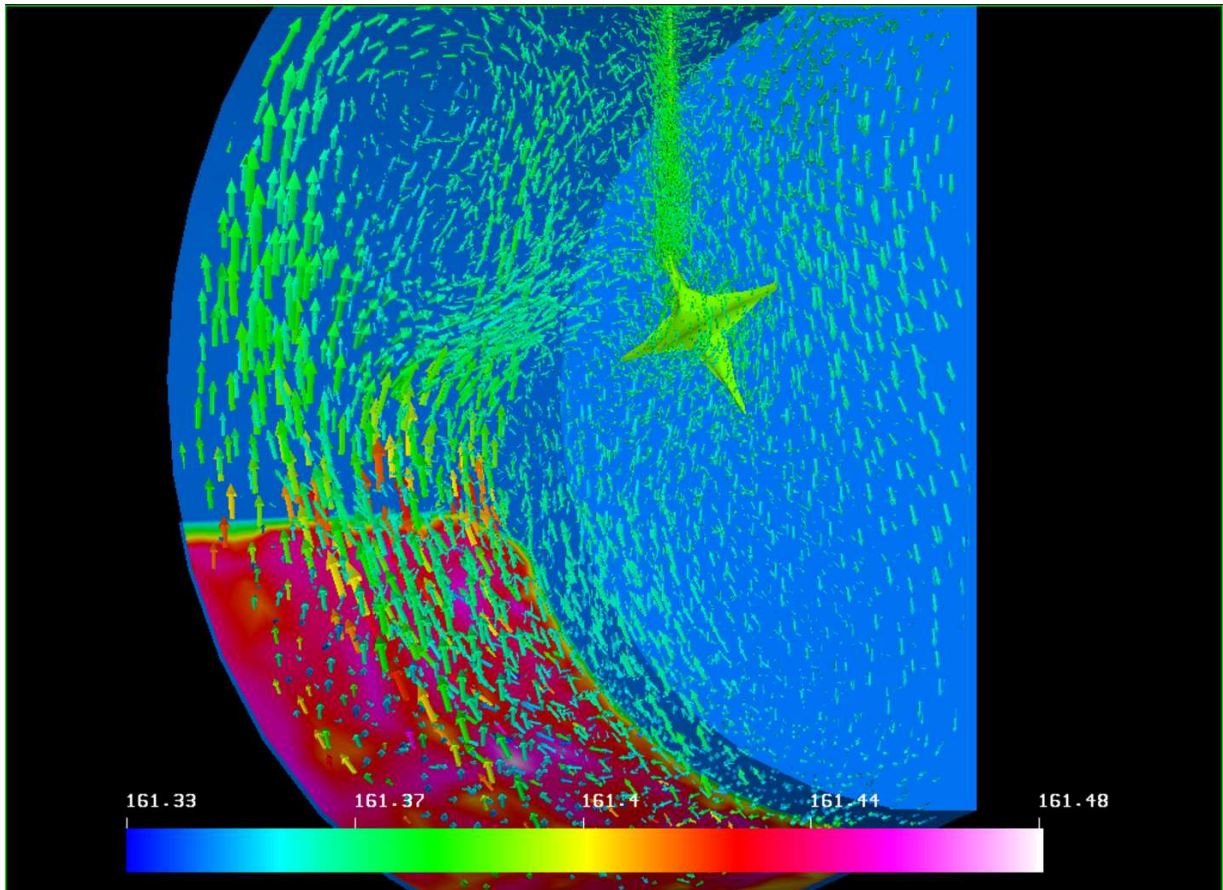
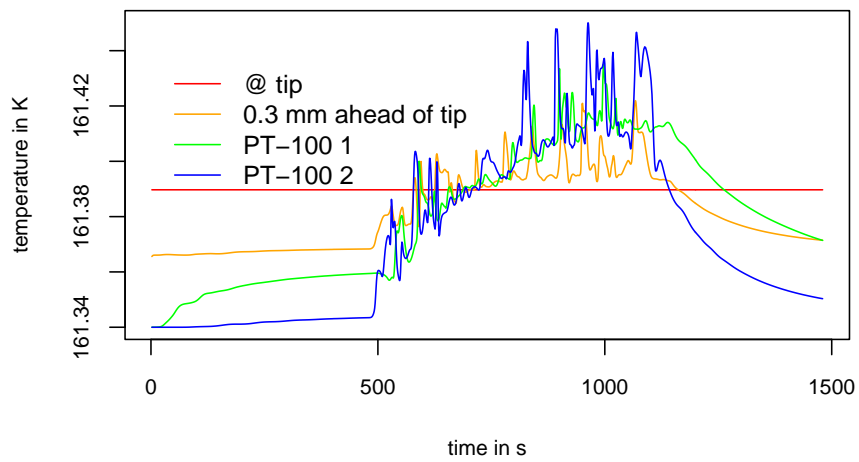
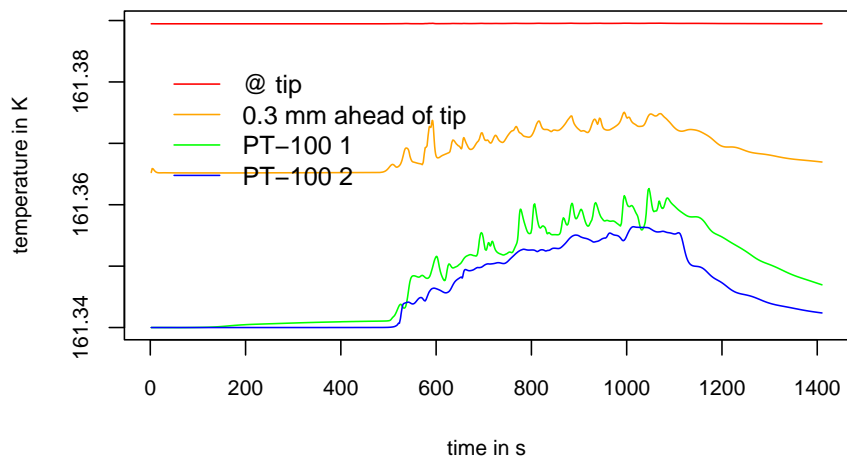


Figure 5.5: The flow and temperature in the growth vessel around the crystal after the 10th heating pulse. The length of the arrows show the absolute velocity, the colors show the temperature. The crystal is found to be in a flow of xenon at about the melting temperature (same color as the crystal) from various directions.



(a) 2D



(b) 3D

Figure 5.6: The temperatures as calculated on four different points in the growth vessel.

Chapter 6

Discussion

The results found during the two series of perturbation experiments presented in chapter 4 can be ordered with respect to the perturbation strength. (i) Starting from the free dendritic growth with non-vanishing anisotropy, thermal fluctuations are the smallest perturbations. They are considered to be the reason for noise induced sidebranching in Langer's and Brener's theories which have been confirmed in experiments. Spontaneous appearances of multi-tip-configurations are found but they are transient. (ii) The next larger perturbation in the experimental framework presented here is shaking with small amplitudes. The motion of the oscillating tip is of the order of 1 mm/s over a distance of about 10 μm . Under the influence of this force early sidebranching is observed, coarsening is reduced and multi-tip configurations are stabilized. (iii) The heating pulse is a stronger perturbation again, the temperature around the crystal is changed within seconds, sidebranching is selectively initiated. The transient temperature drop acts the other way round, within seconds the temperature around the tip decreases. This leads to sidebranching too, but with different shapes. It is noteworthy that no transition to multiplons can be provoked this way, in accordance to Dougherty's observations [26]. (iv) Finally the melting obviously as strongest impact on 'growth' leads to smooth structures as reproducible starting points for the falling temperature transitions. The shape of the whole crystal is affected by melting. In this work, the melting process has not been in the focus of research. Rather melting has been used as an instrument providing reproducible initial conditions for the transition to growth.

The systematic application of perturbations leads to a reproducible formation of characteristic structures on a dendrite, defining its shape and characteristic parameters such as sidebranch spacing and area filling factor. The question arises, which selection mechanism for these shapes is hidden behind perturbations (ii) and (iii). Is the steady growth with a unique selection parameter $\sigma \approx \sigma^*$ only one of many possible states that can be forced by the perturbations? This possibility has been discussed by Langer [7] in a different form, when he asked for the ways the *wavelength* selection for the perturbation analysis may occur, focused on the stability analysis of the dendritic single tip. Can the perturbations be viewed as a controlling mechanism in a system with (i) one attractor the marginally stable growth, (ii) another attractor a limit cycle centered in this point, (iii) a further one, far away in the phase-space, the dendritic doublons?

6.1 Mechanism for tip splittings

The so-called tip splittings in the dendritic growth lead from a single dendrite to dendritic doublons, triplons or quadruplons in a single step. Further splittings of the newly-born tips result in higher order multi-tip-configurations. In the f.c.c. structure of xenon, the showing-up of a split to three is not a priori easy to understand. The proposed mechanism for the tip splittings bases on the fact that free dendrites look like a rotational symmetric needle-crystal in the foremost part. The fins becomes visible and the trunk evolves at a distance of about 3 tip radii from the tip, the sidebranches grow on the fins, starting about 15 tip radii behind the tip. This shape is clearly seen in figure 6.1.

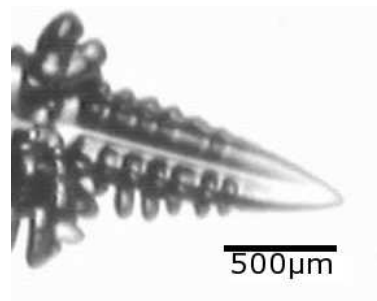


Figure 6.1: The shape of a dendrite near the tip is clearly seen in this orientation. The tip is rotationally symmetric, the fins start about 3 tip radii behind and the sidebranches start growing on the fins about 15 tip radii behind the tip.

As a reaction to a perturbation, the tip velocity decreases but the fins do not keep the distance to the tip, rather they 'catch-up' with the main tip. In the usual maximum-area projection and outline investigation the tip becomes slower and thicker. These fins can even surpass the former 'main' tip and evolve in four lobes. These structures then grow into new tips. An image sequence of the transition towards a doublon is shown in figure 6.2. A comparison with the tip-splitting mechanism in (quasi-)two dimensions is shown in the contours in Fig. 6.3.

The same process can lead to quadruplons. In this case, all four fins surpass the main tip and four new tips are formed (see fig. 6.4(a)). The triplon is a degenerated quadruplon, where one of the four fins (surrounded by warmer melt due to convective flow) is a little slower and can not evolve in a new tip. This is shown in figure 6.4(b). After some minutes of growth, this process can repeat on one of the new tips, leading to the odd multi-tip-configurations observed by Wittwer [63].

This mechanism is presumably different from how the tip splitting happens in directional solidification in quasi-two dimensions, where in fact a 'splitting' is observed (e.g. in ref. [69]). Still it seems the same process of 'splitting' into two, three and four new tips observed in three-dimensional directional solidification experiments (e.g in [75,76]).

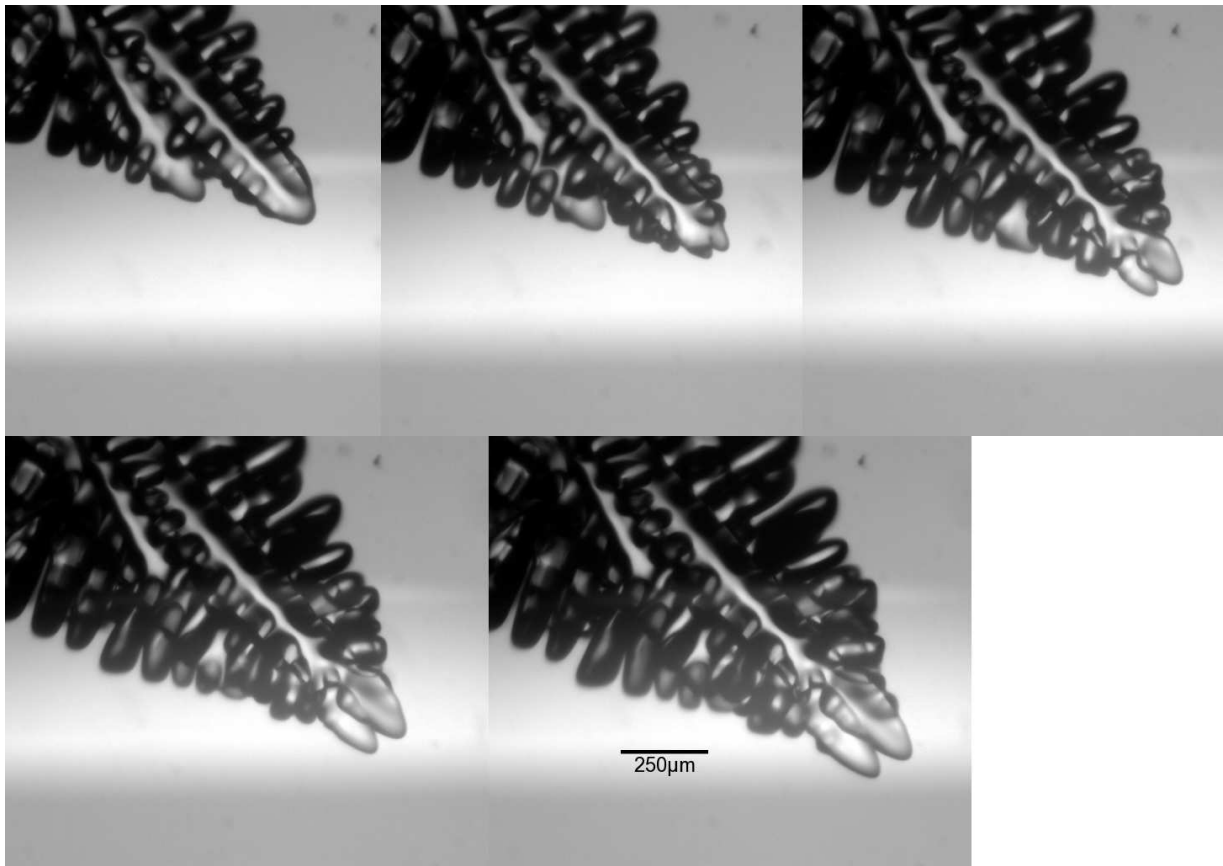


Figure 6.2: The single-tip dendrite transforms into a doublon at the fins surpassing the main tip as is seen in the temporal evolution covering 482 seconds. The fins 'catch-up' with the main tip and surpass it, evolving into two new tips. These continue to grow parallel and define a doublon. (These images have already been shown in [68].)

6.2 Stabilized sidebranching

The shaking perturbations (ii) are thought to act on the diffusive field around the tip as shown in figure 6.5(a). The *compression* of the isotherms around the crystal along the oscillation direction causes a steeper temperature gradient to the luff side at the fins in or close to the oscillation plane. A faster growth of the sidebranches on both sides of the main tip is the result, especially in the lower region of the crystal (up to about 50 tip radii). All the sidebranches in this region grow with almost the same velocity. Starting from the very tip they build a front where none of them can escape from. Coarsening is suppressed as direct consequence. The steeper gradient makes them grow faster than the unperturbed ones observed in free growth. The fins perpendicular to the oscillation plane are shifted in the diffusion field, the isotherms are compressed in the oscillation direction, making the gradient steeper. A schematic representation is shown in figure 6.5(b). A rough estimation for the mean diffusion distance (see section 6.4) in 1/100s gives $\sqrt{\langle x^2 \rangle} \approx 30 \mu\text{m}$, in the order of the amplitude. The temperature field outside this horizon is hardly affected.

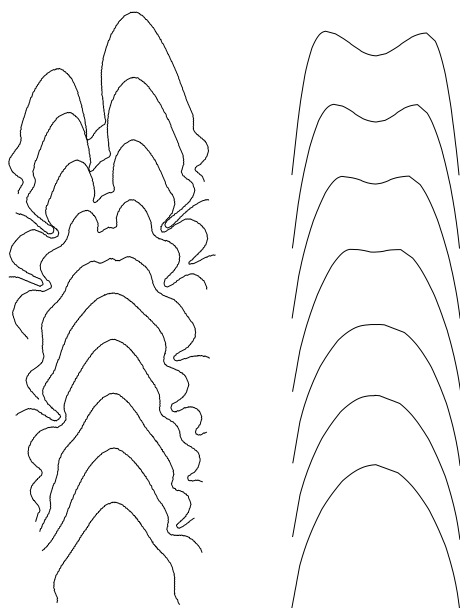


Figure 6.3: (left) The projection of the tip-splitting in three dimensions. The fins catch-up with the main tip and surpass it, then evolve into new tips. (right) The tip-splitting in two and quasi-two dimensions. The tip grows large and becomes unstable.

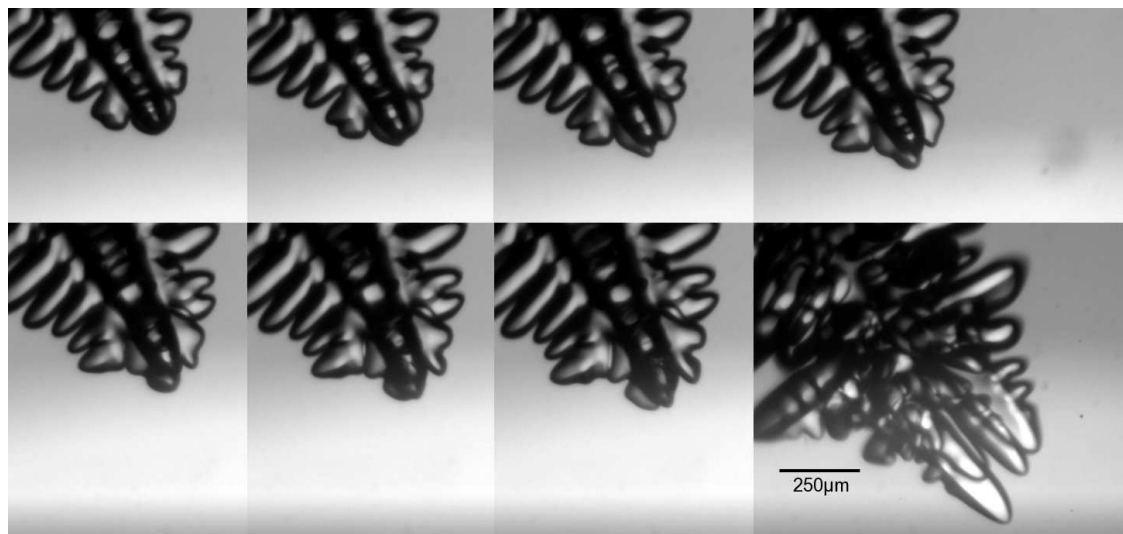
The situation on the other 'leeward' side (depicted as stretched isotherms in figure 6.5) is more difficult. An important feature is a density change (number density of atoms) in the melt in the close vicinity of the former solid-liquid interface, caused by moving the crystal rapidly out of this region. In a phase-field model, Conti [73] studied the influence of density change upon solidification. He found a decrease of the tip velocity with increasing solid to liquid ratio. But for the fast movements during shaking the situation is not really an advection flow since the volume set in motion is much larger than in Conti's steady-state solidification analysis.

On the other hand, the oscillation amplitude is too small to cause a large scale streaming around the crystal as it has been investigated by Tatsuno [77].

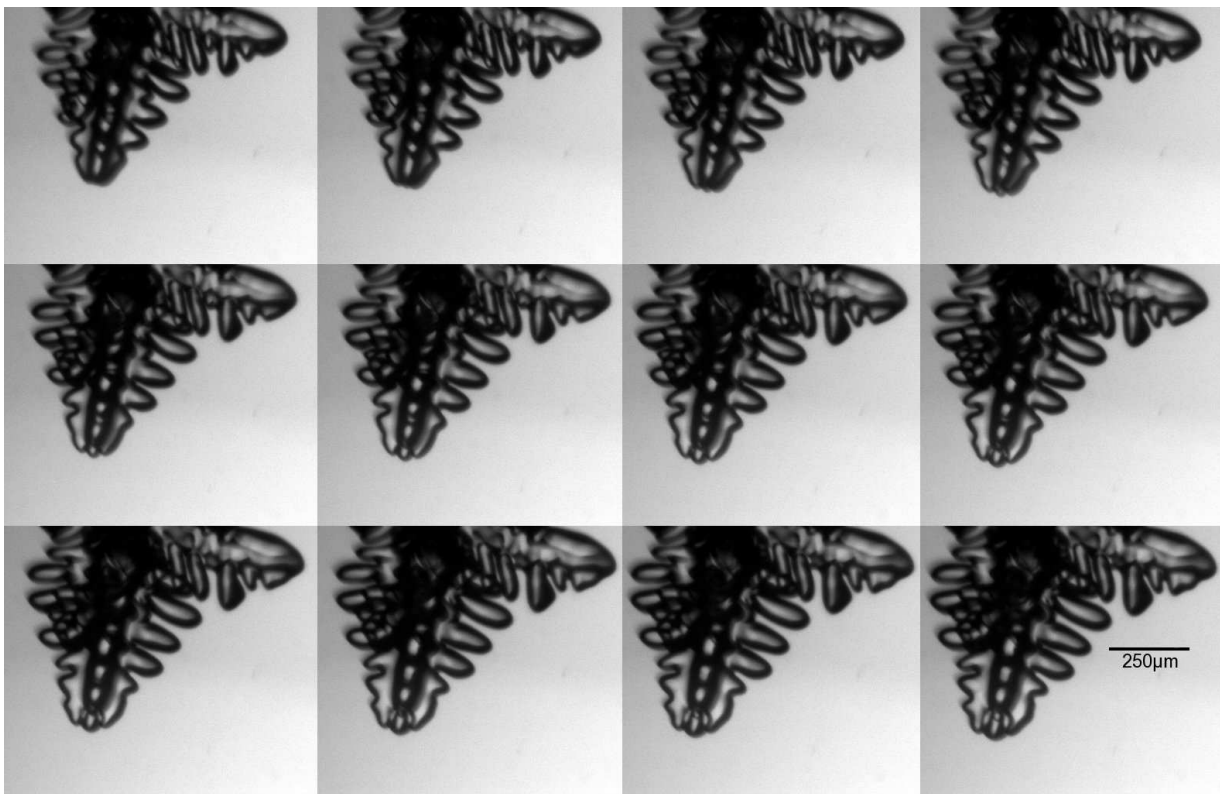
The liquid xenon flows towards the former location of the crystal and compresses the isotherms that way, causing faster growth. Thus there is an increased growth rate at the luff as well as at the lee side. This mechanism however should be examined in more detail in numerical simulations.

6.3 Unstable growth

An important indication that there are more states of growth for a dendritic tip than the needle-crystal and dendritic doublons in the sense of Ihle and Akamatsu [78,32], comes from the side-branching following a melting-growing transition. With intense heating, homogeneous initial conditions for the restarting growth are set. The highly symmetrical growth lasts for several minutes until random fluctuations (that certainly always have some effect) have been amplified



(a)



(b)

Figure 6.4: (a) The transition from a single tip to a four-fold tip, called quadruplon. The images are taken in an interval of 10 seconds. (b) A single tip transforms into a three-fold tip, called triplon. One of the fins in or out of the image plane does not evolve into a new tip. The images are in 6 seconds interval.

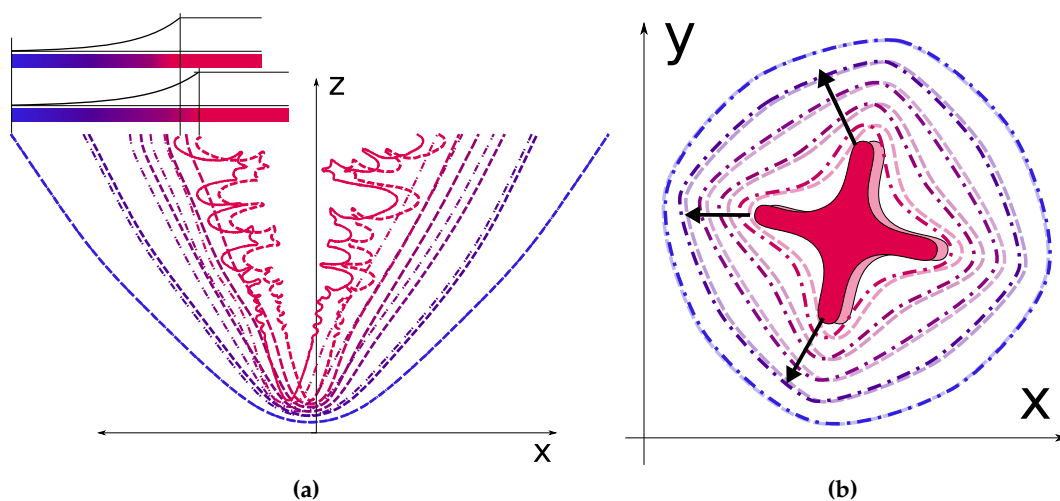


Figure 6.5: Shaking compresses the isotherms spacing in the shaking direction (parallel to the $-x$ -axis in this representation). This results in a steeper gradient in the compression direction. The stretch of the isotherms in the other direction shows only the qualitative purely diffusive temperature field. It is thought that the density drop by moving the crystal causes a flow towards the new position and therefore compresses this isotherms too.

at the unstable interface and govern the structure formation in free growth. Repetitive heating minimizes this influence.

A sequence of tip splittings and regular sidebranching is observed (4.3). This finding is a strong indicator for a meta-stable oscillatory growth mode as proposed by Holzmann [56] and by Langer and Müller-Krumbhaar [57]. The thermal fluctuations that have been found to be too small for the observed sidebranch amplitudes [45, 14] might be strong enough to drive the system out of a fix point in the basin of attraction of a limit cycle. In this framework, the experimentally [79, 80] and numerically [81] observed, randomly showing-up sequences of 3-12 sidebranches starting synchronously and with unique spacing, so called *bursts*, could be explained as transient limit cycle behavior of the system. Periodic perturbations as they have been applied in this work seem to extend the time the tip region remains in this mode.

6.4 Heat transfer as coupling mechanism

The emergence of symmetry in spatially separated regions of the crystal observed in restarted growth might have a similar background. The growth mode for *all* tips (the main tip as well as the dominant sidebranch tips) during the transition from melting to growth becomes unstable and changes more or less synchronously towards a more stable mode (the operating point of marginal stability for example). The effect of this synchronous change is clearly seen in figure 6.6, where four sidebranches show identical structures even if they are about 1 mm apart.

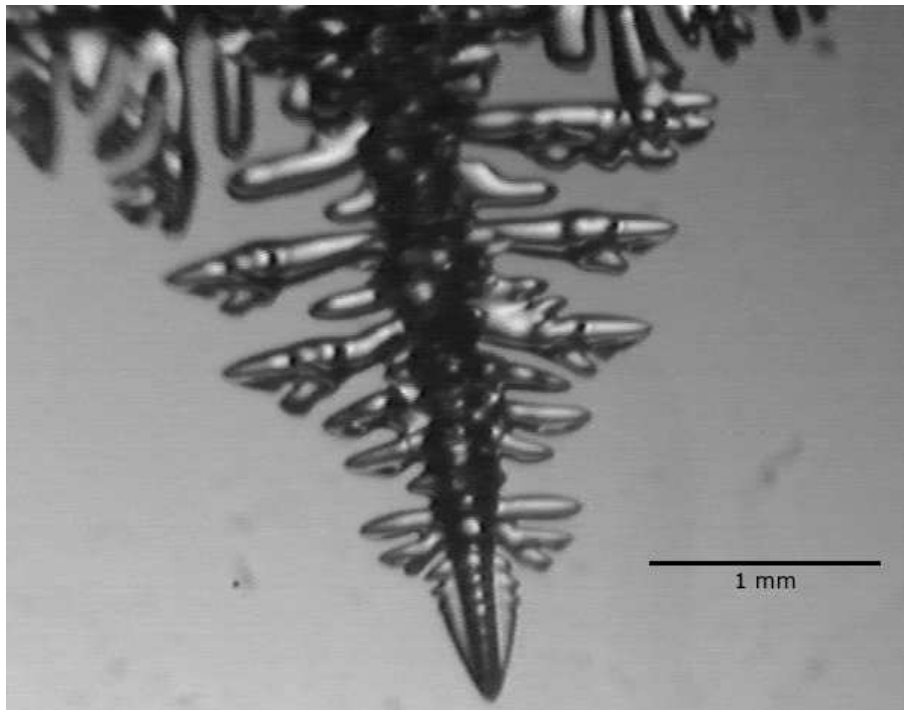


Figure 6.6: The two dominant sidebranch pairs show the same structures at the same relative position in their growth. This means these structures have been generated synchronously even if the distance between the two sides is about 1 mm.

The temporal evolution leading to this structure is shown in figure 6.7. The sequence covers the interval of one minute of growth, the interval between the pictures is 20 seconds. The main stem as well as the sidebranches show the sphere-like isotropic growth (a). More interesting, they do it synchronously and correlated over the large spatial distance mentioned before. The main tip shows the T-type sidebranching (b),(c). The instability at the main tip reaches the sidebranch tips about 20 seconds later and triggers a branching of all four of them (d). This higher order branchings happen synchronously for up to minutes, leading to cascading structures described in section 4.3.

The idea of absolutely identical conditions and fluctuations around the different tips so far apart seems not realistic, neither does the assumption of identical convective flow. The crystal is inclined with respect to the gravitational field, thus the convection on the both sides is not the same. Furthermore, the convective flow near the tip has been found (see chapt. 5) to be of the order of magnitude of about 0.5 mm/s, which is about one order of magnitude too fast for the observed delay between main and sidebranches tips.

Assuming the tip is the most unstable region then it will emit a small tip first (see section 4.1.1). This small tip has a higher curvature and thus a lower temperature as the original tip. The small tip will proceed into the melt with higher undercooling. Simultaneously heat will diffuse through the solid to the small tip. Due to the high thermal diffusivity of the crystal, the whole crystal will become colder and thus drive the sidebranches away from equilibrium,

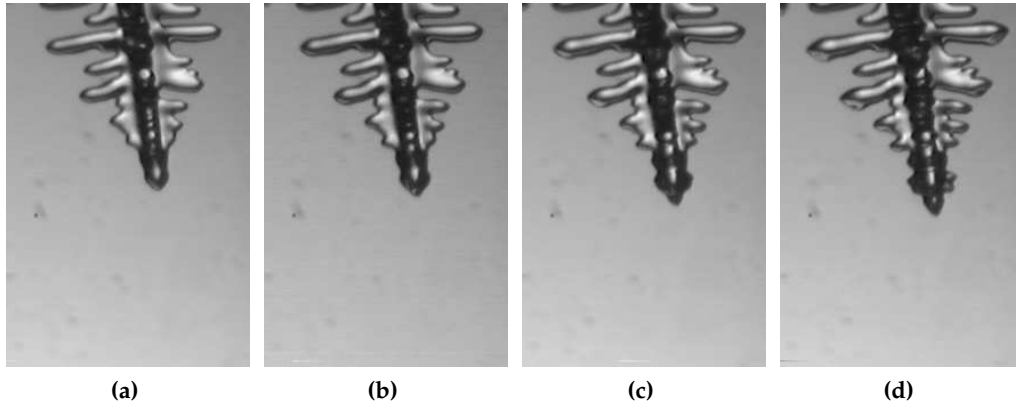


Figure 6.7: The temporal evolution (the sequence covers 1 minute) leading to the structures in figure 6.6. The sphere-like transition of the main tip is mirrored in the behavior of the sidebranch tips with a lag of about 30 s. The sidebranches growing on both sides behave synchronously (within the detection limit).

making the tips of the sidebranches unstable and trigger the emission of small tips from the sidebranches tips too. It might be that this mechanism is also active during the growth of other dendritic shapes e.g. snow crystals. This would explain the high degree of symmetry of snow crystals.

The simultaneity of the system behavior of the four sidebranches is within the experimental observed delay time of $t = 20$ s. With a thermal diffusivity in the solid of $D = D_{th}(s) \approx 4.96 \cdot 10^{-3} \text{ cm}^2/\text{s}$ (see appendix A) the expected distance for diffusion is estimated:

$$\begin{aligned} \langle x^2 \rangle &= D \cdot t \\ &\approx 1 \cdot 10^{-1} \text{ cm}^2, \end{aligned} \quad (6.1)$$

$$\sqrt{\langle x^2 \rangle} \approx 3 \cdot 10^{-1} \text{ cm} = 3 \text{ mm}. \quad (6.2)$$

The diffusion speed in the solid phase seems to be compatible with the observations.

6.5 Fluctuations and instability

In a recent paper, Pelcé analyzed the fluctuations in the tip region of a moving curved interface [82]. Depending on a constant $C = 8/\sigma \propto \rho^2 v$ and the inverse of the correlation time of the noise Γ at the tip, he finds three regions, where (i) the fluctuations are too small to overcome the anisotropic effects, i.e. the shape is determined by anisotropy alone, (ii) the fluctuations are so large that they are the reason for tip splittings and (iii) the fluctuations are in a range where they are small enough to keep the well-defined tip shape but large enough to overcome the anisotropic effects. With a mean $R = 30 \text{ }\mu\text{m}$, and $v = 3 \text{ }\mu\text{m}$, the values for xenon are as follows

$$\sqrt{C} \approx 17.4$$

$$\left(\frac{Dd_0R}{\Gamma}\right)^{\frac{1}{2}} = R/((2\pi)(k_B T/\gamma)^{\frac{1}{2}}(\log(R/a))^{\frac{1}{2}}) \approx 202,$$

$$\ln(202) \approx 10.6,$$

where a was chosen as $3 \cdot 10^{-10}$ as in Pelcé's Paper. The point lies in the region of the 'selection problem' as can be seen in figure 6.8.

A perturbation exceeding the amplitude of thermal noise therefore can drive the system in the tip-splitting regime. The periodic shaking fulfills this requirement. A sudden change of both $\rho \propto \sqrt{C}$ or $v \propto C$, triggered by only small changes in the convective flow around the tip, may shift the operating point.

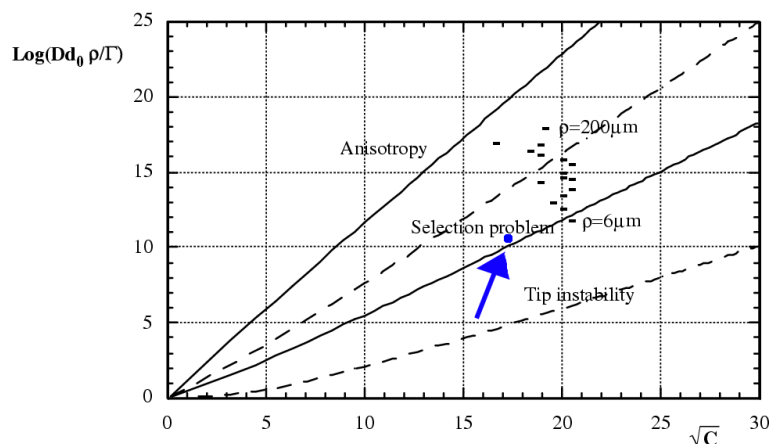


Figure 6.8: The selection diagram as Pelcé found it in [82]. The xenon dendrites lie in the region of the 'selection problem' as the SCN-results. The arrow indicates the position of the data of a xenon dendrite with $R = 30 \mu\text{m}$ and $v = 3 \mu\text{m}$.

6.6 Convection

The convective flow was thought to form a large toroidal convection roll in the growth vessel as shown in figure 6.9. Wittwer [63] bases on this assumption when he analyzes the influence of convection on the growth and especially the capability of latent heat removal in this context.

This model allows the interpretation of sudden growth mode changes reported by Fell [83]. It might be supposed that the inclined crystal tip can grow out of the main flow in the middle of the vessel. This would lead to *different growth conditions* for the tip region which could be *misinterpreted as changed growth mode*. Sometimes an additional 'swell of cold xenon' in the not isotropic flow in the vessel perturbs the steady state growth causing tip splitting. Heating would interrupt this flow and change its direction, the zero-flow transition would allow a phase of unperturbed isotropical growth.

The CFD simulations in this work indicate that this model has to be adapted. The buoyancy-induced convective flow in the lower region is much slower than above the crystal, because the

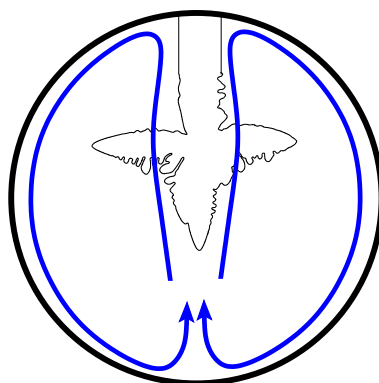


Figure 6.9: The assumption of convective flow in the growth vessel with a well defined toroidal roll across the whole vessel. (Two rolls in the 2D representation.) The CFD simulations are not compatible with this simple model.

convection cell bends towards the crystal in the middle of the growth vessel. Especially in the three dimensional simulation (see fig. 6.11), the xenon in the lower part of the vessel is almost in rest compared to a flow velocity of about 0.5 mm/s along the capillary. Still there is an important effect of the convection: It is responsible for the shape of the diffusional field. The overall movement of the fluid causes the latent heat develop a larger gradient than for a purely diffusive heat transport, not only at the tip but all along the crystal. The heat accumulates in the upper region of the vessel. The amount of transported heat is therefore increased around the lower part of the crystal, the gradient is steeper near the tip and the crystal grows faster, whereas the growth in the upper region is reduced. This idea agrees with the experimental finding that the overall shape of the crystal is much less developed towards the top and has rather a triangle shape in the projection, as shown in figure 6.10.

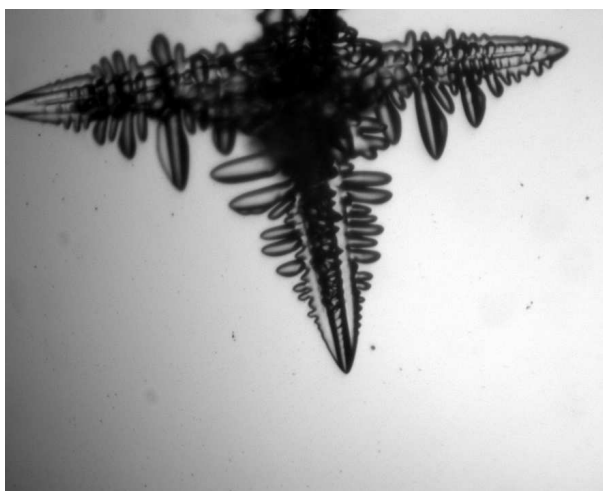


Figure 6.10: A free grown dendrite about 3 minutes after the start. The shapes pointing upwards are less evolved than the ones growing downwards.

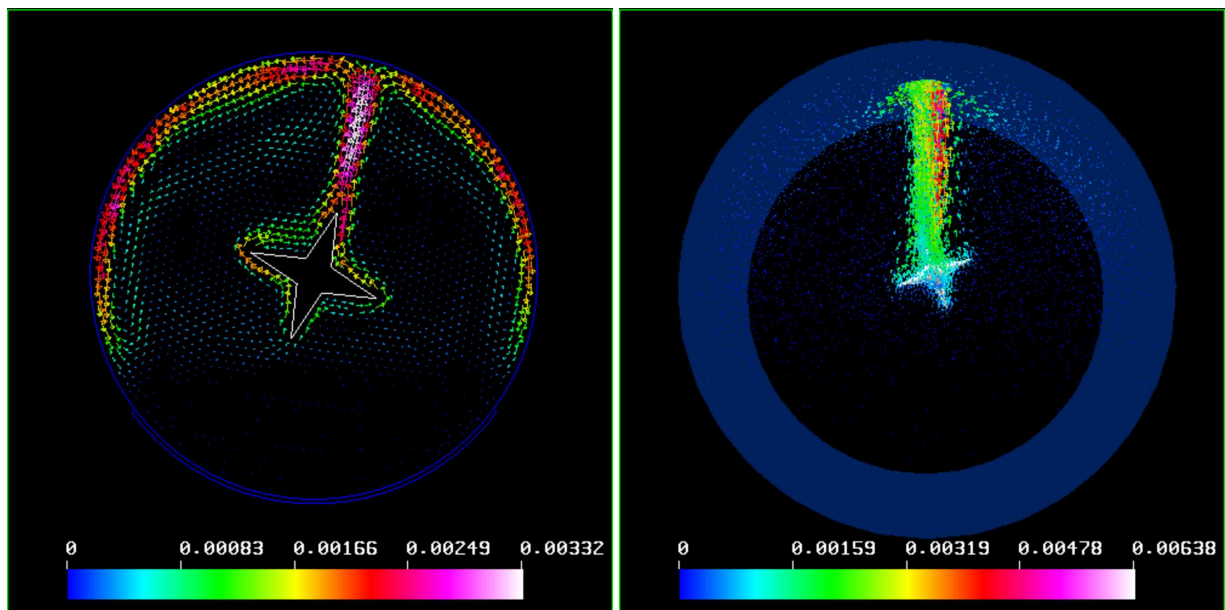


Figure 6.11: The velocity distribution as simulated in a 2D and a 3D domain with real parameters and a typical undercooling of 200 mK. The colors show the velocity in m/s.

In the case of microgravity the heat transport is assumed to be purely diffusive. The temperature distribution around the growing crystal is therefore different from an earth-based experiment. In this environment, LaCombe [18] observes tip velocity oscillations, indicating a periodic system behavior at the tip. This is qualitatively the same that was observed in the results presented here in section 4.4. This finding is a clue that the diffusive field *in* and around the crystal is more relevant for the dynamical system behavior than convection. The steady convective flow results in a different value for the growth rate (selection constant σ), but does not change the dynamic system behavior.

6.7 Conclusion

The experimental findings presented in this work lead to the statement that the system behavior of the growing dendrite allows several operating states. Indications for a meta-stable limit cycle have been found, causing the periodic tip splittings and the four-fold symmetric sidebranching as well as the tip velocity oscillations.

Thermal noise as small perturbation seems to be the reason for one type of sidebranches (N-type), and for random and transient tip splittings. This noise can also drive the system into the limit cycle operating mode. In free growth, this mode is active for only a transient phase, allowing bursts to emerge.

Still thermal noise seems not to be strong enough to drive the system into a stable multi-tip-configuration. This mode only can be stabilized by (periodic) external perturbations. Changes in the external forcing influence the kinetics near the solid-liquid interface causing inclinations

and twists.

Large perturbations (heating pulses, melting and large temperature drops) drive the system out of any steady state. The relaxation back to a steady state reveals deterministic behavior, such as the reproducible T-type sidebranches and the symmetry.

The mechanism of the fins surpassing the tip and therefore cause 'fake tip splittings' can explain the transition from a single tip with fourfold symmetry to either dendritic doublons, triplons or quadruplons. By a sequential appearance of this mechanism, the odd five or more multi-tip-configurations are explained.

The complicated system behavior, determined by a point attractor (operating point), by a limit cycle and by meta-stable multi-tip-configurations allows to control the characteristic growth parameters and therefore the shape of crystals. These findings might lead towards a dendrite engineering during solidification.

6.8 Outlook

Further investigations on the topic of dendritic growth under influence of perturbations seem promising in a search for controlled crystal shaping. There are open questions on how the different effects of shaking on the growth (e.g. inclination, twist) can be explained on both, microscopical and mesoscopical length scales. It would also be desirable to have a model that compares the shaking and melting effects, maybe in a theoretical framework. Experimentally, a closer look on the consequences of perturbed growth on grain refinement during continuous casting would be useful. A good starting point might be the interaction of dendrite arrays as they develop in directional solidification.

Appendix A

Xenon

Molecular weight	M_m	131.30	g/mol	
Triple-point temperature	T_t	161.3897	K	[a]
Triple-point pressure	p_t	0.816901	bar	[b]
Triple-point molar volume (l) ¹	$V_m(l)$	44.31	cm^3/mol	[c]
Triple-point molar volume (s) ¹	$V_m(s)$	38.59	cm^3/mol	[c]
Heat of fusion	L	2299	J/mol	[d]
Melting entropy	ΔS_m	24.24	J/mol	
Jackson α -factor	$\alpha_{Jackson}$	1.71		**
Specific heat (l)	$c_p(l)$	44.6	$J/mol K$	[d]
Specific heat (s)	$c_p(s)$	36.0	$J/mol K$	[d]
Thermal conductivity (l)	λ_l	$0.734 \cdot 10^{-3}$	$W/cm K$	[e]
Thermal conductivity (s)	λ_s	$4.76 \cdot 10^{-3}$	$W/cm K$	[e]
Thermal diffusivity (l)	$D_{th}(l)$	$7.29 \cdot 10^{-4}$	cm^2/s	
Thermal diffusivity (s)	$D_{th}(s)$	$4.96 \cdot 10^{-3}$	cm^2/s	
Refractive index (l)	n_l	1.3957		[f]
Refractive index (s)	n_s	1.4560		[g]
Solid-liquid interfacial free energy	γ_{sl}	$1.073 \cdot 10^{-8}$	J/cm^2	[h]
	γ_{sl}	$0.975 \cdot 10^{-8}$	J/cm^2	[i]
Capillary length	d_0	$4.9 \cdot 10^{-8}$	cm	
Unit of supercooling	θ	59.2	K	

¹(l) liquid; (s) solid

- [a] R.E. Bedford, G. Bonnier, H. Mass and F. Pavese, *Metrologia* **20**, 145 (1984)
- [b] J. Ancsin, *Metrologia* **14**, 45 (1978)
- [c] *Rare gas solids*, Eds. M.L. Klein and J.A. Venables (Academic Press Inc., New York, 1977)
- [d] *Selected Values of the Thermodynamic Properties of the Elements* (American Soc. Metals, Metals Park, OH, 1973)
- [e] *Thermophysical Properties of Matter*, TPRC Data Series, Vol. 3 (IFI/Plenum, New York, 1970)
- [f] W.M. Yen and R.E. Norberg, *Phys. Rev.* **131**, 269 (1963)
- [g] A.C. Sinnock and B.L. Smith, *Phys. Rev.* **181**, 1297 (1969)
- [h] Estimate according D. Turnbull, in *Phase Changes*, edited by F. Seitz and D. Turnbull (TMS-AIME, Warrendale, 1983)
- [i] I. Stalder and J.H. Bilgram, *J. Chem. Phys.* **118**, 7981-7984 (2003)

** Materials with $\alpha < 2$ are usually not faceting in contact with the melt.

Appendix B

Piezo

For the driving of the oscillations, a commercially available piezo from Physik Instrumente was used. The PICMA[®] Chip Monolithic Multilayer Piezo Actuator (LowVoltagePZT) PL033 was found to be small enough to fit in the close space and to provide a relatively large amplitude. The nominal properties are found in table B.1.

length \times width [± 0.1 mm]	$l \times w$	3×3	mm ²
height [± 0.05 mm]	h	2	mm
displacement [$\pm 20\%$]	s	2.2	μm @ 100 V
blocking force	F	> 300	N
electrical capacitance [$\pm 20\%$]		50	nF
resonant frequency	f_r	> 300	kHz
max. operating voltage		-20to + 120V	
max. operating temperature		150	$^{\circ}\text{C}$

Table B.1: Technical properties of the piezo actuator according to the data sheet.

Measurement of the characteristic curve

The voltage-displacement curve was determined by means of an ad-hoc Michelson interferometer (see fig.B.1). The number of interference fringes of a He-Ne laser are supposed to be proportional to the voltage. This linear dependency is shown in figure B.2 for two different piezo (the PL022 is smaller). The read out error of the brightness is about $\frac{\lambda}{8}$, symbolized by the error bars in y-direction. The voltage was read out when the interference fringes were 'bright' or 'dark', which leads to a scatter in the voltage values (symbolized by the error bars in x-direction). The PL022 is in good agreement with the table data, where for the PL033 we find an elongation of

$2.3 \times \lambda @ 100V$, which is a little too low compared to the reference. In the experimental setup the PL033 was used.

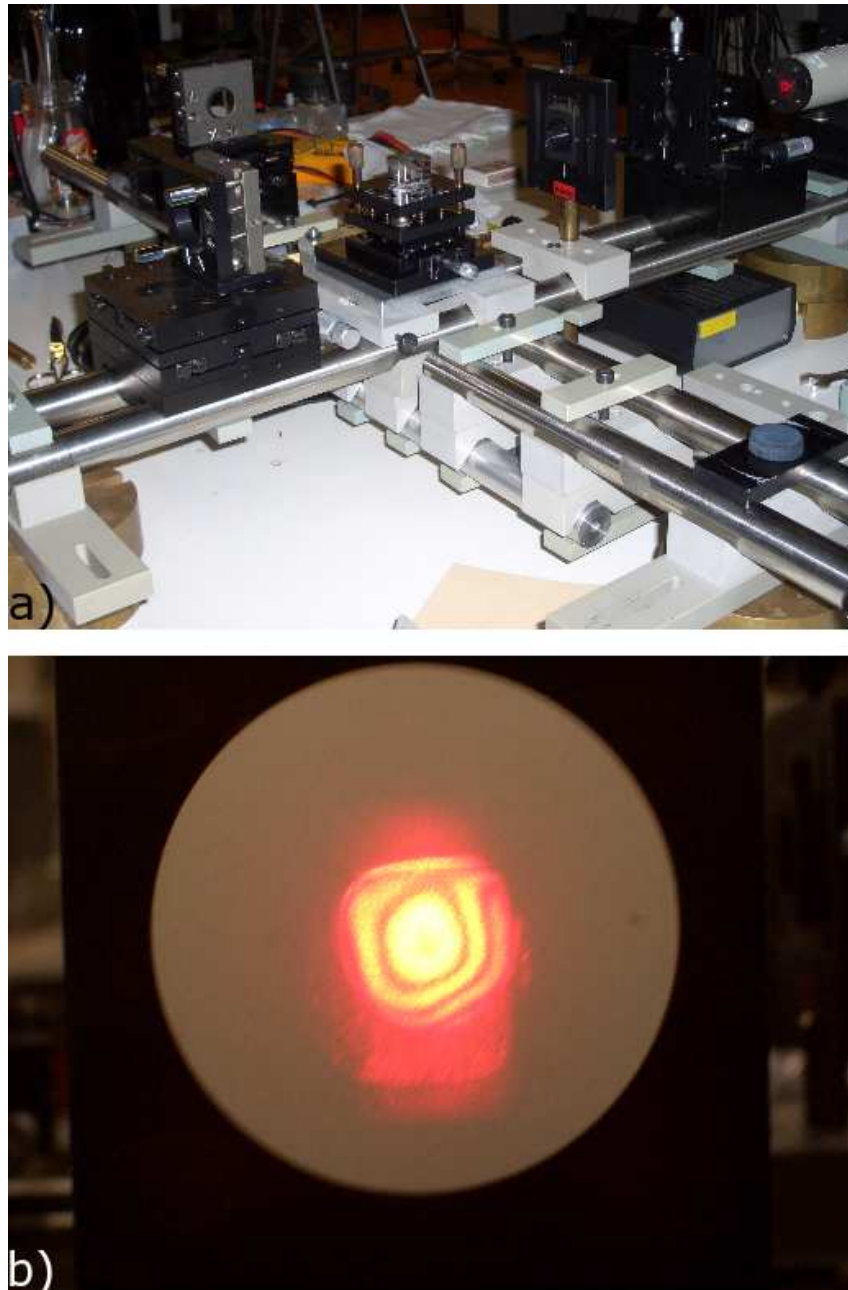


Figure B.1: a) The ad-hoc Michelson interferometer that was used to measure the piezo elongation. The geometrical length of one of the arms was changed by the piezo, depending on the applied voltage. (b) The interference fringes as observed in steady-state.

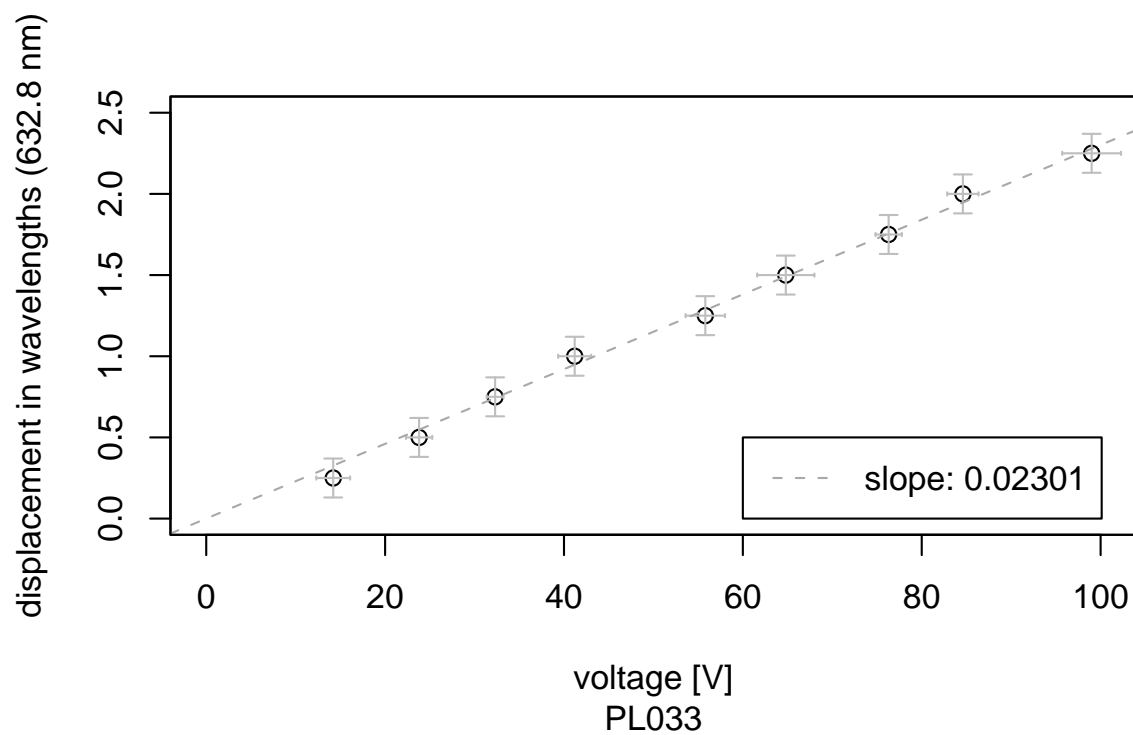
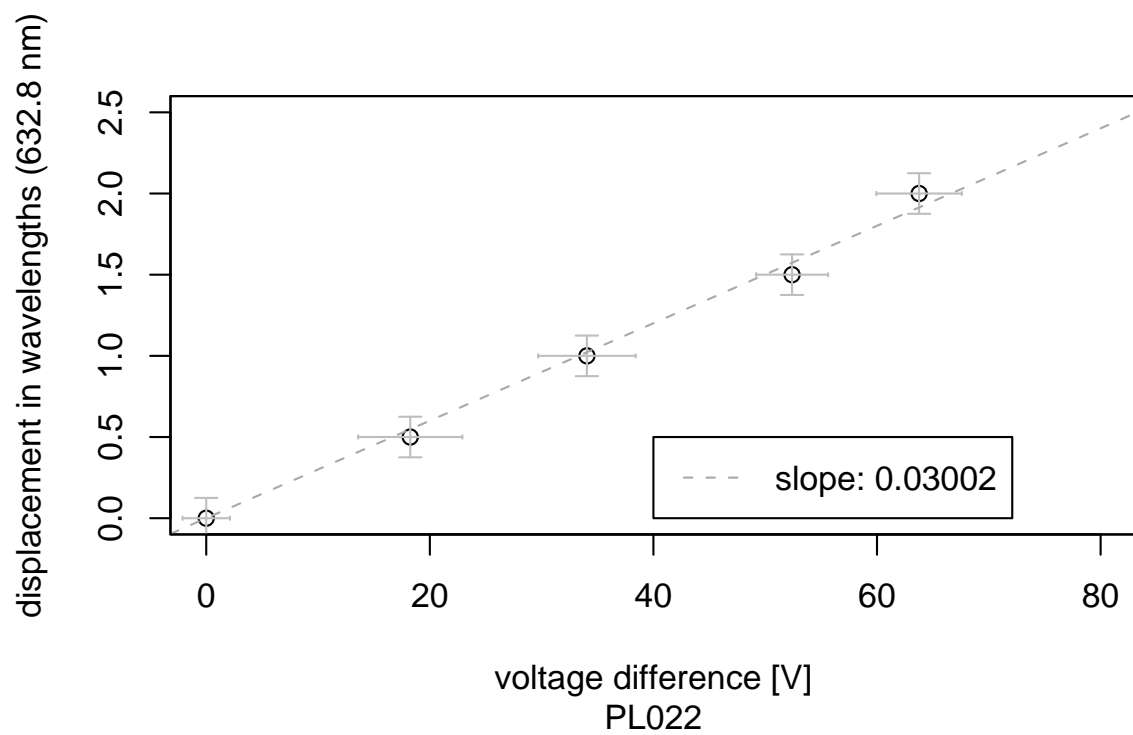


Figure B.2: The elongation of two piezo vs. the applied voltage shows a good linear dependency. The error bars indicate the measurement error mentioned in the text.

References

- [1] F. C. Frank. *Contemporary Physics*, **23**: 3–22 (1982).
- [2] R. H. Mathiesen, L. Arnberg, F. Mo, T. Weitkamp and A. Snigirev. *Phys. Rev. Lett.*, **83**: 5062–5065 (1999).
- [3] B. Li, H. D. Brody and A. Kazimirov. *Phys. Rev. E*, **70**: 062602 (2004).
- [4] N. Mangelinck-Noël, H. Nguyen-Thi, G. Reinhart, T. Schenk, V. Cristiglio, M. D. Dupouy, J. Gastaldi, B. Billia, J. Härtwig and J. Baruchel. *Journal Of Physics D*, **38**: A28–A32 (2005).
- [5] J. S. Langer and H. Müller-Krumbhaar. *Acta Metall.*, **26**: 1681–1687 (1978).
- [6] J. S. Langer. *Reviews Of Modern Physics*, **52**: 1–28 (1980).
- [7] J. S. Langer. In J. Souletie, J. Vannimenus and R. Stora (eds.), *Chance And Matter: Les Houches, Session XLVI, 1986*, pp. 629–711. Elsevier Science Publisher B. V., Amsterdam (1987).
- [8] M. Ben Amar and E. A. Brener. *Phys. Rev. Lett.*, **71**: 589–592 (1993).
- [9] E. A. Brener. *Phys. Rev. Lett.*, **71**: 3653–3656 (1993).
- [10] H. Honjo, S. Ohta and Y. Sawada. *Phys. Rev. Lett.*, **55**: 841 (1985).
- [11] U. Bisang and J. H. Bilgram. *Phys. Rev. E*, **54**: 5309–5326 (1996).
- [12] J. H. Bilgram, M. Firmann and E. Hürlimann. *J. Cryst. Growth*, **96**: 175–187 (1989).
- [13] E. Hürlimann, R. Trittbach, U. Bisang and J. H. Bilgram. *Phys. Rev. A*, **46**: 6579–6595 (1992).
- [14] A. Dougherty, P. D. Kaplan and J. P. Gollub. *Phys. Rev. Lett.*, **58**: 1652 (1987).
- [15] A. Dougherty and R. Chen. *Phys. Rev. A*, **46**: 4508–4511 (1992).
- [16] D. P. Corrigan, M. B. Koss, J. C. LaCombe, K. D. De Jager, L. A. Tennenhouse and M. E. Glicksman. *Phys. Rev. E*, **60**: 7217–7223 (1999).
- [17] M. E. Glicksman, M. B. Koss and E. A. Winsa. *Phys. Rev. Lett.*, **73**: 573–576 (1994).
- [18] J. C. LaCombe, M. B. Koss, J. E. Frei, C. Giummarra, A. O. Lupulescu and M. E. Glicksman. *Phys. Rev. E*, **65**: 031604 (2002).

- [19] X. W. Qian and H. Z. Cummins. *Phys. Rev. Lett.*, **64**: 3038 – 3041 (1990).
- [20] W. Losert, D. A. Stillman, H. Z. Cummins, P. Koczyński, W.-J. Rappel and A. Karma. *Phys. Rev. E*, **58**: 7492–7506 (1998).
- [21] K. Lee and W. Losert. *J. Cryst. Growth*, **269**: 592–598 (2004).
- [22] P. Bouissou, B. Perrin and P. Tabeling. *Phys. Rev. A*, **40**: 509–512 (1989).
- [23] P. Bouissou, B. Chiffaudel, B. Perrin and P. Tabeling. *Europhys. Lett.*, **13**: 89–94 (1990).
- [24] T. Börzsönyi, T. T. Katona, Á. Buka and L. Gránásy. *Phys. Rev. Lett.*, **83**: 2853 (1999).
- [25] M. B. Koss, J. C. LaCombe, A. Chait, V. Pines, M. Zlatkowsky, M. E. Glicksman and P. Kar. *J. Cryst. Growth*, **279**: 170–185 (2005).
- [26] A. Dougherty and T. Nunnally. *J. Cryst. Growth*, **300**: 467–472 (2007).
- [27] Y.-W. Lee, R. Ananth and W. N. Gill. *J. Cryst. Growth*, **132**: 226–230 (1993).
- [28] R. Tönhardt and G. Amberg. *Phys. Rev. E*, **62**: 828–836 (2000).
- [29] X. Tong, C. Beckermann, A. Karma and Q. Li. *Phys. Rev. E*, **63**: 061601 (2001).
- [30] Y. Lu, C. Beckermann and J. C. Ramirez. *J. Cryst. Growth*, **280**: 320–334 (2005).
- [31] K.-K. Koo, R. Ananth and W. N. Gill. *Phys. Rev. A*, **44**: 3782–3790 (1991).
- [32] S. Akamatsu, G. Faivre and T. Ihle. *Phys. Rev. E*, **51**: 4751–4773 (1995).
- [33] I. Stalder and J. H. Bilgram. *Europhys. Lett.*, **56**: 829–835 (2001).
- [34] B. T. Murray, A. A. Wheeler and M. E. Glicksman. *J. Cryst. Growth*, **154**: 386–400 (1995).
- [35] H.-J. Diepers, D. Ma and I. Steinbach. *J. Cryst. Growth*, **237**: 149–153 (2002).
- [36] S. Liu, S.-Z. Lu and A. Hellawell. *J. Cryst. Growth*, **234**: 751–758 (2002).
- [37] A. V. Gorbunov. *Solid State Phenomena*, **23**: 15–28 (1992).
- [38] A. Karma, Y. H. Lee and M. Plapp. *Phys. Rev. E*, **61**: 3996–4006 (2000).
- [39] L. Rubinstein. *The Stefan Problem*. Providence, Rhode Island (1971).
- [40] G. P. Ivantsov. *Dokl. Akad. Nauk SSSR*, **58**: 567–569 (1947).
- [41] G. E. Nash and M. E. Glicksman. *Acta Metall.*, **22**: 1283–1290 (1974).
- [42] R. Pieters and J. S. Langer. *Phys. Rev. Lett.*, **56**: 1948–1951 (1986).
- [43] M. N. Barber, A. Barbieri and J. S. Langer. *Phys. Rev. A*, **36**: 3340–3349 (1987).
- [44] D. A. Kessler, J. Koplik and H. Levine. *Adv. Phys.*, **37**: 255–339 (1988).

- [45] J. S. Langer. *Phys. Rev. A*, **36**: 3350–3358 (1987).
- [46] U. Bisang and J. H. Bilgram. *Phys. Rev. Lett.*, **75**: 3898–3901 (1995).
- [47] E. A. Brener and D. Temkin. *Phys. Rev. E*, **51**: 351–359 (1995).
- [48] O. Wittwer and J. H. Bilgram. *Phys. Rev. E*, **74**: 041604 (2006).
- [49] E. A. Brener, K. Kassner, H. Müller-Krumbhaar and D. Temkin. *Int. Jour. Mod. Phys. C*, **3**: 825–851 (1992).
- [50] E. A. Brener, H. Müller-Krumbhaar and D. Temkin. *Europhys. Lett.*, **17**: 535 (1992).
- [51] E. A. Brener, H. Müller-Krumbhaar and D. Temkin. *Phys. Rev. E*, **54**: 2714–2722 (1996).
- [52] H. M. Singer, I. Singer-Loginova, J. H. Bilgram and G. Amberg. *J. Cryst. Growth*, **296**: 58–68 (2006).
- [53] T. Ihle and H. Müller-Krumbhaar. *Phys. Rev. Lett.*, **70**: 3083–3086 (1993).
- [54] T. Ihle and H. Müller-Krumbhaar. *Phys. Rev. E*, **49**: 2972–2991 (1994).
- [55] U. Lappe. *Experimentelle untersuchung des dendritischen wachstums von kristallen in unterkühlten schmelzen*. Tech. Rep. 1671, Forschungszentrum Jülich (1980).
- [56] E. G. Holzmann. *On Dendritic Growth*. Ph.D. thesis, Dept. of Electrical Engineering, Stanford University (1969).
- [57] J. S. Langer and H. Müller-Krumbhaar. *Phys. Rev. A*, **27**: 499–514 (1983).
- [58] R. K. Trivedi and J. T. Mason. *Metall. Trans. A*, **220**: 235–249 (1991).
- [59] E. Raz, S. G. Lipson and E. Polturak. *Phys. Rev. A*, **40**: 1088–1095 (1989).
- [60] M. E. Glicksman, J. S. Lowengrub and S. Li. In C.-A. Gandin and M. Bellet (eds.), *Modeling Of Casting, Welding And Advanced Solidification Processes - XI*, pp. 521–528. TMS (The Minerals, Metals & Materials Society) (2006).
- [61] M. E. Glicksman, R. J. Schaefer and J. D. Ayers. *Metall. Trans. A*, **7**: 1747–1759 (1974).
- [62] H. M. Singer and J. H. Bilgram. *J. Cryst. Growth*, **261**: 122–134 (2004).
- [63] O. Wittwer. *Solidification Of Xenon: Instabilities Leading To Complex Structures*. Ph.D. thesis, Laboratorium für Festkörperphysik, ETH Zürich (2006).
- [64] H. M. Singer and J. H. Bilgram. *Phys. Rev. E*, **69**: 032601 (2004).
- [65] I. Steinbach, H.-J. Diepers and C. Beckermann. *J. Cryst. Growth*, **275**: 624–638 (2005).
- [66] M. E. Glicksman, A. O. Lupulescu and M. B. Koss. *J. Thermophys. Heat Transfer*, **17**: 69–76 (2003).

- [67] A. O. Lupulescu, M. E. Glicksman and M. B. Koss. *J. Cryst. Growth*, **276**: 549–565 (2005).
- [68] I. Stalder. *Morphology Of Structures in Three-Dimensional Diffusional Growth*. Ph.D. thesis, Laboratorium für Festkörperphysik, ETH Zürich, Zürich (2000).
- [69] B. Utter, R. Ragnarsson and E. Bodenschatz. *Phys. Rev. Lett.*, **86**: 4604–4607 (2001).
- [70] A. Karma and A. E. Lobkovsky. *Phys. Rev. Lett.*, **92**: 245510 (2004).
- [71] S. Henry, T. Minghetti and M. Rappaz. *Acta Materialia*, **46**: 6431–6443 (1998).
- [72] K. A. Jackson, D. R. Uhlmann and J. D. Hunt. *J. Cryst. Growth*, **1**: 1–36 (1967).
- [73] M. Conti. *Phys. Rev. E*, **69**: 022601 (2004).
- [74] M. Dorn-Aymon. *Side Branch Development Of Dendritic Growth And Analysis Of The Tip-Splitting Phenomenon in Xenon Crystals*. Diploma thesis, Laboratorium für Festkörperphysik, ETH Zürich (2003).
- [75] C. Weiss, N. Bergeon, N. Mangelinck-Noël and B. Billia. *Mat. Sci. Eng. A*, **413**: 296–301 (2005).
- [76] B. Billia. *Private Communication* (2006).
- [77] M. Tatsuno. *J. Phys. Soc. Jpn.*, **50**: 330–337 (1981).
- [78] T. Ihle. *Wachstumsmuster unter diffusivem transport*. Tech. Rep. 3230, Jülich-D (1996).
- [79] M. Georgelin and A. Pocheau. *Phys. Rev. E*, **57**: 3189–3203 (1998).
- [80] M. Georgelin, S. Bodea and A. Pocheau. *Europhys. Lett.*, **77**: 46001 (2007).
- [81] M. Plapp. *Private Communication* (2005).
- [82] P. Pelcé. *Europhys. Lett.*, **75**: 220–226 (2006).
- [83] M. Fell. *Untersuchung von Wachstumsmoden von Xenon-Dendriten an der Wachsenden Spitze*. Diploma thesis, Laboratorium für Festkörperphysik, ETH Zürich (2003).

Presentation and publication list

March 2005	DGK/DGKK, Köln	Talk: Heat induced symmetrization of xenon dendrites
March 2005	DPG, Berlin	Talk: Controlling of symmetry and fractal dimension of xenon dendrites by heating Poster: Controlling of fractal dimension and symmetry of growing xenon crystals
June 2005	ICASP, Stockholm	Paper presentation: Controlling the symmetry of xenon crystals by repetitive heating, M. Fell et al., <i>Mat. Sci. Eng. A</i> , 413-414 (2005), 451-454
February 2006	7. Kinetikseminar der DGKK, Halle	Talk: Transiente dendritische Wachstumsformen bei Temperaturänderungen
March 2006	APS, Baltimore	Talk: Transient growth and controlled side-branching of xenon dendrites
March 2006	DPG, Dresden	Talk: Controlling of structure formation in crystal growth Poster: Controlling of structure formation in crystal growth
September 2006	BACG, Edinburgh	Talk: Dendrite Engineering by means of heating and shaking

Curriculum vitae

Name	Marco Fell
Date of birth	July 10, 1976 in Chur
Citizen of	Valendas (GR), Switzerland
1983-1989	Primarschule in Arosa
1989-1996	Gymnasium in Chur
July 1996	Matura Typus C, Matura work: „Einführung in die KI: Wasserstandsregelung mittels eines Neuronalen Backpropagation-Netzes“
1997-2003	Physics student at the ETH Zürich
Spring 2002	Semester work on <i>Simulation des Neuron-Elektroden-Interface</i> in Prof. Dr. H. Baltes' group at the Physical Electronics Laboratory (PEL), ETH Zürich
Spring 2003	Diploma thesis on <i>Untersuchung von Wachstumsmoden von Xenon-Dendriten an der wachsenden Spitze</i> in the group of Prof. Dr. J. H. Bilgram at the Laboratorium für Festkörperphysik, ETH Zürich
2003-2006/7	Research and teaching assistant to Prof. Bilgram in the <i>Dendrites research group</i> within the group of Prof. Batlogg at the Laboratorium für Festkörperphysik, ETH Zürich
Winter 2006/7	Doctoral thesis at the ETH Zürich on <i>Dendrite Engineering on Xenon Crystals</i> .

Dank

Prof. Dr. Jörg H. Bilgram hat es ermöglicht, dass ich meine Dissertation in seinem „Dendrite research team“ machen konnte. Für seine unzähligen Anregungen, Ideen und die in zurückhaltender Art angebrachte, immer sehr konstruktive Kritik gilt ihm mein Dank. Sein riesiges Wissen in vielen Gebieten der Physik hat mir immer wieder neue Stichworte liefern können, und die mittäglichen Gespräche über wissenschaftliche, historische, politische und musische Themen werden unvergessen bleiben. **Hansruedi Aeschbach** hat sehr zuvorkommend und mit ausserordentlichem Einsatz dafür gesorgt, dass ich die eine Anlage nach über 10 Jahren wieder in Betrieb nehmen und an zwei Experimentierstationen viele Messungen machen konnte. Sein technisches Talent, seine Erfahrungen und die Apparatekenntnisse waren höchst wertvoll für die Modifikationen der beiden Anlagen.

Prof. Dr. K. Ensslin hat als Vorsteher des Laboratoriums für Festkörperphysik wesentlichen Einfluss gehabt, dass diese Arbeit zustande kommen konnte, und er hat als Referent gewirkt. **Prof. Dr. B. Billia** hat meine Arbeit sehr eingehend studiert und mir anlässlich zweier Besuche viele wertvolle Hinweise gegeben. **Prof. Dr. H. Müller-Krumbhaar** hat trotz seiner grossen Arbeitsbelastung meine Dissertation beurteilt. In der Gruppe von **Prof. Dr. B. Batlogg** habe ich eine sehr gute unbürokratische Atmosphäre erlebt.

Prof. Dr. A. Dougherty, **Prof. Dr. H. Reichelt** und **Prof. Dr. E. Haller** sowie **Dr. M. Plapp** konnte ich kennenlernen und mit ihnen im Labor und auf verschiedenen Tagungen fruchtbare Diskussionen führen.

Es war für mich eine Ehre und eine Herausforderung, auf der weitherum anerkannten Arbeit meiner Vorgänger im „Dendrite research team“ aufbauen und meine eigenen Experimente beitragen zu können. In dieser Reihe möchte ich besonders **Dr. Herman Singer** danken. Er hat mich insbesondere zu Beginn unterstützt und viele gute Ideen beigetragen. Seine Computerprogramme waren und sind die Grundlage vieler Arbeitsschritte. Mit **Dr. Oliver Wittwer** konnte ich viele Gedanken insbesondere in der Methodik diskutieren und umsetzen. **Dr. Ivo Stalder** hat mich als „Coach“ betreut. Die interessanten Gespräche über wissenschaftliche und weniger wissenschaftliche Themen mögen auch in Zukunft stattfinden, im Labor und im Bistro und im Fédéral und in der Metzgerhalle und im Cheyenne. . . **Gregor Kreuzer**, **Lars Mächler** und **Patrick Stocker**, haben in ihren Diplom- und Semesterarbeiten sehr gute Beiträge geliefert.

Sofia Deloudi danke ich für die vielen Kaffeerunden mit interessanten Gesprächen über Kristallographie und Quasikristalle und für ihre Unterstützung in wissenschaftsfernen Gebieten;-)

Schliesslich gebührt mein Dank meiner engsten Umgebung: Meinen **Eltern** für alles, was sie für mich getan und mir mitgegeben haben, meinen Geschwistern **Urs** und **Anian** und meiner Freundin **Regula**, die in den letzten Monaten leider oft nur an zweiter Stelle kam. Sie alle haben immer ein offenes Ohr für meine Berichte aus dem Labor gehabt, und sie haben mich motiviert und unterstützt, selbst wenn sie zeitweise nicht so ganz verstanden haben, worin.

In Wirklichkeit ist die Realität ganz anders.

Quelle unbekannt